

University of Pardubice
Jan Perner Transport Faculty

STRENGTH OF GLUE JOINTS OF METALLIC MATERIALS IN
CONNECTION WITH DESIGN OF JOINTS

by

İbrahim KOCABAŞ

Doctoral Thesis

2016

University of Pardubice
Jan Perner Transport Faculty
Department of Mechanics, Materials and Machine Parts

**STRENGTH OF GLUE JOINTS OF METALLIC MATERIALS IN
CONNECTION WITH DESIGN OF JOINTS**

by

İbrahim KOCABAŞ

Supervisor: Doc. Ing. Pavel Švanda, *PhD*

Doctoral Thesis

2016

Prohlašuji:

Tuto práci jsem vypracovala samostatně. Veškeré literární prameny a informace, které jsem v práci využila, jsou uvedeny v seznamu použité literatury.

Byla jsem seznámena s tím, že se na moji práci vztahují práva a povinnosti vyplývající ze zákona č. 121/2000 Sb., autorský zákon, zejména se skutečností, že Univerzita Pardubice má právo na uzavření licenční smlouvy o užití této práce jako školního díla podle § 60 odst. 1 autorského zákona, a s tím, že pokud dojde k užití této práce mnou nebo bude poskytnuta licence o užití jinému subjektu, je Univerzita Pardubice oprávněna ode mne požadovat přiměřený příspěvek na úhradu nákladů, které na vytvoření díla vynaložila, a to podle okolností až do jejich skutečné výše.

Souhlasím s prezenčním zpřístupněním své práce v Univerzitní knihovně.

V Pardubicích dne 01. 09. 2016

İbrahim KOCABAŞ

Declaration by author

I declare:

This thesis was developed independently. All literary sources and the information that I use at work, are listed in the bibliography.

I was familiar with the fact that my work is to apply the rights and obligations arising from Act No. 121/2000 statute. Copyright Act, particularly the fact that the University of Pardubice has the right to conclude a license agreement for use of this work as school work by § 60 paragraph 1 copyright Act, and the fact that if the use of this work with me or to be granted a license to use another entity, the University of Pardubice authorized me to request a reasonable contribution to cover costs incurred in the creation of the work, according to circumstances, until their actual amount.

I agree with the full disclosure of their work in the university library.

In Pardubice on the 01.09.2016

İbrahim KOCABAŞ

ACKNOWLEDGEMENT

First and foremost, the author would like to thank to his supervisor Ing. Doc. Pavel SVANDA for his invaluable guidance, effort and contribution during the dissertation study. He also inspired the author greatly to complete the study and showed him some examples that related the topic of the dissertation study. Besides, the author wishes to express thank the authority of Jan Perner Transport Faculty for providing him with a good environment and facilities to accomplish experiments and complete the study. Finally, an honorable mention goes to the author's family and colleagues for their patience, motivation and support in completing the study. Without helps of the particular that mentioned above, many difficulties would be faced while doing this.

İbrahim KOCABAŞ

ABSTRACT

Estimation of the load carrying capacity of the adhesively bonded structures is the main challenge in the bonded constructions and structures prior to manufacture stage. Particularly, the adhesive joints in the railway and automotive industry increasingly becoming the most popular joining method recently. In order to make an accurate prediction of the load carrying capacity of an adhesive joint, modern fracture mechanic approaches are employed using the finite element package program “ABAQUS®”, in this dissertation study. In this regard, metallic substrates were considered to simulate structural mild steels having different tensile strengths. Then the adhesive joints were manufactured with two different epoxy adhesives which are Veropal HE20 and Carboresin. FE models of the adhesive joints were created for a variety of the different joint configurations. A validation procedure was followed between experimental and numerical failure loads, which corresponds to the maximum error of 18%. Besides, a parametric study was accomplished to establish a simple expression of the failure load in terms of the geometrical and material parameters of the adhesive joint. Moreover, the effect of each parameter on the joint load carrying capacity was examined and presented in the study. Finally, three design parameters; L/t , σ_a/σ_y and $F/\sigma_y t$ were decided to be the most substantial for an optimum adhesive joint design.

Keywords: Fracture mechanics, Single lap joint, FE method, Epoxy adhesive, Mild steel

SOUHRN

Určení zatížitelnosti lepených spojů důležitým parametrem konstrukcí či zařízení při jejich konstrukčním návrhu. V současné době se výrazně zvyšuje podíl lepených spojů při výrobě automobilů či kolejových vozidel. V některých aplikacích je spojování lepením již hlavním způsobem spojování dílů. Pro určení zatížitelnosti lepených spojů je dnes možno využít poznatků lomové mechaniky a chování spojů simulovat s využitím metody konečných prvků. V případě této disertační práce byl použit software “ABAQUS®”. Pro simulace byly uvažovány nelegované konstrukční oceli s různými mechanickými vlastnostmi (rozdílnou mezí pevnosti). Jako lepidla byla použita epoxidová lepidla s rozdílnými mechanickými vlastnostmi - Veropal HE20 a Carboresin. Modely pro řešení zatížitelnosti s využitím metody konečných prvků byly vytvořeny pro rozdílná konstrukční uspořádání lepených spojů. Ověření modelů bylo provedeno srovnáním s reálnými vzorky. Porovnáním síly pro porušení lepených spojů získaných při simulačních výpočtech a při experimentech byla zjištěna odchylka maximálně 18%. Cílem práce bylo vytvoření parametrické studie, na jejímž základě bylo možno získat rovnici pro zatížitelnost lepeného spoje s ohledem na geometrické a materiálové parametry lepených spojů. Pro určení únosnosti spojů byly navrženy tři parametry spoje L/t , σ_a/σ_y and F/σ_{yt} , které se ukázaly, že mají největší vliv na kvalitu lepených spojů.

Klíčová slova : lomová mechanika, jednoduše přeplátovaný lepený spoj, metoda konečných prvků, epoxidové lepidlo, konstrukční ocel.

Table of Contents

1. Introduction	16
2. Literature Review.....	17
2.1 History of Cohesive Zone Models	17
2.2 Design of Adhesively Bonded Single Lap Joints	18
2.3 Advantages of Adhesively Bonded Joints	19
2.4 Limitations of Adhesively Bonded Joints	20
2.5 Modern Adhesive Types and Main Characteristics	21
2.6 Methods of Improving the Joint Efficiency.....	23
3. Objectives of the Dissertation.....	27
3.1 Motivation.....	27
3.2 The Theoretical Part.....	28
3.3 The Experimental Part	29
4. Material Nonlinearity and Description of Progressive Failure Model.....	30
4.1 Cohesive Zone Damage Model.....	30
4.2 Thickness-Dependence Cohesive Parameters.....	32
4.2.1 Initial Stiffness	32
4.2.2 Total Fracture Energy.....	33
4.2.3 Separation Strength	34
4.3 Material and Geometry Description	37
4.3.1 Single Lap Joint Geometry	37
4.3.2 Adherend Material Model	38
4.3.3 Adhesive Material Model.....	39
4.4 Implementation of FE Analysis	41
4.4.1 Numerical Model.....	41
4.4.2 Boundary Conditions and Loading.....	42
4.4.3 Mesh Optimization	43

4.4.4 Numerical Solution Algorithm	44
5. Material and Experimental Procedure	46
5.1 Determination of Material Parameters	46
5.1.1 Uniaxial tensile test of bulk samples	46
5.1.2 Double cantilever beam (DCB) test	51
5.1.3 End-notched flexure (ENF) test	53
5.2 Manufacture of Single Lap Joints	55
5.3 Testing Strength of Adhesive Joints	57
5.3.1 Validation of numerical model.....	58
5.3.2 Material and geometry dependent parametric study	63
6. Numerical Results and Discussion	65
6.1 Interface Stress Analysis.....	66
6.1.1 Peeling Stress Distributions.....	66
6.1.2 Shear Stress Distributions	69
6.2 Load Carrying Capacity of the Single Lap Joints	72
6.2.1 Effect of Adhesive Ultimate Tensile Strength and Stiffness.....	72
6.2.2 Adherend Rigidity Effect	75
6.2.3 Overlap Length Effect	77
6.2.4 Adhesive Fracture Energy Rate Effect	79
6.3 Adhesive Damage Model Analysis.....	81
6.4 Parameter Normalization for Dimensional Analysis	87
7. Conclusion.....	90
References	92
Appendices	96

List of Figures

Fig. 2.1. Practical examples of adhesive fastening in supported core constructions	21
Fig. 2.2 Comparison of cryogenic and low temperature adhesives	23
Fig. 2.3 Stress distributions along the bond-line of adhesive layer for various loading conditions	24
Fig. 2.4. (a) Dependence of strength of a single lap joint on overlap and adherend thickness ratio under the action of uni-axial tensile loading. (b) Dependence of shear strength on bond width and bond overlap. Strength increases linearly with increasing joint width. The increase in strength with increasing overlap is gradual; after a particular overlap is reached, there is no further increase in joint strength	25
Fig. 4.1 The bilinear cohesive traction-separation law	31
Fig. 4.2 Normalized separation strength with respect to toughness and adhesive thickness ratios	36
Fig. 4.3 Normalized total fracture energy as a function of toughness and adhesive thickness ratio	36
Fig. 4.4 Adhesively bonded single lap joint geometry according to ASTM D1002.....	37
Fig. 4.5 True stress-strain diagrams of each steel adherend constructed using power-law hardening mode.....	39
Fig. 4.6 Approximated stress-strain diagram of ductile epoxy adhesives using the Eq. 4.17 for various Young's modulus values and 30MPa tensile strength	40
Fig. 4.7 Schematic illustration of mesh structure of single lap joint geometry constructed with two-dimensional plane strain elements	42
Fig. 4.8 Boundary conditions and loading of the numerical model	43
Fig. 4.9 A simple flowchart representing the progressive failure model of the cohesive layer for FE analysis	45
Fig. 5.1 The tensile test geometry of metallic specimen.....	47
Fig. 5.2 True and engineering tensile test results of S235-JRG1 structural steel adherend.....	48

Fig. 5.3 The mould design representing the dimensions of the bulk adhesive specimen according to EN-ISO 527-2	49
Fig 5.4 Uni-axial tensile testing system with mechanical extensometer for the bulk adhesive samples.....	49
Fig. 5.5 Experimental and analytical stress-strain curves of bulk Veropal HE-20 adhesive	50
Fig. 5.6 Experimental and analytical stress-strain curves of bulk Carboresin brittle adhesive....	50
Fig. 5.7 Schematic diagram of a) Mode I DCB specimen and b) manufactured Mode I DCB specimen (side view).....	51
Fig. 5.8 Force versus crack opening displacement diagrams of mode I DCB test for the ductile and brittle adhesives.....	52
Fig. 5.9 End notched flexure (ENF) specimen geometry for Mode II interlaminar fracture test.	53
Fig. 5.10 Experimental setup for three point bending testing of the ENF specimen	53
Fig. 5.11 Load versus vertical deflection diagrams of Mode II ENF test specimens	54
Fig. 5.12 The manufactured single lap joint coupons according to ASTM D1002 standard.....	55
Fig. 5.13 Experimental setup for testing strength of the single lap joints.....	58
Fig. 5.14 Experimental load and cross-head displacement curves of the single lap joints bonded with Carboresin	59
Fig. 5.15 Experimental load and cross-head displacement curves of the single lap joints bonded with Veropal HE-20.....	59
Fig 5.16 Numerical axial loads of the V series joint configurations against axial displacement.	60
Fig 5.17 Numerical axial loads of the C series joint configurations against axial displacement.	61
Fig 5.18 The distribution of errors reference to experimental data for each single lap joint configuration	62
Fig. 6.1 Normalized peeling stress distribution over the bonded length at t=1mm	67
Fig. 6.2 Normalized peeling stress distribution over the bonded length at t=2mm	67
Fig. 6.3 Normalized peeling stress distribution over the bonded length at t=3mm	68
Fig. 6.4 The peak values of normalized peeling stresses (k_y) for each adherend thickness.....	68
Fig. 6.5 Normalized shear stress distribution over the bonded length at t=1mm.....	70
Fig. 6.6 Normalized shear stress distribution over the bonded length at t=2mm.....	70
Fig. 6.7 Normalized shear stress distribution over the bonded length at t=3mm.....	71
Fig. 6.8 The peak values of normalized peeling stresses (k_{xy}) for each adherend thickness	71

Fig. 6.9 Failure loads of the joints for the adherend yield stress of (a) $S_y=200\text{MPa}$ and (b) $S_y=300\text{MPa}$ having both identical adherend thickness of $t=1\text{mm}$ 73

Fig. 6.10 Failure loads of the joints for the adherend yield stress of (a) $S_y=200\text{MPa}$ and (b) $S_y=300\text{MPa}$ having both identical adherend thickness of $t=2\text{mm}$ 73

Fig. 6.11 Failure loads of the joints for the adherend yield stress of (a) $S_y=200\text{MPa}$ and (b) $S_y=300\text{MPa}$ having both identical adherend thickness of $t=3\text{mm}$ 74

Fig. 6.12 Graphical illustration of the adherend rigidity influence on the joint strength for $\sigma_a=15\text{MPa}$ 75

Fig. 6.13 Graphical illustration of the adherend rigidity influence on the joint strength for $\sigma_a=25\text{MPa}$ 76

Fig. 6.14 Graphical illustration of the adherend rigidity influence on the joint strength for $\sigma_a=40\text{MPa}$ 76

Fig. 6.15 3-D representation of overlap length influence on the joint strength as a function of adherend thickness and yield stress for the adhesive ultimate tensile stress of $\sigma_a=15\text{MPa}$ 77

Fig. 6.16 3-D representation of overlap length influence on the joint strength as a function of adherend thickness and yield stress for the adhesive ultimate tensile stress of $\sigma_a=25\text{MPa}$ 78

Fig. 6.17 3-D representation of overlap length influence on the joint strength as a function of adherend thickness and yield stress for the adhesive ultimate tensile stress of $\sigma_a=40\text{MPa}$ 78

Fig. 6.18 Normal (on the left) and shear (on the right) traction-separation lines of the adhesive at various fracture energy values for critical traction $\sigma_a=15\text{MPa}$ 79

Fig. 6.19 Normal (on the left) and shear (on the right) traction-separation lines of the adhesive at various fracture energy values for critical traction $\sigma_a=25\text{MPa}$ 80

Fig. 6.20 Normal (on the left) and shear (on the right) traction-separation lines of the adhesive at various fracture energy values for critical traction $\sigma_a=40\text{MPa}$ 80

Fig. 6.21 Numerical predicted uni-axial load versus displacement response and failure steps of the L10 single lap joint configuration 81

Fig. 6.22 Von-Mises stress distribution in the vicinity of the bonded area of the simulated L10 joint configuration (red is the maximum positive and blue is the minimum positive). The

a-d subplots correspond to the linear elastic, plastic, damage initiation and late stage damage propagation, respectively, as described in Fig. 6.20.....	82
Fig. 6.23 Numerical predicted uni-axial load versus displacement response and failure steps of the L20 single lap joint configuration	83
Fig. 6.24 Von-Mises stress distribution in the vicinity of the bonded area of the simulated L20 joint configuration (red is the maximum positive and blue is the minimum positive). The a-d subplots correspond to the linear elastic, plastic, damage initiation and late stage damage propagation, respectively, as described in Fig. 6.22.....	83
Fig. 6.25 Numerical predicted uni-axial load versus displacement response and failure steps of the L30 single lap joint configuration	84
Fig. 6.26 Von-Mises stress distribution in the vicinity of the bonded area of the simulated L30 joint configuration (red is the maximum positive and blue is the minimum positive). The a-d subplots correspond to the linear elastic, plastic, damage initiation and late stage damage propagation, respectively, as described in Fig. 6.24.....	85
Fig. 6.27 Numerical predicted uni-axial load versus displacement response and failure steps of the L40 and L50 single lap joint configurations.....	86
Fig. 6.28 Von-Mises stress distribution in the vicinity of the bonded area of the simulated L40 (on the left) and L50 (on the right) joint configurations (red is the maximum positive and blue is the minimum positive). The a-e subplots correspond to the linear elastic, plastic, damage initiation, late stage damage propagation and full debonding, respectively, as described in Fig. 6.26.....	86
Fig. 6.29 Variation of the joint efficiency (performance) corresponding to various dimensionless design parameters.....	88

List of Tables

Table 5.1 Mechanical properties (tensile test) and chemical composition of S235JRG1 steel adherend.....	47
Table 5.2 Dimension of the joint series in (mm) for Veropal HE-20 (V series) and Carboresin (C series)	56
Table 5.3 Cohesive zone material parameters of bulk adhesives for the numerical analysis	60
Table 5.4 Geometry and material design parameters of the single lap joint model for the FE parametric study.....	63

List of Symbols

K_0	$[N/mm^3]$	Initial stiffness
δ_c	$[mm]$	Critical separation
t_c	$[MPa]$	Traction stress
δ_f	$[mm]$	Fracture separation
K_{nn}	$[N/mm^3]$	Stiffness in normal direction
K_{ss}	$[N/mm^3]$	Stiffness in shear direction
K_{ns}	$[N/mm^3]$	Stiffness in transverse direction
E	$[GPa]$	Young's modulus
G	$[GPa]$	Shear modulus
σ_c	$[MPa]$	Critical cohesive strength in normal direction
τ_c	$[MPa]$	Critical cohesive strength in shear direction
$G_{I,II}$	$[N/mm]$	Fracture energy in Mode I and II
Γ	$[N/mm]$	Specific fracture energy
D	$[-]$	Damage index parameter
η	$[mm]$	Adhesive thickness
ε	$[mm/mm]$	Strain
U	$[N/mm^2]$	Toughness

θ	[°]	Angle with respect to crack plane
r_p	[mm]	Length of plastic zone
ν	[-]	Poisson's ratio
λ	[-]	Critical separation ratio
μ	[-]	Toughness ratio
n	[-]	Strain hardening exponent
σ_y	[MPa]	Yield strength
σ_t	[MPa]	True stress
ε_t	[mm/mm]	True strain
σ_u	[MPa]	Tensile strength
L_{czm}	[mm]	Length of process zone
L	[mm]	Overlap length
t	[mm]	Adherend thickness
F_c	[N]	Critical load
Δ	[mm]	Correction factor
a	[mm]	Initial crack length
b	[mm]	Specimen width
w	[mm]	Joint width
F_n	[N]	Numerical failure load
F_{ex}	[N]	Experimental failure load
k	[-]	Stress concentration factor
F_w	[N/mm]	Failure load per unit width
u	[mm]	Applied displacement

1

Introduction

Adhesive bonding techniques have been utilized in industry to join a great variety of components ranging in scale from very small electronic parts to large assemblies. Adhesive bonding has received an expanding interest in many industries, e.g. aerospace, automotive, composite materials, electronics, and railway vehicles, as an alternative to traditional joining methods such as welding, riveting, screwing, etc. The strength evaluation and failure analysis of adhesively bonded joints in various applications are important topics. Accordingly, great efforts have been made in finding the influences of material and geometrical parameters on the load carrying capacity of adhesive bonding structures, so as to design optimal structures with proper adhesives for practical requirements in engineering. Fracture mechanics is a common and essential tool for understanding and predicting the failure of machine components. For many years, researchers have been focusing on the durability of materials; the main approach for this is to identify when failure will occur. This mainly concerns nucleation and propagation of cracks in a body. The external load applied on the material could cause a crack to initiate, or could cause growth of an already existing crack and the presence of a crack could lead to rupture when the crack propagates directly through the body. To predict the strength of the adhesive bonding and where fracture will occur, the continuum damage mechanics or fracture mechanics is employed. In recent years, more attention has been paid on the fracture mechanic approach since simulation of crack initiation and propagation is out of the scope of the classical continuum damage mechanics. Moreover, the cohesive zone model approach is increasingly becoming the most popular field in predicting the failure phenomena in adhesive bonding structures.

2

Literature Review

2.1 History of Cohesive Zone Models

There are many traction separation laws [1, 2] proposed and successfully implemented to predict fracture behaviors. Various laws with specific attention focused on the shape and the value parameters of the models are as follows: Needleman used polynomial and exponential types of traction-separation equations to simulate particle debonding in metal matrices [3, 4]. Xu and Needleman [5] used the CZM models to study the void nucleation at the interface of particle and matrix material, fast crack growth in brittle material under dynamic loading, and dynamic crack growth along the interface of biomaterials. Tvergaard and Hutchinson [6] used a trapezoidal shape of the traction-separation model to calculate the crack growth resistance in elastic-plastic materials. Tvergaard [7] used a quadratic traction-displacement equation to analyze interfaces. Camacho and Ortiz [8] employed a linear cohesive fracture model to propagate multiple cracks along arbitrary paths during impact damage in brittle materials. Geubelle [9] utilized a bilinear CZM to simulate spontaneous initiation and propagation of transverse matrix cracks and delamination fronts in thin composite plates subjected to low-velocity impact. Among the various forms of cohesive laws, there is one common feature, i.e. as the cohesive surfaces separate, the traction first increases until a maximum is reached, and subsequently the traction decreases to zero, which results in complete separation. This holds for both the normal and the shear direction. The cohesive strength is usually related to the yield stress of the material involved [10]. It is also the maximum resistance to fracture. During the material separation process, energy is dissipated; this energy corresponds to the cohesive energy. The cohesive length introduces a length scale which enables mesh independent

simulation results. The traction-separation relations play an important role in the macroscopic mechanical response of the system [11]. Xu and Needleman's [5] exponential law is used for the numerical simulation in following sections. This model provides smooth traction- separation relation and is therefore more stable than the discontinuous models, such as the bilinear model.

2.2 Design of Adhesively Bonded Single Lap Joints

Epoxy adhesives, which are widely chosen for bonding process in terms of its applicability to a wide range of material types, become very popular regarding to its higher strength and temperature resistance among the other adhesives. They mainly consist of an epoxy resin plus a hardener. They allow great versatility in formulation since there are many resins and many different hardeners. Epoxy adhesives are available in one-part or two part form and can be supplied as flowable liquids, as highly thixotropic products with gap-filling capability of up to 25mm [11].

The increased application of adhesive joints was accompanied by the development of mathematical models in order to analyse the fracture behaviour of those joints. Both analytical and numerical models have been developed. Analytical models such as the oldest work proposed by Goland and Reissner [12] usually involve many simplifying assumptions. They introduced equations to predict the shearing and normal stresses in the adhesive layer as well as those in the jointed plates, assuming that the peel and shear stresses were constants across the adhesive thickness. In Cornell's work [13], a variation and extension of Goland and Reissner's method [12] was presented for determining the stresses in adhesive lap-joints. He assumes that the two lap-joint plates act like simple beam and the more elastic adhesive layer is an infinite number of shear and tension springs [14]. Hart-Smith has produced an enormous amount of work on continuum mechanics of adhesive joints, for example [14, 15, and 16].

For practical application of adhesively bonded joints, single lap joints are generally preferred to be analysed due to its ease of operation in many fields and assemblies. However, the peeling stresses generated on the edge of adhesive and adherent interfaces make estimation of failure load and strength difficult accompanied by the geometrical and material non-linearity [17]. In the previous works of literature, there are generally two outstanding methods; one is stress and strain based methods and the other is fracture mechanic approach. Stress and strain method considers some maximum and minimum values depending on the some failure criterion equations. For the estimation of failure loads, many researchers performed some numerical finite element analysis

[14-18] considering different material and failure behaviour. In these studies, some failure approaches such as elastic failure mechanism, failure envelope, cohesive zone modelling and some peak stress and strain values were proposed. On the other hand, for practical prediction of static strength of a single lap joint, implementation of fracture mechanics approach requires some information about the toughness, failure mode shape (cohesive, adhesive delamination and stress and strain singularities) that can be obtained early stage of design and manufacture. These methods are only applicable in the case of performing several experiments that increases cost the operation. The failure load of adhesively bonded joints is not only influenced by the geometry of the joints but also by material behaviour.

In the literature, most of researches focused on improving the strength of the joints, and some techniques were therefore developed in order to realize the aim. Some researches tried to explain adhesive strength by modifying the shape of the joints and investigating such as overlap length, adhesive bondline thickness [25, 26, 27 and 28]. Others presented the surface treatments on the overlap area before bonding [29, 30, 31 and 32].

Mahoney et al., [33] carried out numerical analysis (finite element method, FEM) by using a cohesive-zone model for the two adherend–adhesive interfaces and a continuum damage model for the bulk adhesive. He [34] has given an extensive review of finite element analysis of adhesively bonded joints. Damage modelling in adhesive joints has been classified into either local or continuum approaches. In the continuum approach the damage is modelled over a finite region. Where as in local approach, the damage is confined to zero volume lines and surfaces and is often referred to as cohesive zone approach [34]. Xu and Wei’s study [35, 36] aimed to perform a numerical model utilizing FEM is established to describe the mechanical behaviours of the single lap joints subjected to tensile loading. In spite of the fact that numerical investigations have been conducted using cohesive zone damage models in bonded joints mentioned as above, a predictive model is required to determine an mechanical properties of interfacial adhesion failure of bonded single lap joints corresponding to surface characteristic features.

2.3 Advantages of Adhesively Bonded Joints

The bond is continuous: On loading, there is more uniform distribution of stresses over the bonded area. The local concentrations of stresses present in spot welded or mechanically fastened joints are avoided. Bonded structures can consequently offer a longer life under load.

Stiffer structures: The bonded joint- being continuous- produces a stiffer structure. Alternatively, if increased stiffness is not needed, the weight of the structure can be decreased while maintaining the required stiffness.

Improved appearance: Adhesive bonding gives a smooth appearance to design. There are no protruding fasteners such as screws or rivets, and no spot-welds marks.

Complex assemblies: Complex assemblies often that cannot be joined together in any other feasible way with adhesives. Composite sandwich structures are a typical example.

Dissimilar materials: Adhesives can join different materials together- materials that may differ in composition, moduli, coefficients of expansion, or thickness.

Reduced corrosion: The continuous adhesive bond forms a seal. The joint consequently leak proof and less prone to corrosion.

Electrically insulating: The adhesive bond can provide usually an electrically insulating barrier between surfaces.

Reduced stress concentrations: The bonded structure is a safer structure because, owing to the fewer and less severe concentrations of stresses, fatigue cracks are less likely to occur. A fatigue crack in a bonded structure will propagate more slowly than in a riveted structure- or even in a machined profile because the bond-lines act as a crack stopper.

Joining sensitive materials: Adhesive bonding does not need high temperatures. It is suitable means for joining together heat-sensitive materials prone to distortion or to a change in properties from the heat of brazing or welding.

Vibration damping: Adhesive bonds have good damping properties. The capacity may be useful for reducing sound or vibration.

Simplicity: Adhesive bonding can simplify assembly procedures by replacing several mechanical fasteners with a single bond, or by allowing several components to be joined in one operation. Adhesive bonding may be used in combination with spot welding or riveting techniques in order to improve the performance of the complete structure. All these advantages may be translated into economic advantages; improved design, easier assembly, lighter weight (inertia overcome at low energy expenditure), longer life in service.

2.4 Limitations of Adhesively Bonded Joints

Temperature resistance: Adhesives are typically drawn from the class of materials which we know as ‘polymers’, ‘plastics’ or ‘synthetic resin’. They have the limitations of that class. They are not as

strong as metals. (The difference is offset by the increased surface contact area provided by the bonded joints). With increasing temperature the bond strength decreases and the strain properties of the adhesive move from elastic to plastic. This transition is usually in the temperature range 70-220°C; the transition temperature depends on the particular adhesive.

Chemical resistance: The resistance of bonded joints to the in-service environment is dependent on the properties of the polymer from which the adhesive is made. Possible exposure of the bonded structure to oxidizing agents, solvents, etc., must be kept in mind when selecting the adhesive type to use.

Curing time: With most adhesives maximum bond strength is not produced instantly as it is with mechanical fastening or with welding. The assembled joint must be supported for at least part of the time during which strength of the bond is building up. The quality of the bond may be adversely affected if, in the bonding process, the surfaces are not readily wetted by the adhesive.

Process controls: Ensuring consistently good results may necessitate the setting up of unfamiliar process controls. A badly made joint is often impossible to correct.

In service repair: Bonded assemblies are usually not easily dismantled for in-service repair.

2.5 Modern Adhesive Types and Main Characteristics

Modern adhesives are classified either by the way they are used or by their chemical type. The strongest adhesives solidify by a chemical reaction. Less strong types harden by some physical change. Key types in today's industrial scene are as follows.

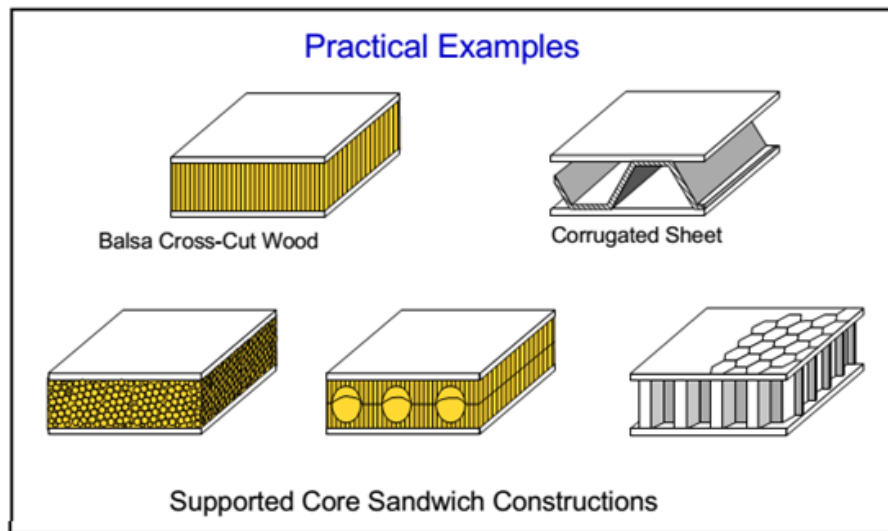


Fig. 2.1. Practical examples of adhesive fastening in supported core constructions [11].

Anaerobics: Anaerobic adhesives harden when in contact with metal and air is excluded, e.g. when a screw is tight in a thread. Often known as ‘locking compounds’ or ‘sealants’, they are used to secure, seal and retain turned, threaded, or similarly close-fitting parts. They are based on synthetic resins known as acrylics. Due to the curing process, anaerobic adhesives do not have gap-filling capability but have advantage of relatively rapid curing.

Cyanoacrylates: A special type of acrylic, cyanoacrylate adhesives cure through reaction with moisture held on the surfaces to be bonded. They need close-fitting joints. Usually they solidify in seconds and are suited to small plastic parts and to rubber. Cyanoacrylate adhesives have relatively little gap-filling capability but can be obtained in liquid and thixotropic (non-flowing) versions.

Toughened Acrylics/Methacrylates: A modified type of acrylic, these adhesives are fast-curing and offer high strength and toughness. Supplied as two parts (resin and catalyst), they are usually mixed prior to application, but specialized types are available which are applied by separate application: resin to one bond surface, catalyst to the other. They tolerate minimal surface preparation and bond well to a wide range of materials. The products are available in a wide range of cure speeds and as liquids or pastes which will gap-fill up to 5mm.

UV curable adhesives: Specially modified acrylic and epoxy adhesives, which can be cured very rapidly by exposure to UV radiation. Acrylic UV adhesives cure extremely rapidly on exposure to UV, but require one substrate to be UV transparent. The UV initiated epoxy adhesives can be irradiated before closing the bondline, and cure in a few hours at ambient temperature or may be cured at elevated temperature.

Epoxies: Epoxy adhesives consist of an epoxy resin plus a hardener. They allow great versatility in formulation since there are many resins and many different hardeners. They form extremely strong durable bonds with most materials. Epoxy adhesives are available in one-part or two-part form and can be supplied as flowable liquids, as highly thixotropic products with gap-filling capability of up to 25mm, or as films.

Polyurethanes: Polyurethane adhesives are commonly one part moisture curing or two-part. They provide strong resilient joints, which are resistant to impacts. They are useful for bonding GRP (glass fibre-reinforced plastics) and certain thermoplastic materials and can be made with a range of curing speeds and supplied as liquids or with gap-filling capability of up to 25mm.

Modified Phenolics: The first adhesives for metals, modified phenolics now have a long history of successful use for making high strength metal-to-metal and metal-to-wood joints, and for bonding metal to brake-lining materials. Modified phenolic adhesives require heat pressure for the curing process.

Plastisols: Plastisol adhesives are modified PVC dispersions which require heat to harden. The resultant joints are often resilient and tough.

Rubber adhesives: Based on solutions of latexes, rubber adhesives solidify through loss of solvent or water. They are not suitable for sustained loading.

Polyvinyl Acetates (PVAs): Vinyl acetate is the principal constituent of the PVA emulsion adhesives. They are suited to the bonding of porous materials, such as paper or wood, and general packaging work.

Pressure-sensitive adhesives: Suited to use on tapes and labels, pressure-sensitive adhesives do not solidify but are often able to withstand adverse environments. They are not suitable for sustained loading. The shear strength properties of these type adhesives are presented in Fig. 2.2 depending on varying temperature range to have an idea of possibility of implementing in practical applications.

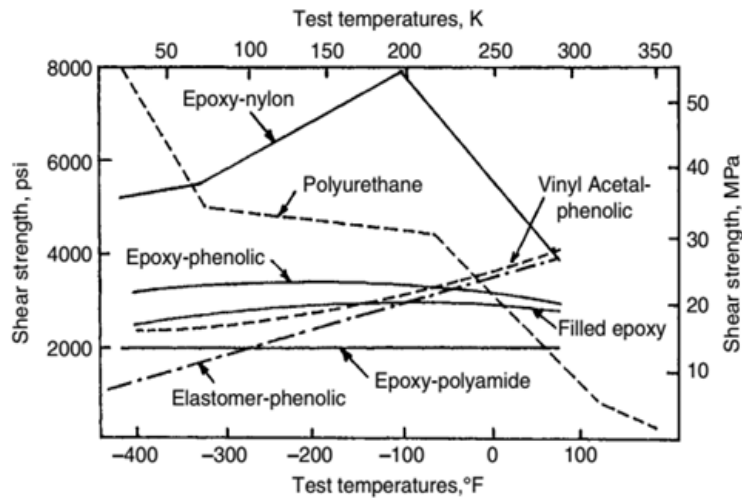


Fig. 2.2 Comparison of cryogenic and low temperature adhesives [12].

2.6 Methods of Improving the Joint Efficiency

As mentioned earlier, joints should be specifically designed for adhesive bonding. Figure 2.2 illustrates various types of adhesive joints used for flat adherends. Adhesive bonds designed to

follow the following general principles will result in maximum effectiveness; the bonded area should be as large as possible within the allowable geometry and weight constraints. A maximum percentage of the bonded area should contribute to the strength of the joint. The adhesive should be stressed in the direction of its maximum strength. Stress should be minimized in the direction in which the adhesive is weakest. Thermosetting adhesives, such as epoxies, are relatively rigid and exhibit high tensile and shear strength under both dynamic loading and static loading. Such adhesives also have good fatigue resistance. However, rigid brittle adhesives are not recommended for bonds stressed in peel or cleavage. Elastomeric adhesives, on the other hand, have low tensile or shear strength, but these adhesives develop high peel or cleavage strength. Adhesives that possess high tensile and shear strength over short periods of static stress give poor results over longer periods or under vibrating stresses.

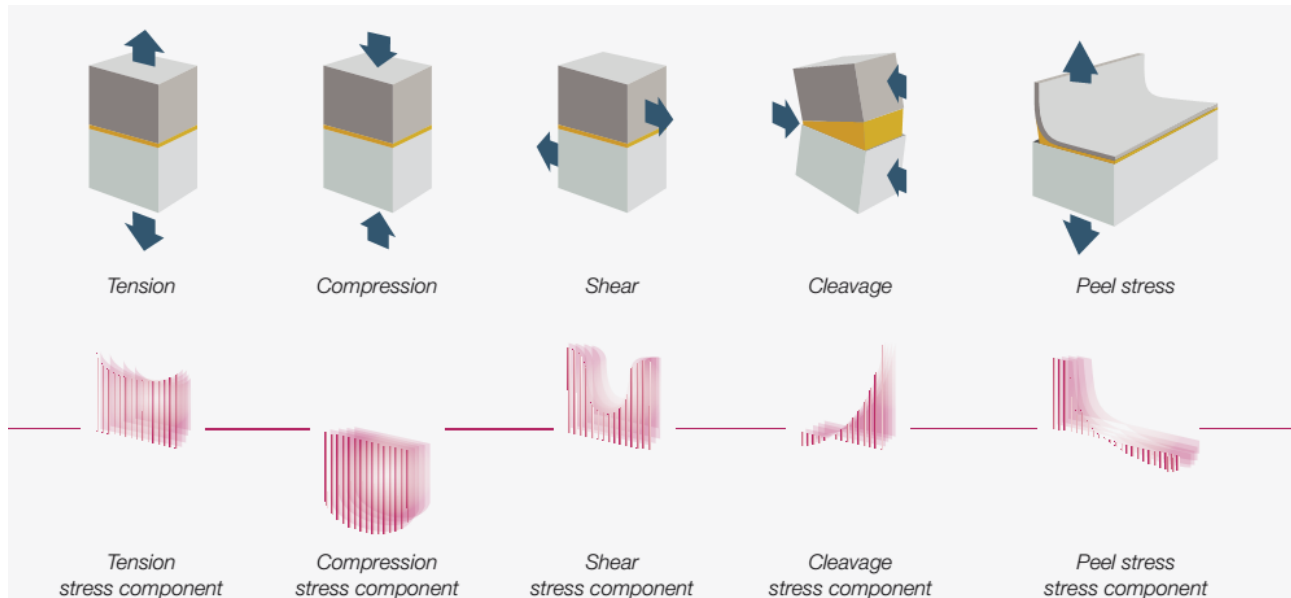


Fig. 2.3. Stress distributions along the bond-line of adhesive layer for various loading conditions [11].

Compression

When loaded in pure compression, a joint is less likely to fail than when loaded in any other manner, but compression-loaded joints are limited in application.

Tension

This type of loading imposes an even stress across the whole bonded area, utilizing the joint area to the best advantage and providing an economical joint that is most resistant to joint failure. Whenever possible, most of the load should be transmitted through the joint as a shear load.

Shear

The strengths of joints loaded in tension or shear are comparable. As in shear, the stress is evenly distributed over the joint area, but it is not always possible to be sure that other stresses are not present. If the applied load is offset to any degree, the advantage of an evenly distributed stress is lost and the joint is more likely to undergo failure. The adherends should be thick with this type of joint and not likely to deflect to any appreciable degree under the applied load. Such a situation will result in non-uniform stress. Tensile stress develops when forces acting perpendicular to the plane of the joint are distributed uniformly over the entire area of the bond. The types of stress likely to result when other than completely axial loads are applied are cleavage and peel. As adhesives generally have poor resistance to cleavage and peel, joints designed to load the adhesive in tension should have physical restraints to ensure axial loading.

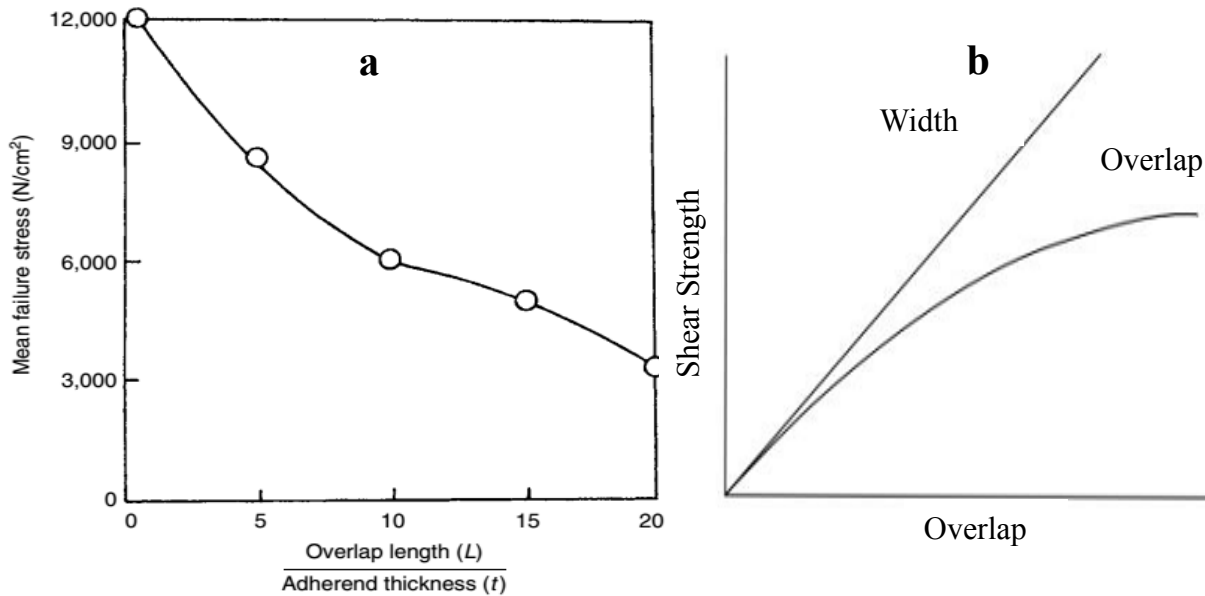


Fig. 2.4. (a) Dependence of strength of a single lap joint on overlap and adherend thickness ratio under the action of uni-axial tensile loading. (b) Dependence of shear strength on bond width and bond overlap. Strength increases linearly with increasing joint width. The increase in strength with increasing overlap is gradual; after a particular overlap is reached, there is no further increase in joint strength [37].

Peel

One or both of the adherends must be flexible in this type of loading. A very high stress is applied to the boundary line of the joint, and unless the joint is wide or the load is small, failure of the bond will occur. This type of loading is to be avoided if possible.

Cleavage

Cleavage is somewhat similar to peel and occurs when forces at one end of a rigid bonded assembly act to split the adherends apart. It may be considered as a situation in which an offset tensile force or a moment has been applied. The stress is not evenly distributed (as is the case with tension) but is concentrated on one side of the joint. A sufficiently large area is needed to accommodate this stress, resulting in a more costly joint.

3

Objectives of the Dissertation

3.1 Motivation

The strength of adhesive bonding or joints strongly depends on the direction and distribution of the stresses as a result of applied load. There are mainly three kind of stresses such as shear, peeling and tension stresses in adhesively bonded lap joints. In the failure analysis, these stresses should be carefully considered in order to determine source of the failure. There are also other effective factors directly changing the stress and strain behavior of the adhesive joints. These factors are commonly nonlinear adherend and adhesive behavior, type of the joint, (i.e. single lap, double lap, scarf and so on) and nature of the loading. Today, predicting the strength of adhesive joint are becoming the most popular and essential subject among them. For this reason, there have been many approaches by many authors in the literature. But most of them are restricted to simple approaches assuming linear elastic material properties for adherend or adhesive material. Furthermore, continuum damage mechanics have been the main tool to assess failure phenomena in the adhesive joints. Many of the proposed theories depend on the analytical closed form solutions, which excludes large displacement effects and non-linear material response. In this regard, a more efficient approach should be implemented to realize failure analysis of more complicated material and geometry responses to stimulate the reality. On the other hand, it would be unreasonable to perform experimental failure analysis for a variety of the different joint configurations in terms of manufacture effort, process control, waste of time and cost. To predict failure load of bonded structures, a fracture mechanics approach is introduced instead of classical damage mechanics models in this thesis.

3.2 The Theoretical Part

In this study, the failure loads of the adhesively bonded single lap joints is investigated employing a fracture mechanic approach. FE method is utilized with an appropriate method which is called “Cohesive zone model”. This progressive failure model is applied on different joint configurations and adhesive materials. In the scope of the thesis, following items are aimed to make a contribution on the precise estimation of failure load;

- Employing elastic-plastic adherend material in the progressive failure analysis to understand influence of plasticity on the joint strength for some kind of structural steels as a substrate material. Accordingly, developing a mathematical formulation to express nonlinear material model of the adherend up to fracture point then using it in FE solutions.
- Similarly, proposing a simple mathematical relation for both ductile and brittle epoxy adhesives to construct their stress and strain diagrams in terms of modulus of elasticity and ultimate tensile strength. Particularly, it is intended to obtain stress-strain diagram of various adhesives using this approach then ease of application in analytical and FE solutions. Thus, conducting many tensile tests of bulk adhesive samples would be no longer essential, which provide ease of application in practice.
- The thickness of adhesive layer is one of the important parameter in the adhesive joint design. Its influence on the joint strength, toughness and stiffness should be understood as much as possible. For this purpose, some general information about the adhesive layer thickness influence are aimed. Therefore, variation of adhesive strength, stiffness and fracture energy with respect to thickness parameter are intended to be evaluated.
- Replacing the adhesive layer by a zero thickness cohesive zone model to see how the joint strength and induced stress distribution in the vicinity of bonded area are affected. Because in practical applications, applying thinner adhesive layer as much as possible is suggested in the many literature surveys. Although it seems not feasible to manufacture zero thickness adhesive layer in practice, the change in the adhesive joint design parameters can be demonstrated as a function of critical thickness value.
- Expressing how the design parameters such as adhesive tensile strength, stiffness, fracture energy rate, adherend rigidity and yield point affect the load carrying capacity of the adhesive joints. Additionally, deriving the normalized design parameters for the adhesive

joint manufacture and finding their optimum range for an efficient joint design are expected to be searched. The possibility of establishing a simple analytical relation to evaluate the joint strength or efficiency is one of the point of interest in the scope of the thesis.

3.3 The Experimental Part

A series of the experiments are conducted during the study concerning the behavior of the bulk adhesive materials and the joint characterization. The purpose and contribution of each experiment are described in the following items;

- Validating the developed mathematical expressions for stress versus strain diagrams of ductile and brittle epoxy adhesives to see how the experimental data fit the theoretical results. To perform this task, two kinds of epoxy adhesives; Veropal HE-20 and Carboresin are chosen which represent ductile and brittle behavior, respectively.
- Similar to previous item, the same procedure is aimed to follow for the adherend material. The engineering and true stress-strain diagrams for a structural steel “S235” are to be performed for the comparison purposes. In the scope of the thesis, the single lap joints with structural mild steel adherends are planned to be the major topic. For this reason, all the results and governed equations are expected to be valid for the adhesive joints with the structural steel adherends.
- The failure loads obtained from progressive FE simulations must be validated for variety of the adhesive joint configurations. This enables possibility of comparison how the employed FE model approximates the experimental failure loads. Therefore, some joint configurations are intended to be manufactured for ductile and brittle adhesives. The cohesive zone parameters which are required to input FE analysis are to be determined by the corresponded experiments. The details of each experiment types and procedures are extensively mentioned in the following chapters of the thesis.

4

Material Nonlinearity and Description of Progressive Failure Model

4.1 Cohesive Zone Damage Model

In this study, the bi-linear traction-separation cohesive law is employed for the progressive failure analysis and predicting of failure mechanism of adhesive layer. Fig. 4.1 demonstrates this cohesive law with the key points O, A, B, C and D. At point O, the joint is not loaded and there is no separation. Through the path OA, the joint is loaded but no material damage is appeared so that unloading is completely reversible. The slope K (the initial cohesive stiffness) is usually chosen to be large so that the separation is small. At point A (with separation δ_c) the cohesive traction reaches the maximum allowable value (the cohesive strength) denoted by t_c . Beyond point A, material damage occurs and the cohesive stiffness is reduced. For example, at an arbitrary point B (with separation, δ_i) between points A and C, the unloading path goes linearly towards point O instead of going back to point A and then to point O. The cohesive stiffness drops down from the initial value K to the current value K_i and the allowable traction drops down from the initial cohesive strength t_c to the current value t_i . When the allowable traction drops down to zero at point C (which corresponds to the current physical crack tip), the separation is equal to δ_f and complete material separation occurs. Then either a new crack is nucleated (when a crack does not already exist) or the tip of an existing crack propagates [38].

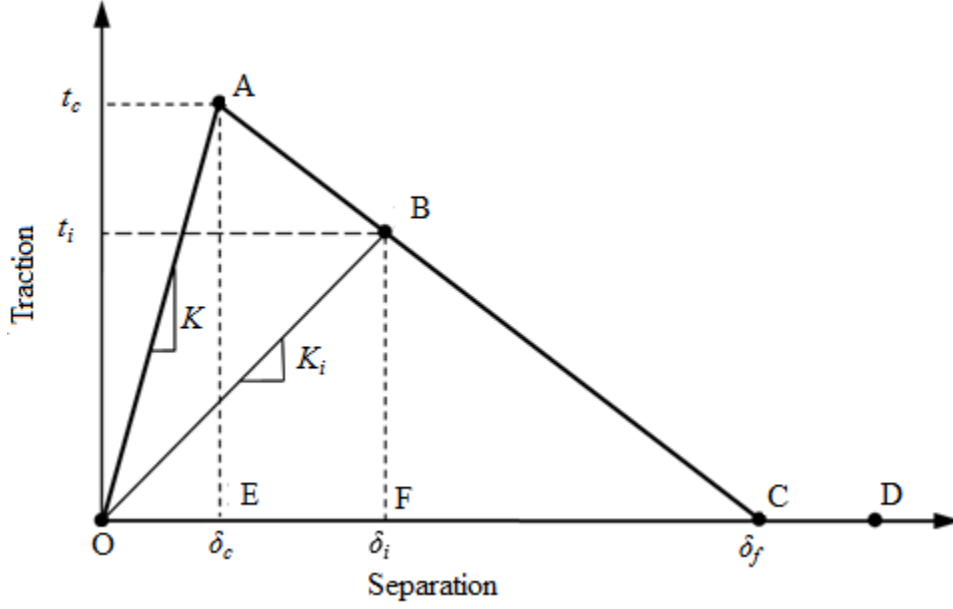


Fig. 4.1 The bilinear cohesive traction-separation law.

The traction–separation law assumes an initial linear elastic behaviour followed by linear evolution of damage. Elasticity is defined by an elastic constitutive matrix relating stresses and strains across the adhesive interface [39].

$$t = \begin{Bmatrix} t_n \\ t_s \end{Bmatrix} = \begin{bmatrix} K_{nn} & K_{ns} \\ K_{ns} & K_{ss} \end{bmatrix} \cdot \begin{Bmatrix} \delta_n \\ \delta_s \end{Bmatrix} = K \delta \quad (4.1)$$

The matrix K contains the stiffness parameters of the adhesive layer, given by the relevant elastic moduli. A suitable approximation for thin adhesive layers is provided with $K_{nn}=E$, $K_{ss}=G$, $K_{ns}=0$; E and G are the longitudinal and transverse elastic moduli, respectively [40]. In single lap joint configuration, both peeling (Mode I) and shear (Mode II) stresses play an important role in the failure mechanism. In this case, damage initiation in mixed-mode condition is evaluated by a quadratic stress criterion including the traction stress components (t^n , t^s) and the critical cohesive strengths (σ_c , τ_c), as shown in Eq. (4.1). σ_c and τ_c represent the critical stresses in normal and shear directions, respectively. $\langle \cdot \rangle$ are the Macaulay brackets such that $\langle x \rangle = 0.5(x + |x|)$, emphasizing that a purely compressive stress state does not initiate damage.

$$\left(\frac{\langle t^n \rangle}{\sigma_c} \right)^2 + \left(\frac{t^s}{\tau_c} \right)^2 = 1 \quad (4.2)$$

Crack growth of the cohesive layer is evaluated by a linear criterion considering the energy release rates (G_I, G_{II}) and the fracture toughnesses (Γ_I, Γ_{II}), as shown in Eq. (4.3). Damage initiation at a given element starts when the equality of Eq. (4.2) is satisfied, and complete separation occurs ruled by Eq. (4.3) in a similar way. The shape of the traction–separation law for each mode is defined as a bilinear model, as shown in Fig. 1, with three cohesive parameters: fracture toughness (Γ), critical cohesive stress (σ_c, τ_c) and initial stiffness (K_n, K_s).

$$\frac{G_I}{\Gamma_I} + \frac{G_{II}}{\Gamma_{II}} = 1 \quad (4.3)$$

The cohesive zone model in pure modes I and II is constructed using the Double Cantilever Beam (DCB) test and the End Notched Flexure (ENF) test, respectively. More extended information about the damage evaluation index parameter D and employment of the progressive failure algorithm are given in the following sections. For failure estimation, mixed mode approach is employed to well prediction of failure loads. Main structure of the mixed mode model is to be further extended in FE simulation details section.

4.2 Thickness-Dependence Cohesive Parameters

As the bilinear cohesive zone model is employed for progressive failure simulation of the adhesive, three cohesive zone parameters are required in normal and shear directions. These parameters are the initial stiffness, fracture toughness and critical separation strength for each aforementioned pure mode directions. However, these parameters would be highly influenced by the adhesive thickness. For example, it is quite difficult to obtain uniform thickness over a large bonded area in practical application of bonded structures, so that it may lead to an unexpected failure. To capture thickness effect on the cohesive zone parameters, the relationship between these parameters and thickness would be presented in this section.

4.2.1 Initial Stiffness

The initial stiffness of CZ model represents the slope value of the rising part of the traction separation curve shown in Fig. 4.1. It is used to describe the ratio between the cohesive stress and separation displacement before the adhesive damage occurs, which is quite similar to the stiffness coefficient of a spring. Obviously, the initial stiffness is dominated by the elastic properties together

with the adhesive thickness η . Based on the present investigation, initial stiffnesses in normal and shear directions can be described as;

$$K_0^n = \frac{E}{\eta} \quad \text{and} \quad K_0^s = \frac{G}{\eta} \quad (4.4)$$

where E and G denote the Young's modulus and shear modulus, respectively. The relation between the separation strength σ_c and critical separation displacement δ_c could be obtained;

$$\delta_c^n = \frac{\eta\sigma_c}{E} \quad \text{and} \quad \delta_c^s = \frac{\eta\tau_c}{G} \quad (4.5)$$

In this expression, it is quite clear that the critical separation displacement at the damage initiation is linearly dependent to thickness of the adhesive layer. Contrary, initial thickness value changes adversely with the increasing adhesive thickness. Obviously, it is an indication of ductile to brittle material transition response of cohesive layer as the thickness gets thinner.

4.2.2 Total Fracture Energy

In general, the mixed total fracture energy of CZM can be evaluated by Eq. (4.6) considering the adhesive layer as an equivalent cohesive layer. In other word, the adhesive layer with a certain thickness dissipates two types of energies, including the cohesive energy Γ_0 and plastic dissipation energy Γ_p , which denote the energy making the adhesive layer separated and the energy dissipated during the plastic deformation, respectively. Therefore, the total fracture energy Γ can be expressed

$$\Gamma = \Gamma_0 + \Gamma_p \quad (4.6)$$

where Γ_p can be obtained by integrating the work density through the adhesive layer thickness

$$\Gamma_p = \int_0^\eta \left(\int_0^\varepsilon \sigma d\varepsilon \right) d\eta \quad (4.7)$$

Where ε is strain component through the thickness of adhesive layer corresponding to relevant stress component of σ . For relatively small adhesive thickness, Γ_p can be simplified to below Eq. 4.8 assuming that the thickness is smaller than plastic zone height in front of crack tip.

$$\Gamma_p \approx \eta U \quad (4.8)$$

Where U is the area under stress strain curve of bulk adhesive. In reality, the plastic dissipation Γ_p is significantly influenced by the plastic zone height that would be constrained by the adhesive thickness [6, 11, 14, and 15]. The length that scales the plastic dissipation zone in front of crack tip, for the plane strain small-scale yielding condition, is expressed as [41]

$$r_p(\theta) = \alpha(\theta) \frac{1}{3\pi} \frac{E}{1-\nu^2} \frac{\Gamma_0}{\sigma^2} \quad (4.9)$$

where θ is the angle with respect to the crack plane. The maximum length of plastic zone is evaluated for $\theta=90^\circ$. Hence, $\alpha(90^\circ)$ can be regarded as equal to r_p^{\max} . When the adhesive thickness is smaller than the plastic zone length, the plastic dissipation energy is obtained by Eq. (4.8), and when the adhesive thickness is larger than the plastic zone length, the plastic dissipation energy would keep at a constant value dominated by r_p^{\max} [42]. Based on the above statement, the total fracture energy would be expressed by

$$\Gamma = \Gamma_0 + \Gamma_p = \begin{cases} \Gamma_0 + \eta U, & \eta < 2r_p^{\max} \\ \Gamma_0 + 2r_p^{\max} U, & \eta \geq 2r_p^{\max} \end{cases} \quad (4.10)$$

4.2.3 Separation Strength

Separation strength refers to maximum cohesive stress between crack planes at the tip of crack. Its value significantly changes for various adhesive thicknesses and should be taken into account for simulating proper crack propagation in adhesive layer. Therefore, based on the bilinear traction separation law shown in Fig. 4.1, the constitutive relations can be derived as following using fracture energy.

$$\sigma_c = \frac{2\Gamma}{\delta_f} \quad (4.11)$$

A dimensionless critical separation ratio $\lambda=\delta_c/\delta_f$ which is almost regardless of adhesive thickness would be introduced. Thus, substituting critical separation ratio and $\delta_c=\sigma_c/K_0$ in Eq. (4.11) gives;

$$\sigma_c = \sqrt{2\lambda K_0 \Gamma} \quad (4.12)$$

Cohesive zone model simulates relatively small thicknesses comparing to adhesive thickness. Furthermore, separation strength σ_c is larger than the bulk adhesive strength σ_u until a critical thickness value of the adhesive η_c is reached. Beyond this critical thickness value corresponding to initial stiffness K_0 , the separation and bulk adhesive strength become nearly identical. Thus λ could be rewritten

$$\lambda = \frac{\delta_c}{\delta_f} = \frac{\sigma_u/K_0}{2(\Gamma_0 + \eta_c U)/\sigma_u} = \frac{\sigma_u^2}{2K_0(\Gamma_0 + \eta_c U)} \quad (4.13)$$

Substituting equation (4.13) into equation (4.12) and introducing dimensionless intrinsic energy parameter, namely $\mu = \eta_c U / \Gamma_0$ concludes

$$\frac{\sigma_c}{\sigma_u} = \sqrt{\frac{K_0 \Gamma}{K_0(\Gamma_0 + \eta_c U)}} = \sqrt{\frac{\frac{\Gamma}{\Gamma_0}}{\left(1 + \frac{\eta_c U}{\Gamma_0}\right) \left(\frac{\eta}{\eta_c}\right)}} = \begin{cases} \sqrt{\frac{1 + \mu \left(\frac{\eta}{\eta_c}\right)}{(1 + \mu) \left(\frac{\eta}{\eta_c}\right)}}, & \eta < \eta_c \\ 1, & \eta \geq \eta_c \end{cases} \quad (4.14)$$

In the same way, using the dimensionless intrinsic energy parameter the total fracture energy relation can be simplified into the form deduced from equation (4.10)

$$\frac{\Gamma}{\Gamma_0} = \begin{cases} \frac{1 + \mu \left(\frac{\eta}{\eta_c}\right)}{(1 + \mu)}, & \eta < \eta_c \\ 1, & \eta \geq \eta_c \end{cases} \quad (4.15)$$

Here, it is readily pointed out that the parameter μ plays an important role in controlling both fracture energy and separation strength. In fact, μ is an indication of toughness of the adhesive layer, which is higher for higher μ . For an extensive understanding of influence of the thickness on the cohesive zone model parameters, some graphical representations would be given.

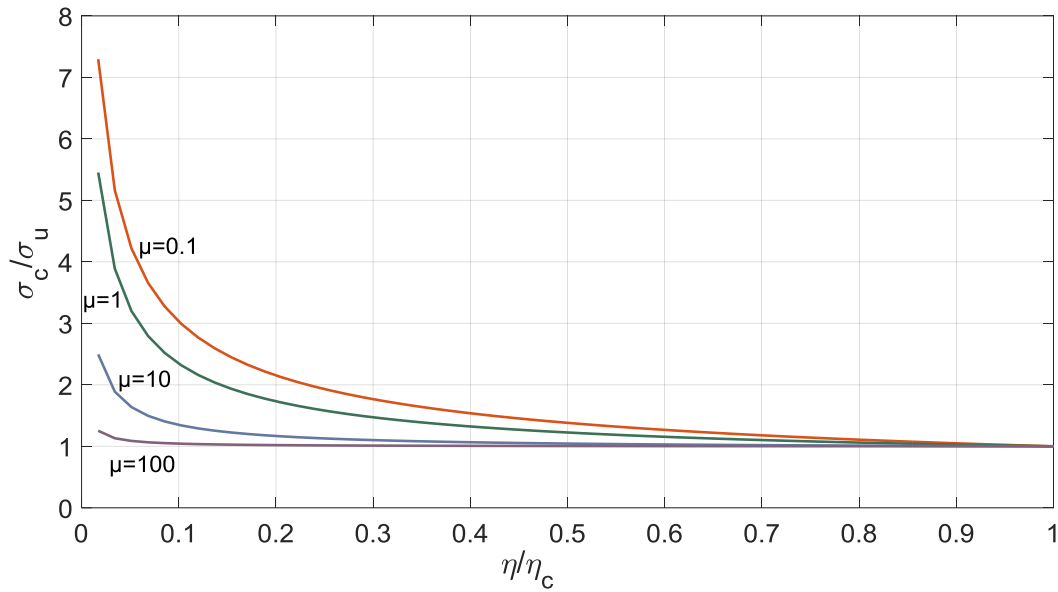


Fig. 4.2 Normalized separation strength with respect to toughness and adhesive thickness ratios.

As the adhesive thickness is increased, normalized separation strength sharply drops down for relatively lower toughness values (e.g. $\mu=0.1$). Contrary, at higher toughness values (e.g. $\mu=100$), the bulk strength of the adhesive becomes less dependent to the thickness ratio. It is noted that employing relatively small adhesive thicknesses lead better joint separation strength up to nearly 8 times larger than that of bulk sample (see Fig. 4.2). Furthermore, ductile adhesives

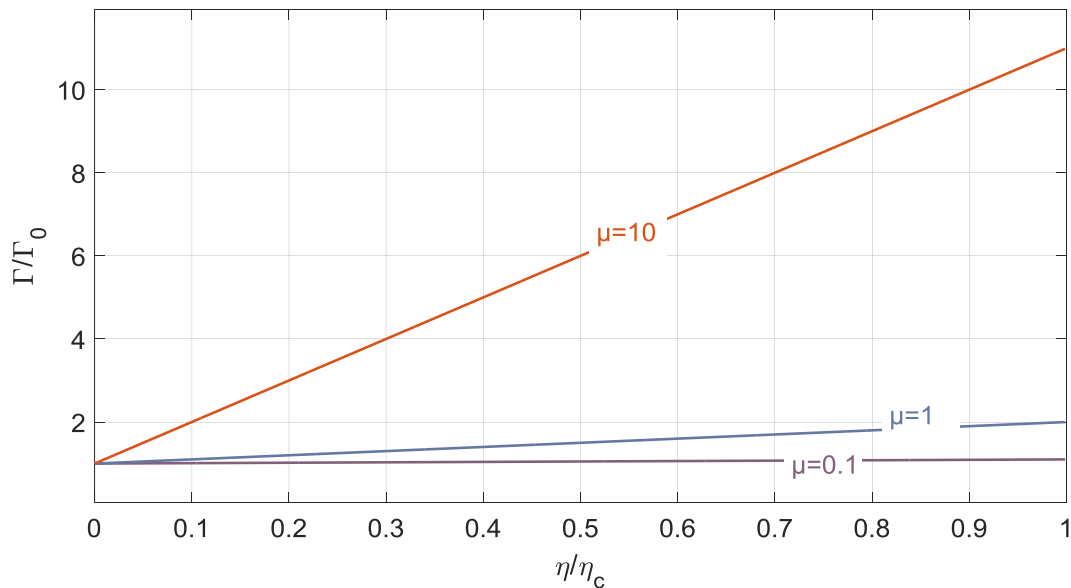


Fig. 4.3 Normalized total fracture energy as a function of toughness and adhesive thickness ratio.

(corresponding to high μ values) has the separation strength which are almost the identical at different thicknesses. In opposition, total fracture energy values (in Fig. 4.3) rises significantly at relatively high toughness values (e.g $\mu=10$). The thickness value becomes increasingly dominant for larger μ values whereas its influence roughly disappears as the μ getting smaller shown in Fig. 4.3.

4.3 Material and Geometry Description

Both material behaviour and single lap joint configuration has a significant influence on the estimation of failure load and simulating crack propagation. Many analytical continuum failure prediction assumes elastic adhesive and adherend material response and nearly ignores nonlinear geometrical stiffness variation due to the eccentricity of loading path. For a better evaluation of damage occurrence and progressive failure concept, both material response and nonlinear geometrical effects should be precisely introduced in the failure analysis. Therefore, the joint geometry and material model of individual components of single lap joint would be described in the upcoming section.

4.3.1 Single Lap Joint Geometry

Single lap joint geometry which exhibits over a range of usage area and popularity among the researchers was selected to be joint geometry. Joint geometry model was designed in accordance with the ‘‘ASTM D1002’’ [43] (Standard Test Method for Apparent Shear Strength of Single-Lap-Joint Adhesively Bonded Metal Specimens by Tension Loading) and thickness of the adherend is controlled to be in the range of 0.1mm and 0.15 mm and width of the joint is 25mm as stated in the standard. The schematic illustrations of single lap joint geometry with the dimensions are given in Fig. 4.4.

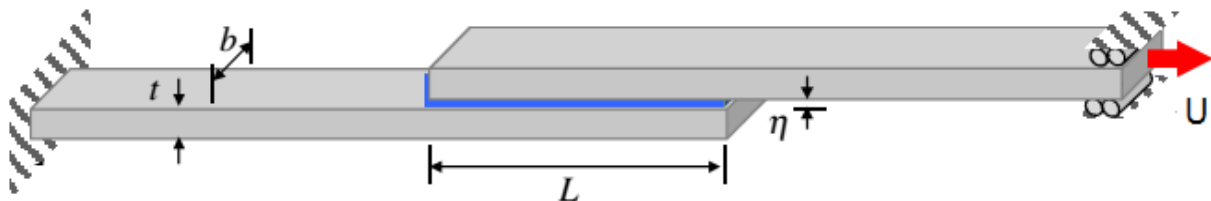


Fig. 4.4 Adhesively bonded single lap joint geometry according to ASTM D1002 [43].

The thickness of adhesive layer is measured using a micrometre after manufacture of the single lap joints. Then the exact cohesive parameters such as separation strength, fracture energy and initial stiffness are evaluated corresponding to experimental thickness value using the equations in section 4.2. The strength of the bonded lap joints generally varies linearly proportional to width of joint so that only one fixed value of joint width is sufficient for failure evaluation.

4.3.2 Adherend Material Model

In order to capture the effect of elasto-plasticity of adherend material, a nonlinear material model is employed with isotropic hardening. In the study, the most common type of structural steels with low carbon content and high ductility is selected as the adherend material. The metallic adherends are modelled as elasto-plastic solids, with their true stress-strain curves using power-law hardening laws.

$$\sigma = \begin{cases} E\varepsilon, & \varepsilon \leq \sigma_y/E \\ \sigma_y \left(\frac{\varepsilon}{\sigma_y/E} \right)^n, & \varepsilon > \sigma_y/E \end{cases} \quad (4.16)$$

where E is the Young's modulus, n is the strain hardening exponent, and σ_y is the yield strength. For the present model, the metallic adherends are assumed to be the S235 structural mild steel with a minimum yield stress of 235MPa and Young's modulus of 200GPa. The strain hardening exponent "n" for structural mild steels, corresponding to an average fracture elongation of 25% and ultimate tensile strength of 400MPa, is evaluated approximately 0.1 using the Eq. 4.16 . Three different structural steels, namely S255, S275 and S355 for the parametric study are implemented. Each has the minimum yield stress of 255, 275 and 355 N/mm², respectively. The other material parameters (e.g Young's modulus, strain hardening exponent) are kept constant for each of the corresponded structural steel. The true stress and strain curves of each steel adherend are presented in Fig. 4.5 using the constitutive stress strain relation in Eq. 4.16. In this way, estimation of the failure loads and damage evaluation behaviour of the single lap joint would be easy depending on only the yield stress of the metallic adherends. In other words, employing power law strain hardening model enables to define all the points in the plastic region introducing only two material parameters (e.g Yield stress and strain hardening exponent). In the numerical analysis, all the points of stress-strain diagram for each type of structural steel is imported to ABAQUS using a tabular data chart. As it can be inferred from Fig. 4.5, the yield stress of the steel adherend plays substantial

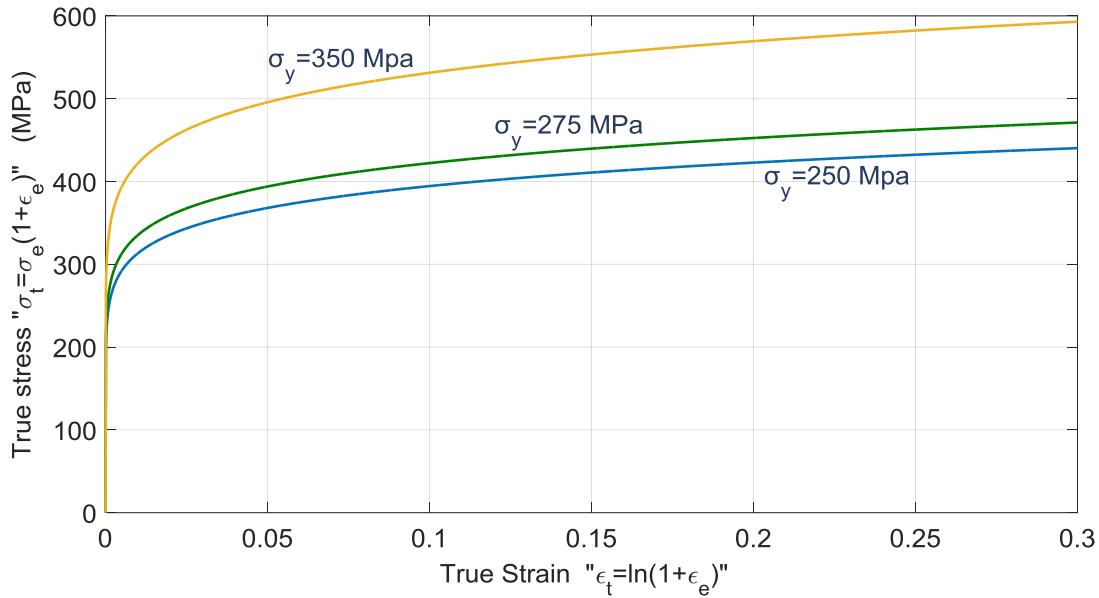


Fig. 4.5 True stress-strain diagrams of each steel adherend constructed using power-law hardening model.

role in determining the plastic behaviour of the single lap joint model. However, this approach is only limited to structural steels with low carbon content and high ductility up to 30% elongation. In the case of high or medium carbon steels, the strain hardening exponent would be highly affected.

4.3.3 Adhesive Material Model

In this study, the most commonly implemented epoxy adhesives are employed for the progressive damage analysis. Thus, there would be an analytical expression in order to describe stress-strain relations of an epoxy adhesive. For this reason two different formulation to construct stress-strain curve of both ductile and brittle behaviour are to be created. For instance, most of the soft (ductile) epoxy adhesives exhibit highly nonlinear trend up to tensile strength then nearly behave like a perfectly plastic material. Under these circumstances, following equation would be sufficient to construct stress-strain curve of soft epoxy adhesives.

$$\sigma_a = \sigma_u \tanh\left(\frac{E_a}{\sigma_u} \varepsilon_a\right) \quad (4.17)$$

Where σ_u is the adhesive tensile strength, E_a is the adhesive Young's Modulus and ε_a is the strain value at an arbitrary point on the stress-strain curve.

Additionally, the case is much more different for brittle or quasi-brittle type of structural epoxy adhesives. Generally, some of the brittle epoxies show a linear stress-strain variation up to fracture point. However, there is still no clear expression of transition from the brittle to ductile behaviour in the literature. Thus, linear material response is not adequate to design of adhesive material model for the brittle adhesives in the transition range. Therefore, third order polynomial form of stress-strain relation would be introduced here in order to describe nonlinear brittle response precisely. The approximation can be written depending on a third variable fracture elongation.

$$\sigma_a = E_a \varepsilon_a - \frac{E_a \varepsilon_f - \sigma_u}{\varepsilon_f^3} \varepsilon_a^3 \quad (4.18)$$

Where ε_f is the elongation at break. In this equation, the value of ε_f should be as much as small for a better interpretation of adhesive material behaviour. However, these approximations should be further validated for the corresponded adhesives experimentally for each of epoxy adhesive. The stress strain diagrams for various parameters are presented in Fig. 4.6 that enable computation of toughness value (U) of bulk adhesive samples, analytically.

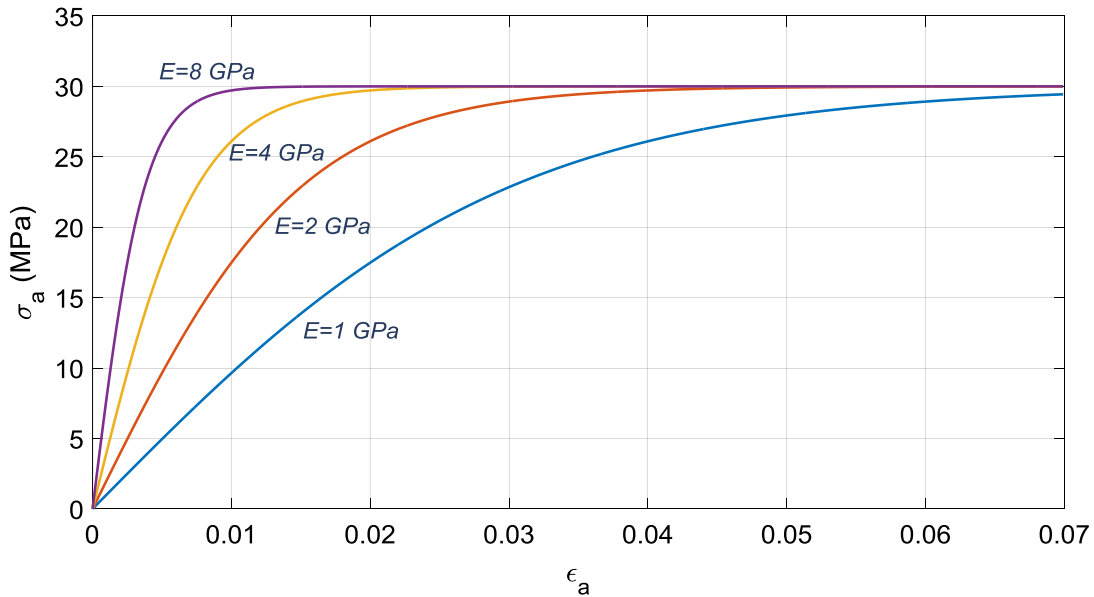


Fig. 4.6 Approximated stress-strain diagram of ductile epoxy adhesives using the Eq. 4.17 for various Young's modulus values and 30MPa tensile strength.

Most of the structural epoxy adhesives have the tensile strength and Young's modulus in the range of 20 to 50MPa and 1 to 8GPa, respectively. Therefore, these intervals are considered once the constructing stress-strain diagrams of bulk epoxy adhesives.

4.4 Implementation of FE Analysis

To calculate relevant stress distributions and failure loads, metal-to-metal adhesive joint specimens with different adhesive lengths and material properties were analyzed using the finite element (FE) method. ABAQUS[®] version 6.13 software and 2-D structural plane strain elements were used for this process. The adhesive joint in 2-D geometry was modeled as a plain strain problem, since it was very thin relative to the width of the entire joint. It was considered that the adhesive and the adherends remained both in linear elastic and non-linear plastic conditions during the analysis. This approach is coherent with the reality to the design of structural adhesive joints which are loaded beyond the elastic range.

4.4.1 Numerical Model

The numerical model was constructed as a 2-D plane strain problem since there is a linear proportionality between the joint strength and width of the joint. The steel adherends were modelled with a 4-node bilinear plane strain quadrilateral (CPE4) elements having a linear shape function and an integration point at each face. CPE4 element is also available in ABAQUS version 6.13, and compatible with non-linear material model and large displacement (non-linear geometry) option. In a similar way, the adhesive layer in the numerical model is replaced by a zero thickness cohesive layer. Thickness dependence cohesive parameters are employed to cohesive layer for precise representation of adhesive layer. The cohesive layer was constructed with a 4-node two-dimensional cohesive element (COH2D4) corresponding to bilinear traction-separation behavior. Both of the CPE4 and COH2D4 elements have three degrees of freedom at each node (translation in x, y and rotation about z axis). The element sizes of each layer is going to be presented more precisely in the mesh optimization section.

The numerical model of a single lap joint geometry is shown in Fig. 4.7 with detailed views at the free ends of overlap length. In the numerical model, the adhesive layer is represented by a zero thickness cohesive layer as shown by the red line in Fig.4.7. Similar metallic adherends are joined together by the cohesive zone, each having the refined mesh density at the joint extremities. The width of the joint is considered to be 1mm for each numerical model, since the strength of the entire joint varies linearly with respect to width of the adherends. In order to avoid mesh mismatches at the interfaces, the mesh size of the refined regions are taken to be equal to cohesive element length. Accordingly, number of elements through the cohesive zone thickness is equal to 1 as it is

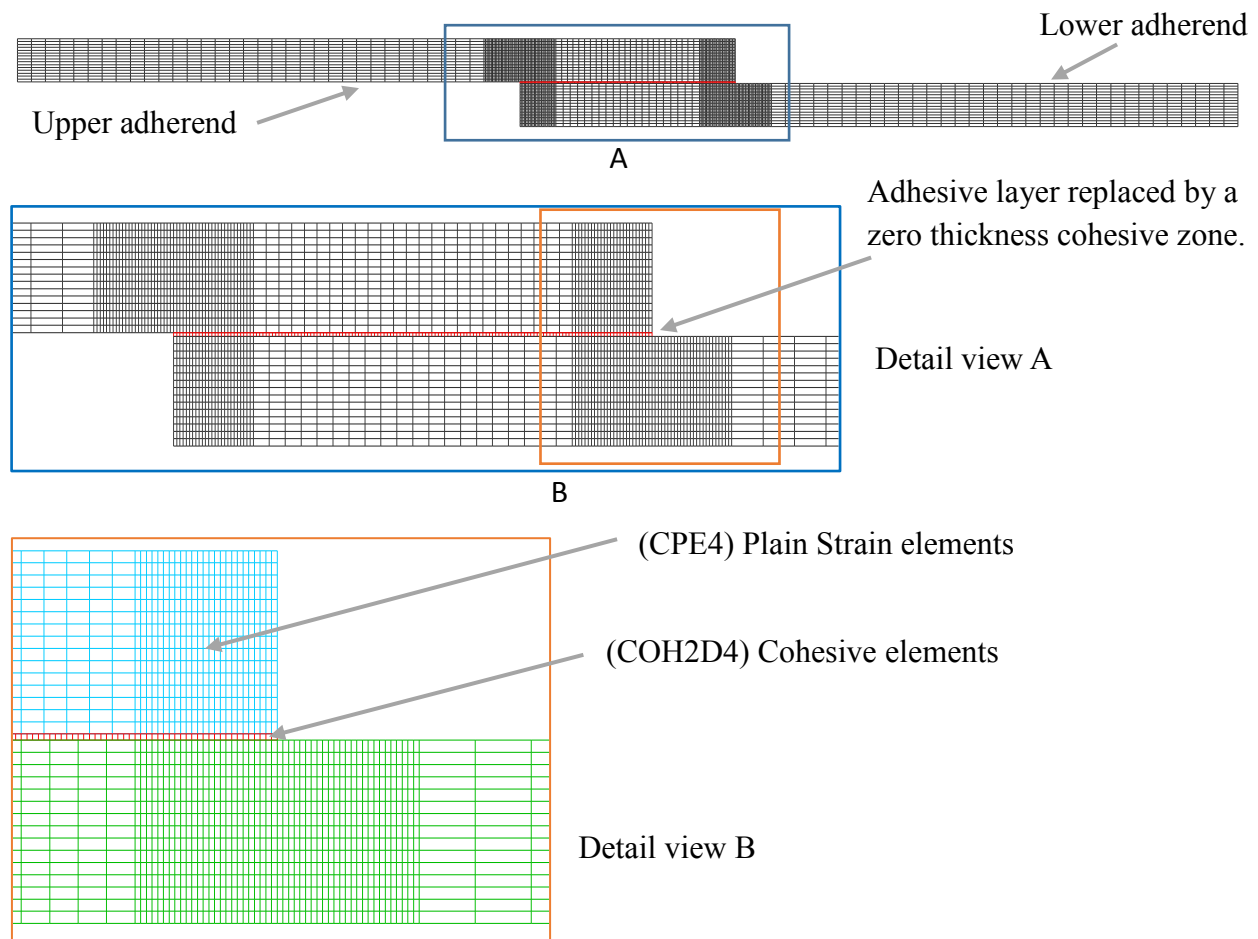


Fig. 4.7 Schematic illustration of mesh structure of single lap joint geometry constructed with two-dimensional plane strain elements.

stated in many literature sources.

4.4.2 Boundary Conditions and Loading

The applied boundary conditions for the numerical model is shown in Fig. 4.8. In order to simulate experimental conditions, vertical displacement of the grip lengths is constrained. End of the upper adherend is not free to move in x, y direction and rotate about z axis ($U_x=U_y=R_z=0$). Thus, there would be a symmetrical elongation of both adherends about the middle of the entire joint.

In this model, displacement control is employed instead of force control to eliminate convergence difficulties in the plastic regions. Therefore, a displacement is applied on the free end of bottom

adherend with an increment size of 0.01mm for each load step. Up to the failure instant, the reaction forces at the fixed edge are recorded during the numerical solution.

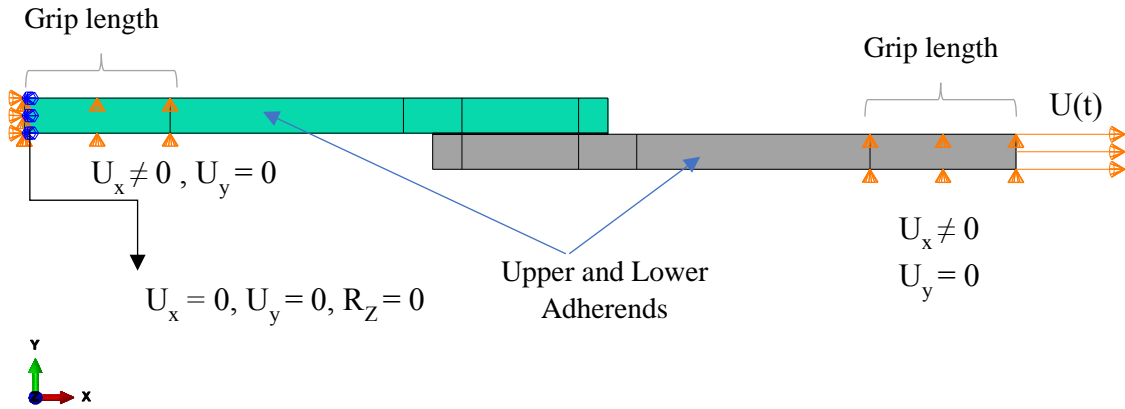


Fig. 4.8 Boundary conditions and loading of the numerical model.

For all coupon models stepwise loading is introduced by applying axial displacement increments on the nodes at the right end of the coupons. To avoid the dependence of load step convergence to mesh density, every time an element failure is detected the load is not increased for the following solution steps, until element failure stops propagating to adjacent elements and then the next increment is applied. After a thorough load step convergence study, including a range of displacement increments of 0.1 mm to 0.001 mm, it was found out that for a step equal to 0.01 mm, all models have fully converged.

4.4.3 Mesh Optimization

In order to reduce computational effort, generalized plane strain analysis was chosen since relatively small strains are expected in the width direction of the model. Geometric nonlinearity was also included in the analysis by taking into account large strain effects. Traditional finite elements have difficulties in resolving the stress state at bi-material wedges due to the existence of singularities and their results vary with mesh refinement. In this study, this case is addressed by a correlation of mesh density with the failure load. For example, five different quadratic element edge sizes (from 0.5mm to 0.05mm) are used as a function of load factor for the CPE4 plane strain elements, which is used for the adherend material. It is found that 0.1mm of element edge size (corresponding to 0.1 percent variation in load factor) is decided to be sufficient to obtain accurate

failure loads. Therefore, refined mesh regions modelled with the element size of 0.1mm whereas the coarse regions are 0.2mm.

However, the choice of a suitable mesh size in the cohesive zone is the critical issue. It is necessary to have a sufficient number of elements in the cohesive zone to give a good representation of the distribution of tractions. The minimum number of elements needed in the damaged part of the cohesive zone, the process zone, is not well established. This issue is discussed in depth in Turon et al. [44]. The length of the process zone (i.e. distance from the crack tip to the point of maximum traction) is given by [44]

$$L_{czm} = \frac{9\pi}{32} E \frac{\Gamma_n}{(\sigma_n^c)^2} \quad (4.19)$$

Where, E is the Young's modulus of the adhesive, Γ_n is the specific fracture energy and σ_n^c is the maximum traction in normal direction. If the specific fracture energy and critical traction are known, then a suitable element size can be chosen for the cohesive zone element. In this study, the minimum cohesive zone element for the three parameters that approaches Eq. 4.19 to a minimum value is 0.12 mm, corresponding to extreme values (e.g. E=1GPa, $\Gamma_n=0.5$ N/mm and $\sigma_n^c=60$ MPa). In other words, any cohesive zone element size which is less than the critical length of 0.12mm would be feasible for the progressive failure model of adhesive layer. Thus, the element size in the cohesive zone is considered to be 0.06mm, enabling to place two elements in the damaged region.

4.4.4 Numerical Solution Algorithm

In fact, there are three groups of parameters affecting the failure load of the single lap joints; which are material properties of adherend (E, σ_y , n), geometry parameters (L, t, η) and cohesive zone parameters of the adhesive (Γ , K_0 , σ_c). The joint is loaded in the uni-axial direction with the increasing displacement. When an element at the cohesive zone reaches the critical separation strength value σ_c either in shear or normal direction, the damage initiates according to Eq. 4.2. Then stiffness degradation occurs based on a dimensionless damage variable D as described in Eq.4.20 as a function of separation displacements using linear softening model.

$$D^{(k)} = \frac{\delta_f(\delta^{(k)} - \delta_c)}{\delta^{(k)}(\delta_f - \delta_c)} \quad (4.20)$$

Where $D^{(k)}$ is the damage variable at k th step and $\delta^{(k)}$ is separation displacement at k th step, δ_c and δ_f are the critical displacement at damage initiation and separation displacement at the complete failure, respectively. The stiffnesses of the cohesive zone model as a function of this damage variable at k^{th} step are calculated in Eq. 4.21.

$$E^{(k)} = (1 - D^{(k-1)})E \quad (4.21a)$$

$$G^{(k)} = E^{(k)}/2(1 + \nu) \quad (4.21b)$$

During the softening process the values of E and G are incrementally decreased based on the Eq. 4.20 up to the final failure. The damage evaluation of an element in the cohesive zone is assessed regarding to energy criterion introduced in Eq. 4.3. When the energy criterion (Eq. 4.3) is satisfied then corresponded element completely fails and removed from the cohesive layer. The basic numerical algorithm of progressive failure model is presented in Fig.4.9.

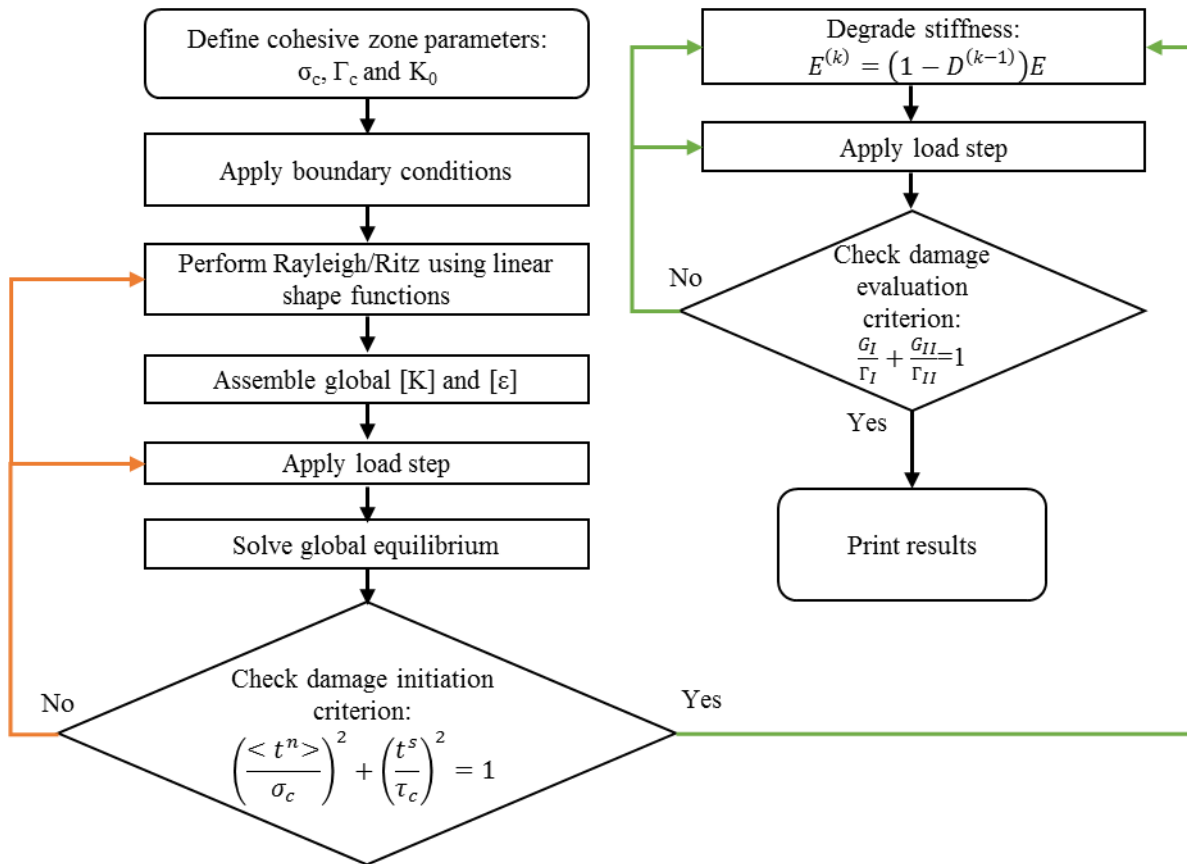


Fig. 4.9 A simple flowchart representing the progressive failure model of the cohesive layer for FE analysis.

5

Material and Experimental Procedure

5.1 Determination of Material Parameters

To determine the material properties of both adherend and adhesive, some series of consecutive test procedures were applied. The material parameters of the adherend (e.g. yield stress and strain hardening exponent) were determined implementing a uniaxial tensile test. In the same way, tensile test of bulk adhesive to evaluate ultimate tensile strength and toughness was conducted. Additionally, some other tests for evaluating normal and shear mode fracture toughness were realized in order to validate numerical model proposed in the previous chapter. Extensive concepts and procedures of each test are expressed in the followings sections.

5.1.1 Uniaxial tensile test of bulk samples

Structural steels are used in many ways and their application can be diverse. They are particularly useful because they offer the unique combination of good weldability with guaranteed strengths. Structural Steel is an extremely adaptable product and is often favored by the engineer trying to maximize strength or structure while minimizing its weight. Structural mild steels having a carbon content in the range of 0.1-0.2% are the point of interest in this thesis. There are many examples of European grades of structural steel such as; S195, S235, S275, S355, S420, S460 etc. However, for the purposes of this article we will focus on the mechanical properties and applications of S235, S275 and S355. Therefore, the adherend material for validation purposes was preferred to be S235-JRG1 steel having the minimum yield stress of 235MPa with high elongation

up to 30%. The chemical composition of structural steel is extremely important and highly regulated. It is a fundamental factor which defines the mechanical properties of the steel material. The chemical composition of this metallic adherend material, as indicated in literature studies are shown in Table 5.1 [45, 46]. A tensile test specimen was manufactured from a sheet metal having 1mm in thickness according to tensile test standard of metallic materials (EN 10002-1). The geometry of the specimen is also given in Fig 5.1. Hence, true and engineering stress-strain curves of the specimen are presented in Fig. 5.2 to understand the material parameters such as yield stress and strain hardening exponent; which is required to construct material model for the numerical analysis.

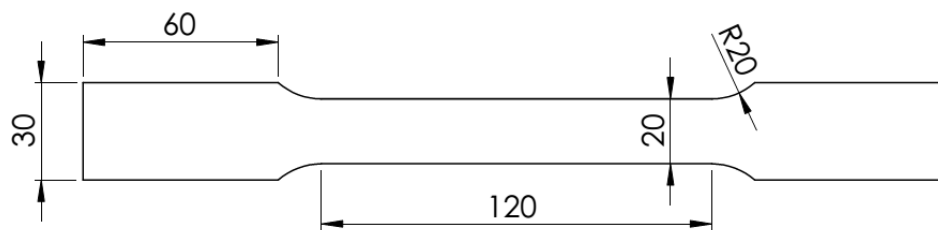


Fig. 5.1 The tensile test geometry of metallic specimen.

Table 5.1 Mechanical properties (tensile test) and chemical composition of S235JRG1 steel adherend

Mechanical property		Chemical composition (wt. %)			
Ultimate strength (MPa)	325	Carbon, C	0.17	Copper, Cu	max 0.40
Yield strength (MPa)	285	Chromium, Cr	max 0.15	Phosphorus, P	max 0.0045
Young's Modulus (GPa)	200	Manganese, Mn	max 1.4	Sulphur, S	max 0.045
Elongation at break (%)	25	Silicon, Si	*nan	Nitrogen, N	max 0.007

* Not available

The mechanical properties of structural steel are fundamental to its classification and hence, application. Even though chemical composition is a dominant factor of the mechanical properties of steel, it is also very important to understand the minimum standards for the mechanical properties (performance characteristics) such as yield strength and tensile strength. Thus the strain hardening exponent for both true and engineering stress-strain curves are evaluated 0.19 and 0.09, respectively. Strain hardening exponent can be basically expressed as the slope of the logarithmic stress-strain relation in the plastic region. For the validation purposes of the numerical model, $n=0.19$ representing the true stress-strain relation should be introduced to FE model.

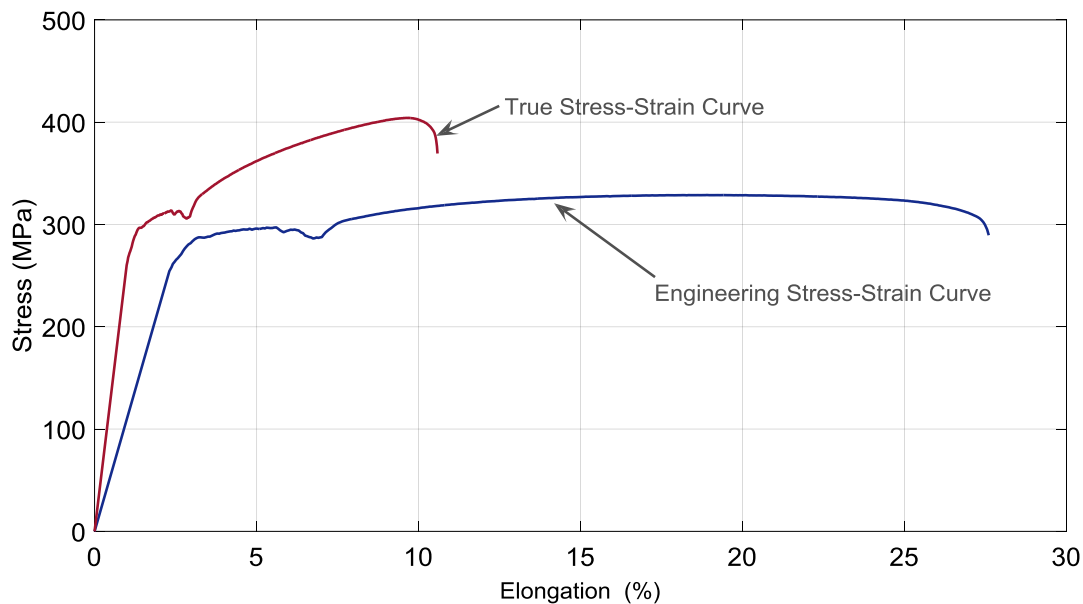


Fig. 5.2 True and engineering tensile test results of S235-JRG1 structural steel adherend.

The uni-axial tensile test of metallic adherend (S235-JRG1) was repeated three times in a tensile test device, namely ZD 10/90 at a crosshead speed of 5mm/min. Then the average load and crosshead displacement values were considered to construct stress strain curves.

One type of adhesive was selected: Veropal (He 20-06) from (SYNPO, Czech Republic). The adherends were joined using a unique hybrid two-component (Component A: Resin, Component B: Hardener) epoxy structural adhesive with high elongation and at the same time with excellent peel strength and shear strength. It is used for structural bonding of a wide range of substrates. The chemical basis of the hardener is an arbitrary rubber (ATBN) modified complex mixture of amines. The adhesive components were mixed as 1:1 by parts weight. The viscosity of adhesive after mixing is 15-22 Poise at 23 °C. As recommended by SYNPO, the bonded samples were cured in the ambient condition at 20-23 °C and 70% humidity for 24 hours. The geometry of the bulk adhesive samples is given in Fig. 5.3. Besides, this bulk adhesive was tested according to standard EN-ISO 527-2 [47]. The bulk adhesive specimens were tested in a tensile testing machine as shown Fig. 5.4, (Instron-5940) after 48 hours of curing time, at a constant crosshead speed of 5mm/min, at the ambient conditions. For each sample, the mechanical extensometer was placed at the ends of gauge length (80mm for each sample).

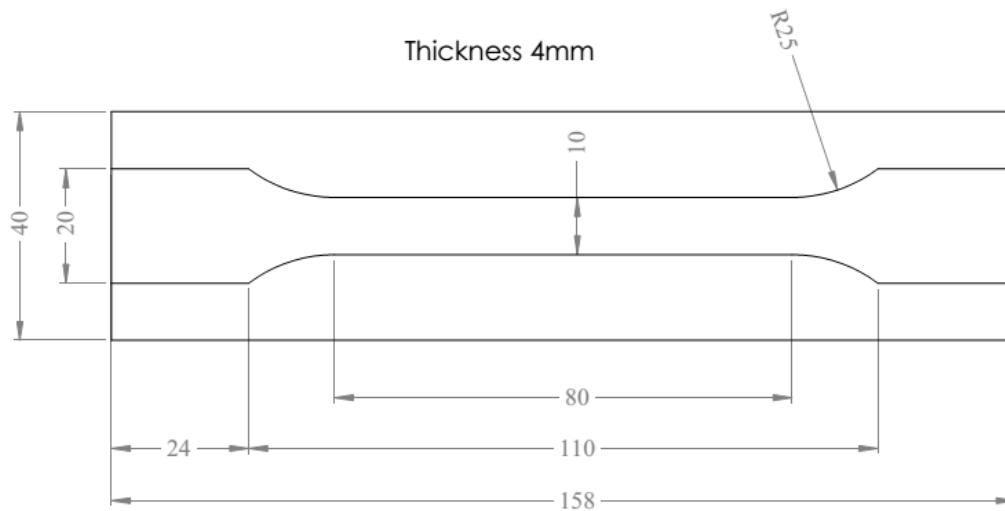


Fig. 5.3 The mould design representing the dimensions of the bulk adhesive specimen according to EN-ISO 527-2.

The results of the mechanical test for the bulk adhesive are; Young's modulus 967 MPa, Poisson's ratio 0.34, tensile strength 28.6 MPa, and elongation at break 7.6%. Moreover, the experimental and analytical the stress–strain relations of the bulk Veropal HE-20 adhesive is expressed in Fig. 5.5, attaining a quite accurate fitted curve with a regression coefficient of $R^2= 0.99$. Therefore, it is quite simple to find out the Young's modulus and ultimate tensile strength of the bulk adhesive from the analytical expression in Fig. 5.5 which is also stated in chapter 4.

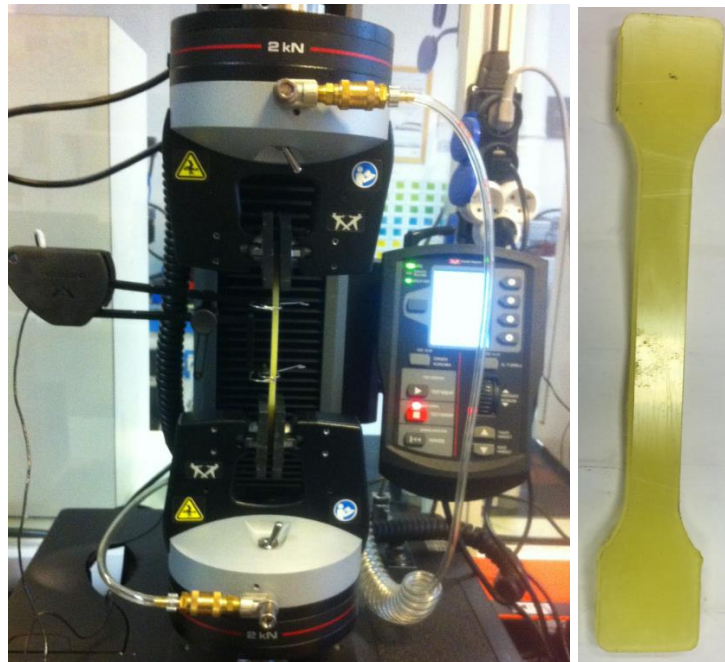


Fig 5.4 Uni-axial tensile testing system with mechanical extensometer for the bulk adhesive samples.

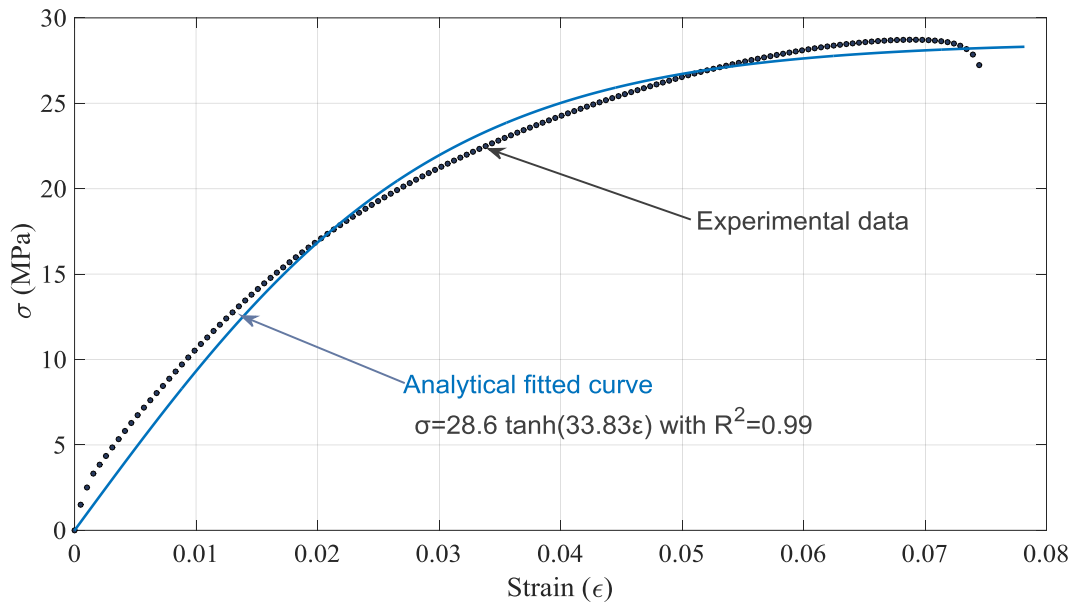


Fig. 5.5 Experimental and analytical stress-strain curves of bulk Veropal HE-20 adhesive.

The other adhesive used for the validation process is two component structural epoxy adhesive namely, Carboresin supplied from SYNPO company in Czech Republic. It consists of two components; resin (A) and hardener (B) mixed in a ratio of A:B=1:3 by weight. Carboresin is quite brittle adhesive with relatively low ultimate tensile strength.

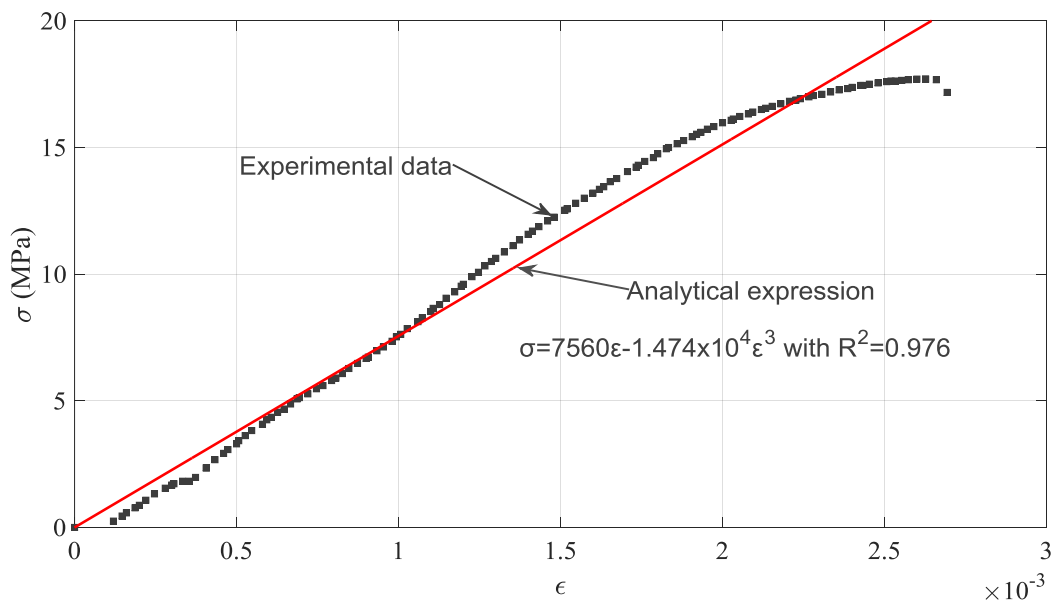


Fig. 5.6 Experimental and analytical stress-strain curves of bulk Carboresin brittle adhesive.

The main mechanical properties are the Young's modulus 7560 MPa, ultimate tensile strength 17.7 MPa and elongation at fracture nearly 0.3 %. The detail description of experimental and analytical stress-strain relations are depicted in Fig. 5.6. The analytical expression to characterize stress strain relation approximates the real data with a regression coefficient of $R^2=0.976$. It is found out to be lower than the analytical expression for ductile adhesives (see Fig. 5.5) but still in the range of acceptable limits. Hence, the toughness values of both Veropal HE-20 and Carboresin would be evaluated taking the integrations of the analytical expressions for the bundles zero to fracture strain. The bulk adhesive Carboresin was cured 24 hours at the ambient conditions as it is recommended by the manufacturer. The glass transition temperature is declared to be 55 °C for the curing process of one day.

5.1.2 Double cantilever beam (DCB) test

ASTM recommends D5528 standard for mode I interlaminar specific fracture energy. Although this test method is meant for interlaminar specific fracture energy of unidirectional composite laminates, it can also be used for adhesive-bonded joints [48]. Specimen configuration is similar to what the standard suggests. The double cantilever beam (DCB) with piano hinges, as shown in Figure 5.7, consists of two adherends bonded with adhesive.

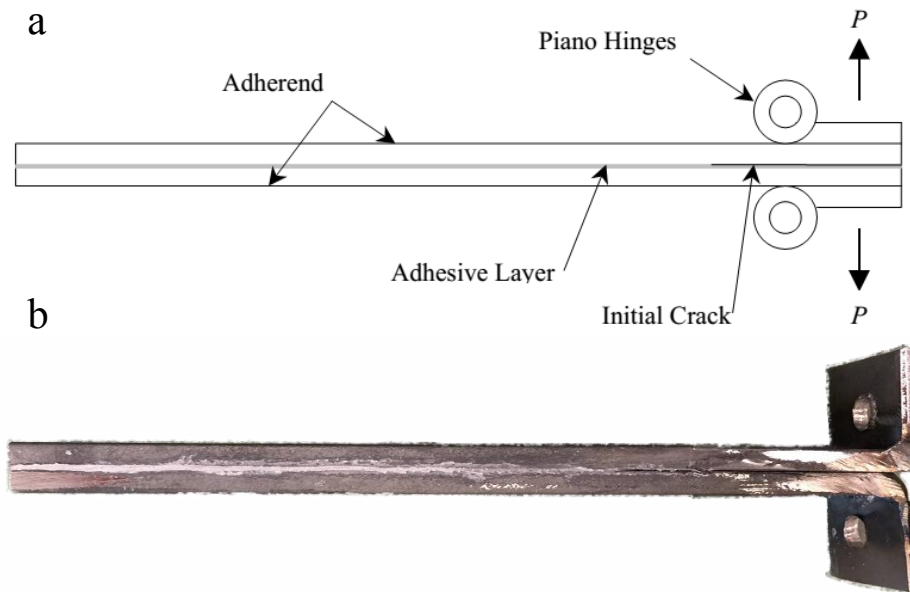


Fig. 5.7 Schematic diagram of a) Mode I DCB specimen and b) manufactured Mode I DCB specimen (side view)

The mode I specific fracture energy, Γ_{Ic} , was determined using the modified beam theory (MBT), which accounts for rotation at the delamination front, as recommended in ASTM D5528 standard. The final data reduction formula is shown in Eq. 5.1. An initial crack length of 35mm is considered.

$$\Gamma_{Ic} = \frac{3F_c\delta_c}{2b(a + |\Delta|)} \quad (5.1)$$

Where F_c is critical (maximum) load, δ_c is critical displacement corresponding to maximum load, b is specimen width, a is the initial crack length and Δ is the correction factor for rotation of adherend. The correction factor would be neglected since the adherend is sufficiently rigid with a relatively high thickness of 5mm. The specimen geometric parameters for mode I DCB test are taken as $a=35\text{mm}$ and $b=30\text{mm}$. The experimental force versus crack opening displacement diagrams of both ductile adhesive (Veropal HE-20) and brittle adhesive (Carboresin) are given in Fig. 5.8. The critical parameters are recorded to be 394N at 2.99mm and 295N at 2.06mm for Veropal HE-20 and Carboresin adhesives, respectively as indicated in Fig. 5.8. Substituting these critical parameters in above Eq. 5.1, the mode I specific fracture energy (G_{Ic}) can be calculated as 1.68 N/mm and 0.86 N/mm for ductile (Veropal HE-20) and brittle (Carboresin) adhesives, respectively.

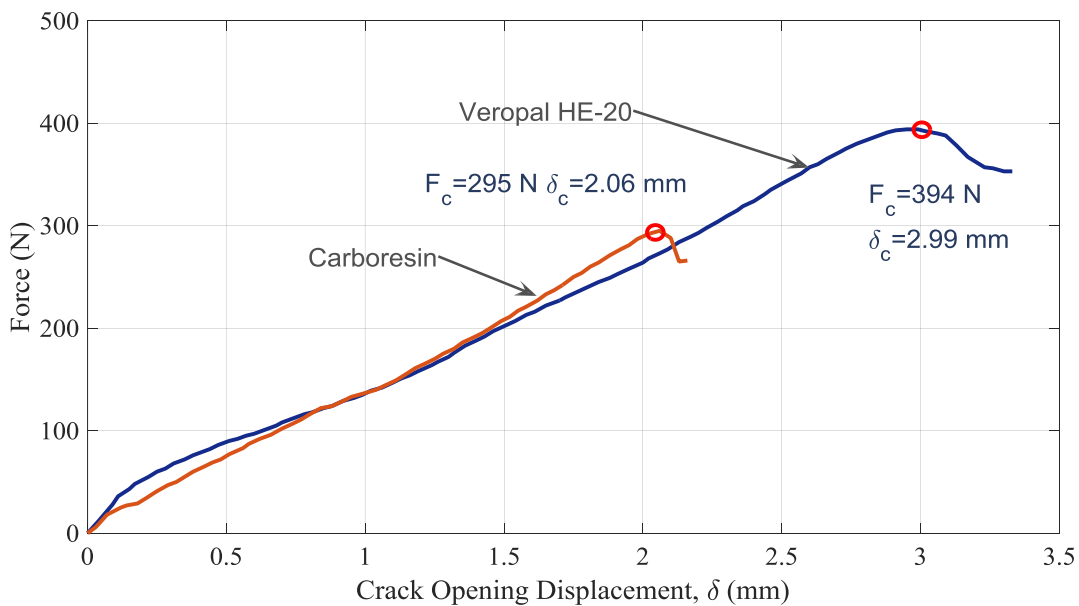


Fig. 5.8 Force versus crack opening displacement diagrams of mode I DCB test for the ductile and brittle adhesives.

5.1.3 End-notched flexure (ENF) test

In order to determine critical pure shear (Mode II) specific fracture energy of the bulk adhesives, SACMA recommends a three-point bend test using an edge notch flexure (ENF) specimen [49]. This standard can also be used effectively for bonded joints. The schematic illustration of the end notched flexure (ENF) test specimen geometry is given in Fig. 5.9.

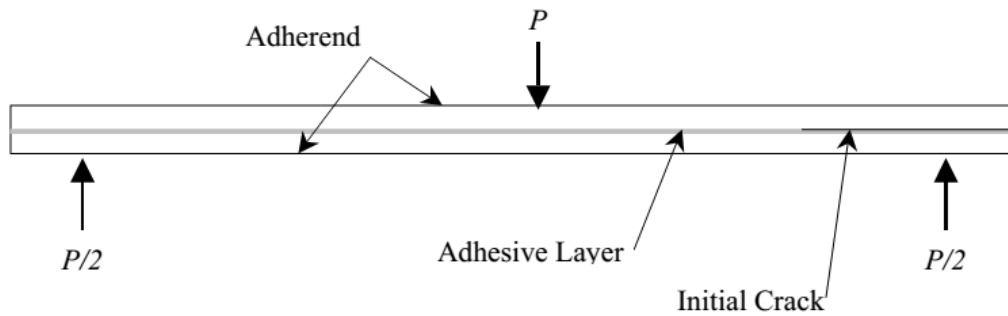


Fig. 5.9 End notched flexure (ENF) specimen geometry for Mode II interlaminar fracture test.

The test specimen was manufactured bonding two separate metallic parts together by applying adhesive on the interface surfaces. But the initial crack length is completely free of adhesive. Tests were conducted using the End-notched Flexure specimen. The ENF test involves loading a beam with a mid-plane starter crack at one end, in three-point bending, as shown in Fig. 5.10. Crack length, a , is measured from the support roller, and the half-span length, L , is the distance from the support rollers to the center loading roller.

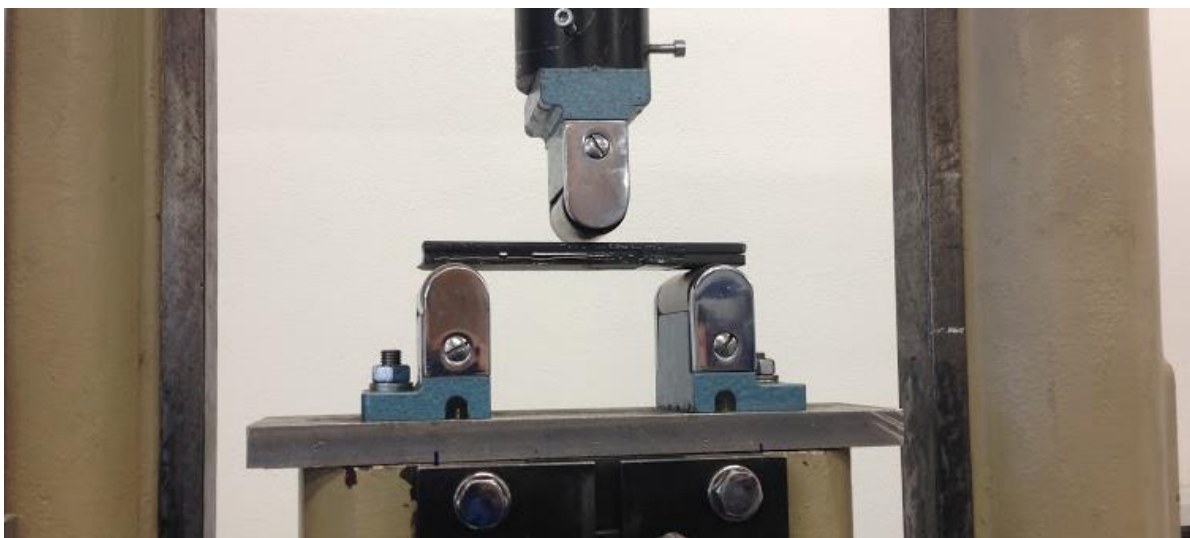


Fig. 5.10 Experimental setup for three point bending testing of the ENF specimen.

As recommended by ASTM D5528-01, the mode II specific fracture energy, Γ_{IIc} , is determined using the formula shown in Eq. 5.2.

$$\Gamma_{IIc} = \frac{9a^2 F_c \delta_c}{2b(2L^3 + 3a^3)} \quad (5.2)$$

The geometry parameters are; the initial crack length $a=35\text{mm}$, half span length $L=60\text{mm}$ and width of base material $b=30\text{mm}$ for the evaluation of mode II specific fracture energy. The critical load F_c and correspondent critical displacement δ_c were specified constructing a load-displacement diagram for both of the adhesives (see Fig. 5.11). The critical values are calculated as 6500N at 1.58mm and 4687N at 0.92mm for Veropal HE-20 and Carboresin adhesives, respectively. Thus critical mode II interlaminar specific fracture energy can be evaluated substituting these value in Eq. 5.2. The specific fracture energy (Γ_{IIc}) is calculated 3.37 N/mm and 1.42 N/mm for Veropal HE-20 and Carboresin, respectively.

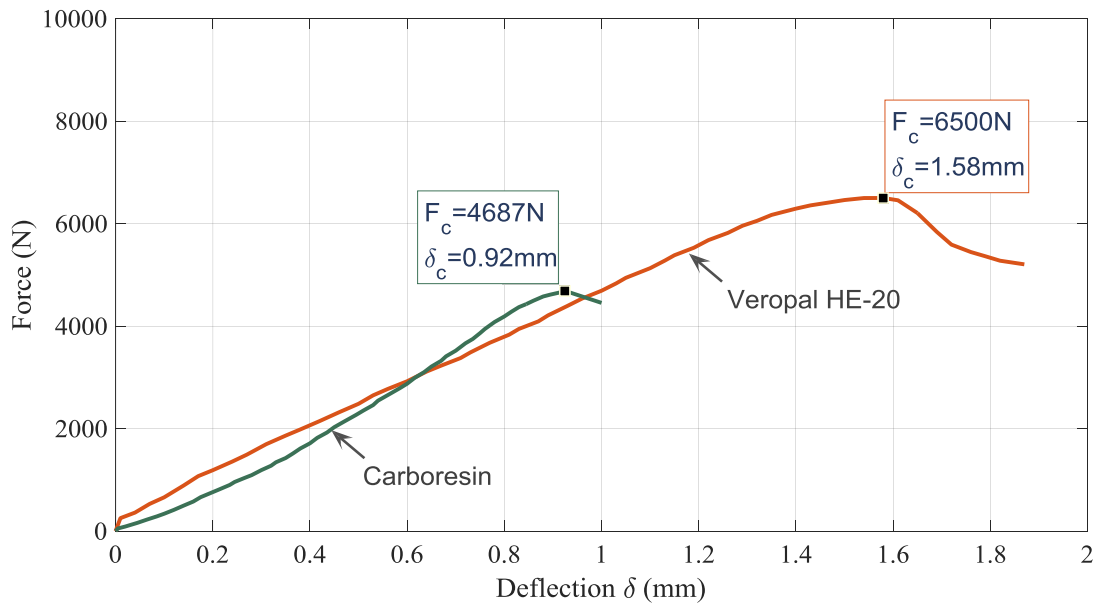


Fig. 5.11 Load versus vertical deflection diagrams of Mode II ENF test specimens

5.2 Manufacture of Single Lap Joints

For the manufacture of the single lap joints, degreasing of the adherend surfaces is the minimum pretreatment that is usually carried out prior to bonding. Grit-blasting or other mechanical abrasion methods are also recognized as providing a useful increase in initial adhesion level. Mechanical treatment allows the development of actual geometrical structure of adhesively bonded materials, which results in an increased contact area between the molecules of an adhesive and substrate, causing higher intermolecular interactions and, thus, increasing adhesive properties [50]. Accordingly, roughness is a parameter that affects the strength of bonded joint, because it leads to an increased contact area between two adherends and increases the adhesion by mechanical interlocking. Grinding is the most widely used mechanical abrasion method characterized by the fact that abrasion is done by tools with unspecified geometry and number, in which grinding grits do not change their position relative to one another owing to the use of a binder [50]. In this study, the surface of all adherends being bonded were grinded with a 200mesh silicon carbide grinding papers perpendicular the direction of the loading. The single lap joints having a width of 25 mm, were manufactured and tested according to ASTM D1002 standard [51] shown in Fig. 5.12. The alignment taps were placed at the grip lengths of testing fixtures to avoid misalignment during the axial loading.

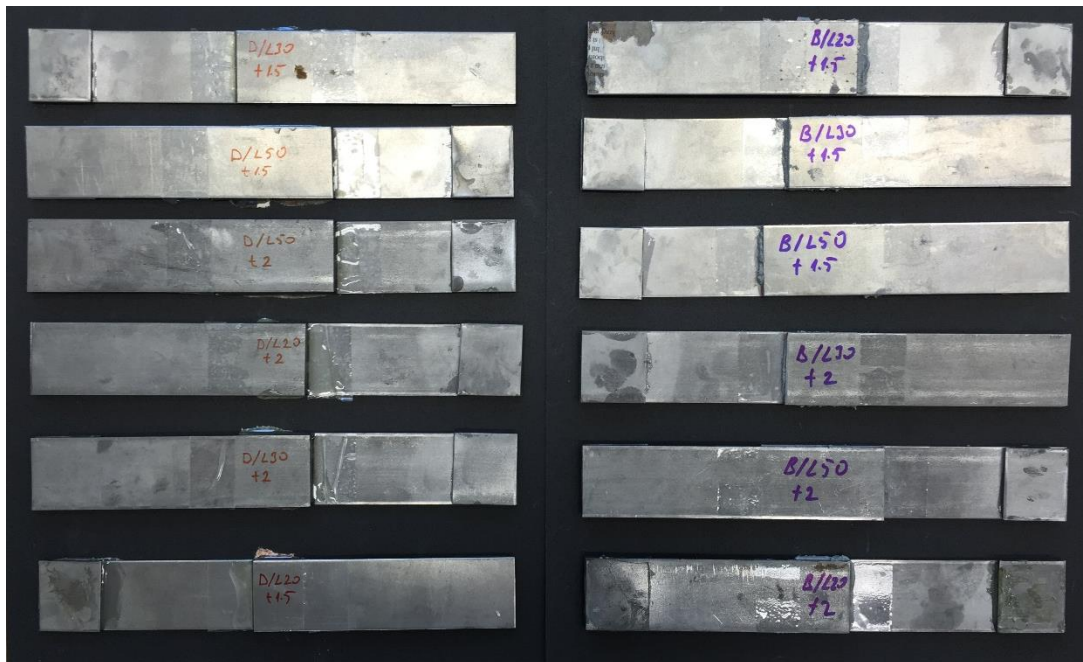


Fig. 5.12 The manufactured single lap joint coupons according to ASTM D1002 standard.

For surface preparation, the adherend surfaces were pre-treated by acid solution. The etching process was performed with a solution of sulfuric acid (20ml at 30% wt.), and the de-ionized water (40ml) at the ambient conditions. The etching solution was maintained at about 25 °C and the steel adherends were allowed to stay in that for about 10 min. until no visible air bubble appears in the solution. Then the test specimens were taken out and were sprayed in tap water for another 3 min. Finally the test specimens were dried thoroughly at about 50 °C. The adherents were bonded with the adhesive within 3 hours after the surface preparation and then the joints cured at room temperature for about 24 h. Two specimens for each configuration were fabricated and tested in a tensile test machine (ZD 10/90) under displacement control with a crosshead speed of 5 mm/min. During the tests, the load was increased up to complete debonding of the joints. The maximum load which resulted in complete debonding was recorded in each test as the static failure load or load carrying capacity of the joint. The configuration of fabricated specimens for the purpose of numerical model validation are presented in Table 5.2. Each joints series in Table 5.2 corresponds two different adherend thickness of 1.5 and 2 mm, which means that each joint series represents two specimens at two different adherend thickness. Totally, 24 specimens were manufactured for 12 different configurations considering two repetitions for each test.

Table 5.2 Dimension of the joint series in (mm) for Veropal HE-20 (V series) and Carboresin (C series).

Joint Series	Bonding Length, L	Adherend thickness, t	Joint width, w
V-20	20	1.5 and 2	25
V-30	30	1.5 and 2	25
V-50	50	1.5 and 2	25
C-20	20	1.5 and 2	25
C-30	30	1.5 and 2	25
C-50	50	1.5 and 2	25

Bonding procedure was performed as follows. The adhesive was mixed according to composition as it is stated previously. In the case of two-component adhesives, the mixture of the resin and hardener introduce voids, to reduce even further the quantity of voids, a toothpick was used to burst the air bubbles out before the application of pressure. The adhesive thickness was controlled using preloading gauge block (20 N) after applying the adhesive on the sides bonding area with a spatula. The samples were aligned according to markings and held in place by the force until the completion

of the curing processes for 24 hours. Cotton buds were used to wipe off any extra adhesive from the sides of the overlap, to avoid fillet-like formation of adhesive. The samples were kept in ambient conditions at 20-23 °C and in 70% humidity. After the curing process completion, the thickness of adhesive layers were measured using a micrometre. A nominal value of adhesive thickness with the upper and lower tolerances was calculated 0.15 ± 0.036 mm for V joint series, and 0.55 ± 0.032 mm for the C joint series, respectively.

5.3 Testing Strength of Adhesive Joints

In the mechanical tests the single lap joints are loaded to the point of fracture. The nature of the fracture (adhesive fracture, cohesive fracture, substrate fracture or a combination of these) provides information about the quality of the bonding process and about any potential production errors. Regarding tests on samples equilibrated under controlled conditions, a cohesive fracture indicates that the adhesion remained stable despite the influences acting on the bond (e.g. moisture). In contrast, an adhesive fracture indicates that the bond has failed at its most sensitive point, the adhesion. This may indicate incompatibility between the substrate material and adhesive, inadequate surface pretreatment and/or processing/application errors. The bond strength of bonded single lap joints on subjecting the substrates to loads is determined by lap shear forces in the direction of the bonded joint. In accordance with the standard ASTM D1002, the overlap corresponds to a width of 25 mm and relevant overlap length of L. Each sample must be measured individually. To do this, a sample is clamped in the self-aligning jaws of the test unit so that the force acts in the center of the bonded layer, as illustrated in Fig. 5.13.

Shear joints impose uniform stresses across the bond area which results in the highest possible joint strength. ASTM D1002 is commonly performed to measure the shear strength of adhesives that are used to bond metals. This test is similar to ASTM D3163 which is for adhesives that bond rigid plastic substrates, and also ASTM D3164 which is for plastic adhesives that are used to bond both plastic and metal substrates. All three of these specifications use a single lap joint (lap shear) specimen to determine the shear strength of adhesives.

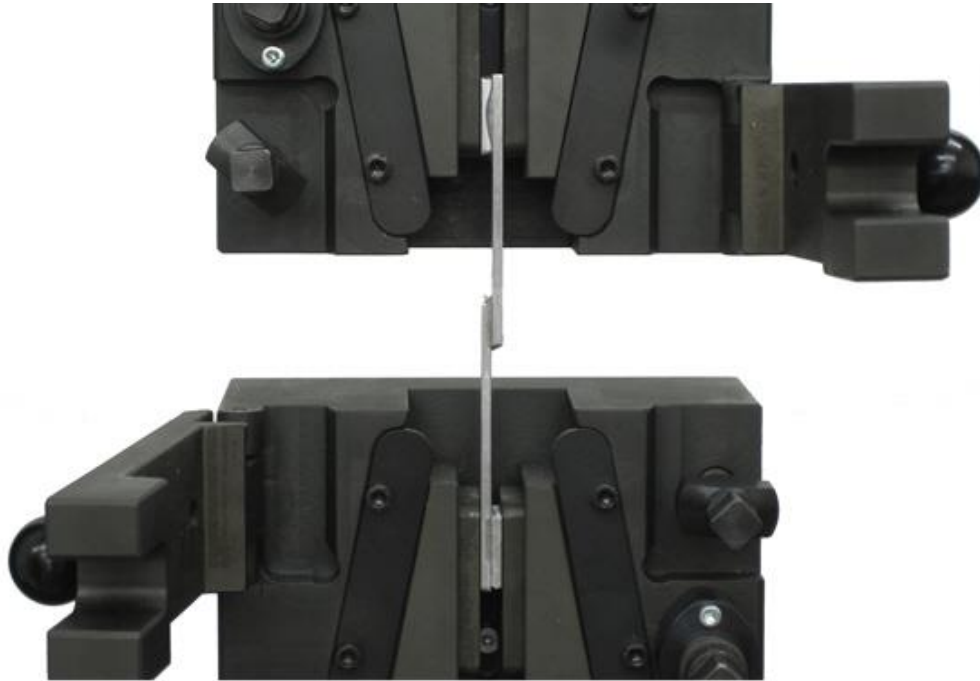


Fig. 5.13 Experimental setup for testing strength of the single lap joints

For the validation procedure the strength of the single lap joints were specified to be the force recorded at the fracture per unit width of the joint. Because, it makes quite easy to analyze results of comparison between experimental and numerical joint strength. For a normalized description of the joint material and geometry parameters a further methodology is going to be implemented in the next chapter.

5.3.1 Validation of numerical model

In order to make a verification of the proposed numerical model, the experimental and numerical results would be compared based on the same geometry parameters. Therefore, typical load-displacement diagrams of the manufactured specimens were constructed as a result of the tensile tests. The typical load-displacement diagram of the C (Carboresin) joint series at three overlap length 20, 30 and 50 mm, each having two different adherend thickness of 1.5 and 2 mm, is given in Fig. 5.14. Similarly, Fig. 5.15 illustrates the load-displacement curves of V (Veropal HE-20) joint series. It was clearly observed that as the load increases the global joint stiffness value also increases up to the failure point. It would be claimed that the elongation is more dependent to thickness of the steel adherend and nearly regardless of adhesive deformation response, since the adhesive has the relatively thin values.

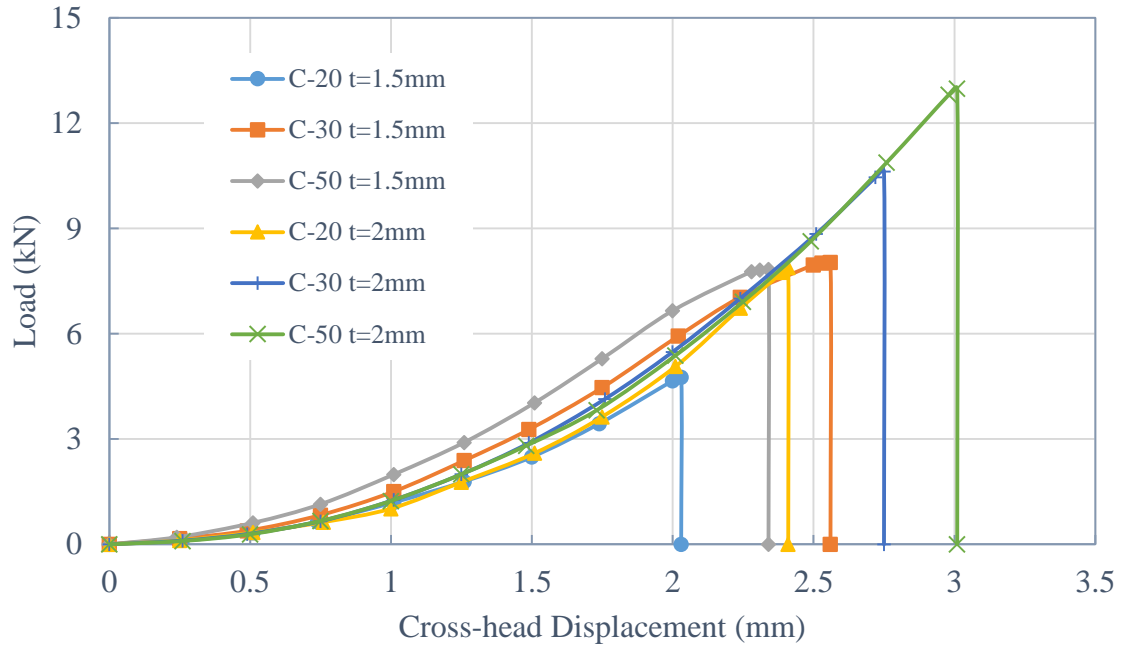


Fig. 5.14 Experimental load and cross-head displacement curves of the single lap joints bonded with Carboresin.

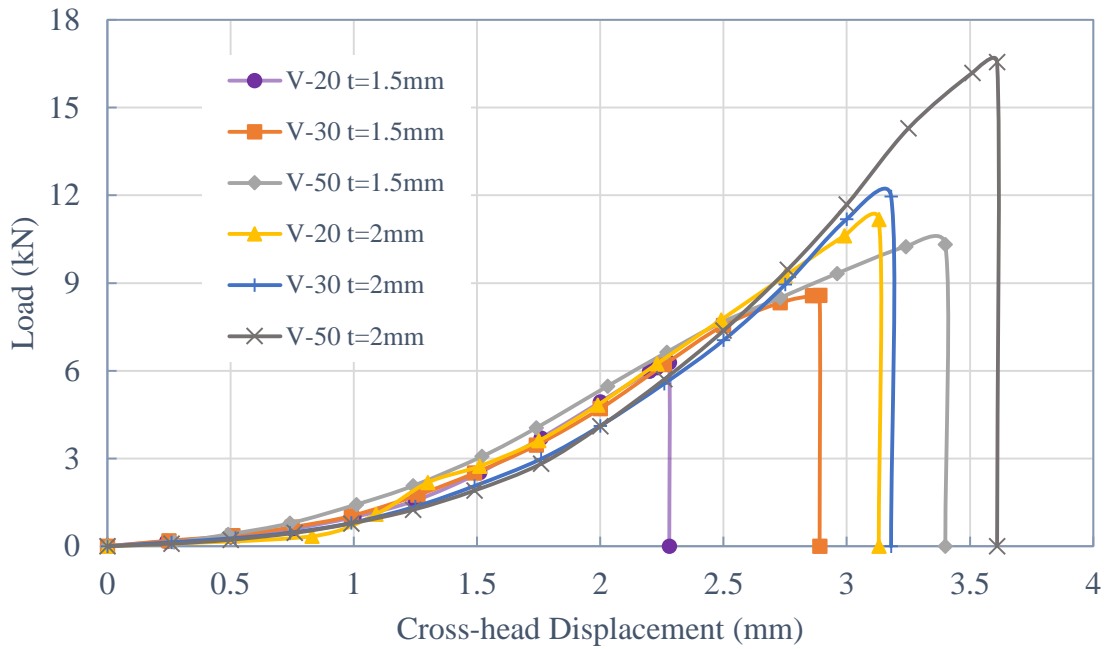


Fig. 5.15 Experimental load and cross-head displacement curves of the single lap joints bonded with Veropal HE-20.

Cohesive zone material properties of the bulk adhesives (introduced and evaluated in the previous section) are summarized in Table 5.3 based on the analytical calculations and experimental results in Chapter 4 and 5, respectively. These aforementioned properties are adopted to ABAQUS® in order to accomplish validation procedure of experimental failure loads. The experimental failure loads are considered to be the peak values for each curve in Fig. 5.14 and 5.15. Likewise the numerical load-displacement curves of each configuration are given in Fig. 5.16 and 5.17 corresponding to V and C joint configurations, respectively to simulate and validate experimental results.

Table 5.3 Cohesive zone material parameters of bulk adhesives for the numerical analysis.

	Veropal HE-20	Carboresin
Initial normal stiffness, K_n	6445 N/mm ³	13745 N/mm ³
Initial shear stiffness, K_s	2405 N/mm ³	5370 N/mm ³
Mode I fracture energy, Γ_I	1.68 N/mm	0.86 N/mm
Mode II fracture energy, Γ_{II}	3.37 N/mm	1.42 N/mm
Normal critical traction, σ_n	28.6 MPa	17.7 MPa
Shear critical traction, σ_s	16.5 MPa	10.2 MPa
Poisson's ratio, ν	0.34	0.28

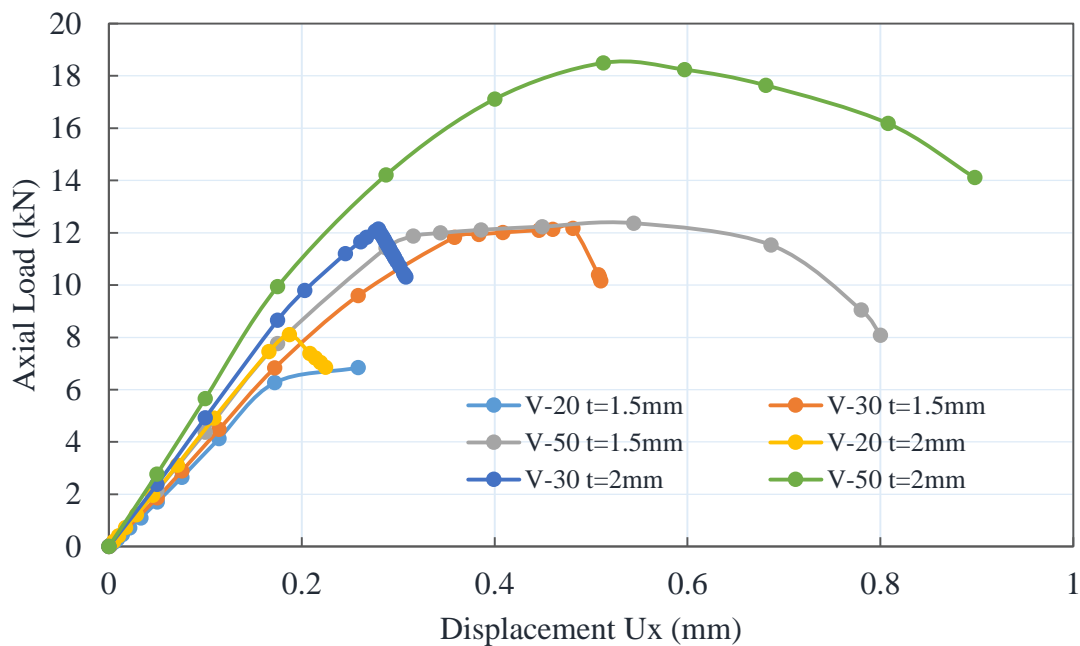


Fig 5.16 Numerical axial loads of the V series joint configurations against axial displacement.

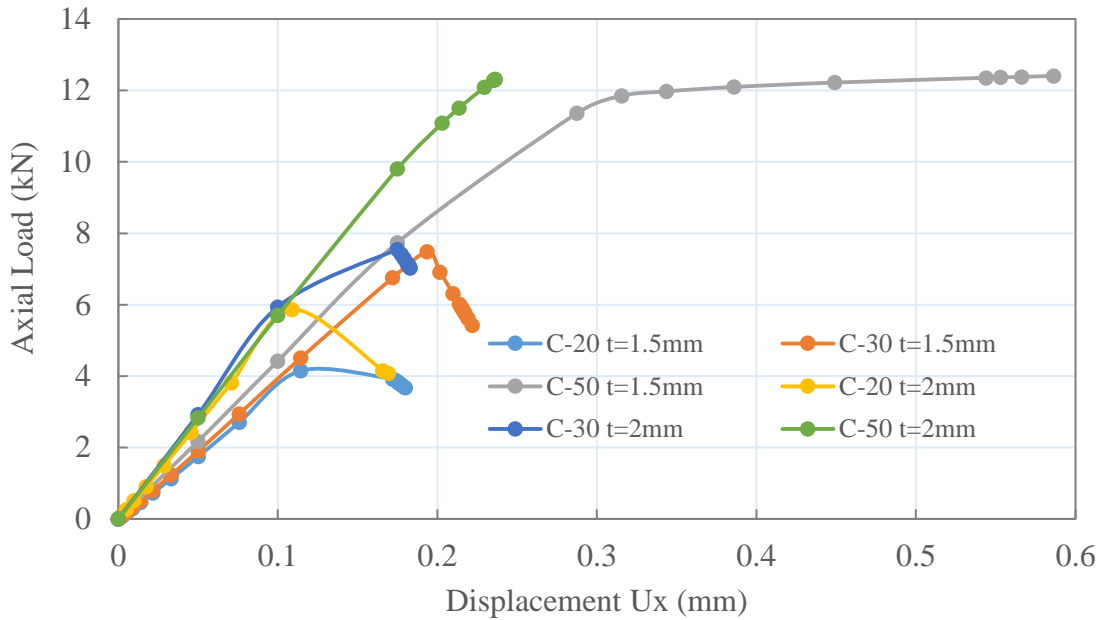


Fig 5.17 Numerical axial loads of the C series joint configurations against axial displacement.

This FE analysis showed how a single lap joint could be simulated to capture the behavior of an entire joint, by using a cohesive zone progressive damage approach to solve for the appropriate shape functions rather than classical damage mechanics theories having convergence difficulties. The cohesive zone element is intended for use as a design tool that can model a joint to estimate failure mechanism and still couple with global vehicle scale finite element models. Some of the limitations of this model are contained in the assumptions used to generate thickness dependence cohesive zone parameters. First, the adhesive is modeled as a zero thickness bed of springs in normal and shear directions rather than a continuum, and so eccentricity due to adhesive thickness of the adhesive is not represented in the element. Additionally, the adherends are assumed to behave like wide plates under plain strain conditions. Thus, variations in fields through the width of the joint are not captured but not necessary to evaluate joint strength. Progressive failure of the adhesive was approximated, by shortening the joint element by the length of the failed adhesive and lengthening the adjoining plain strain elements. Softening of the adhesive as the stress increases causes the shape functions to no longer be exact. The predicted behavior of load-displacement curve for a single lap joint did not match precisely with the experimental result, most likely because of a lack of large rotation in the numerical model although non-linear geometry option is activated. Likewise the imperfections and material inclusions such as voids, air bubbles

uniformity of adhesive pre-treatment and errors caused by the testing equipment can be considered another source of the errors. However, a quite sufficient proximity of the numerical failure loads was captured with the experimental data for each joint configurations, indicating that the cohesive zone model is more practical in evaluating failure load than stiffness variation.

To understand the deviation of numerical failure loads from the experimental data, a step plot was constructed as shown in Fig 5.18 which represents the ratio of predicted and experimental failure load (F_n/F_{ex}) at each joint configurations. The horizontal axis represents the length of overlap and adherend thickness at each data point. The green line representing the equality of predicted and experimental failure loads ($F_n/F_{ex}=1$) is chosen as a baseline to indicate amount of error. It was observed that there is not a fixed value of the error, changing with the joint configurations and adhesive material parameters. This is most likely the reason of rotation of adherends at different adherend thicknesses and overlap lengths. It was found out that the errors for each configuration remain in the range of +18% and -15 % as illustrated in Fig 5.18, with an average value of 11 percent error corresponding to $F_n/F_{ex}=1.11$, which are in the acceptable limits.

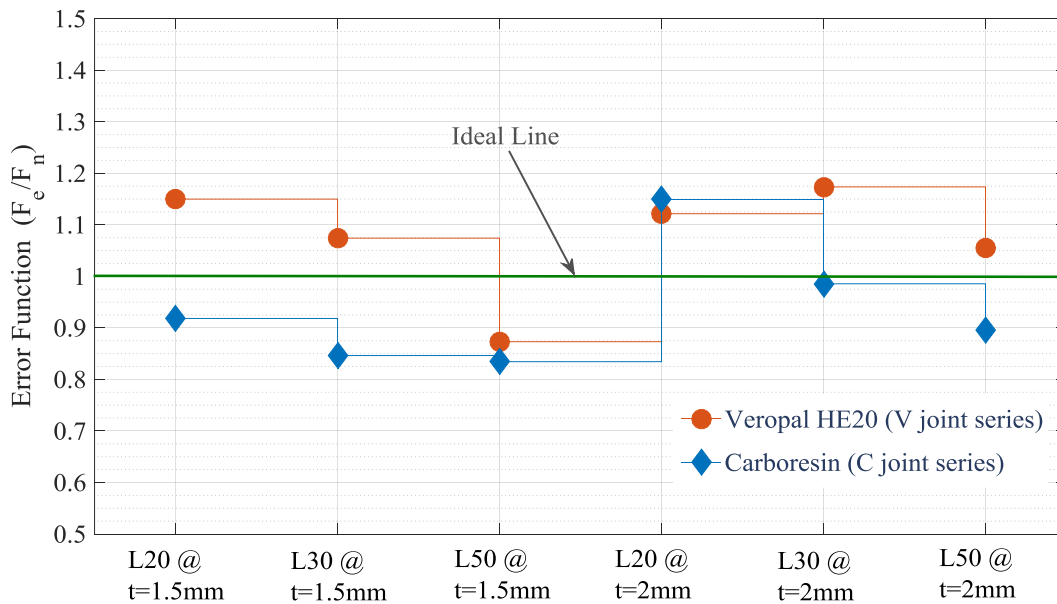


Fig 5.18 The distribution of errors reference to experimental data for each single lap joint configuration.

5.3.2 Material and geometry dependent parametric study

There are two categories of parameters that affect the failure load of the single lap joints; material and geometry parameters of both adherend and adhesive material. To understand effects of each of them, a parametric study should be implemented in FE analysis. It would be also possible to create a correlation based on design parameters of the single lap joint. Therefore, it would be quite practical to precise expression of failure loads in the range of described error function above. To perform this task, the parameters for parametric study can be divided in to two groups; first the geometric parameters such as thickness of adherend “t”, and overlap length “L”, secondly material parameters of adherend and cohesive zone model (e.g. yield stress of the adherend, critical traction stress, initial stiffness and specific fracture energy of the adhesive material). In practical applications, the adhesive thickness should be as thin as possible to acquire maximum joint performance. In this study, adhesive thickness is fixed to 0.1mm recommended for a variety of adhesive applications in industry. Thus all the cohesive zone parameters are derived considering this constant thickness for the parametric study. Additionally, the effect of initial stiffness (penalty parameter) on the failure load is infinitely small such that increasing the initial stiffness ten times decreases the joint strength by only 1.3 percent. Actually it is the reason of employing cohesive zone model which is nearly zero thickness. Thus initial stiffness was not included in the parametric study as a design variable. Consequently, the design parameters for the parametric study are described in Table 5.4 for the FE analysis.

Table 5.4 Geometry and material design parameters of the single lap joint model for the FE parametric study.

Overlap Length, L (mm)	Adherend thickness, t (mm)	Critical traction, σ_c (MPa)	Specific Fracture Energy, Γ_c (N/mm)	Adherend yield stress σ_y (MPa)
10	1	15	0.5	200
20	2	25	1	300
30	3	40	1.5	400
40				
50				

Three different adherend materials having the yield stresses of 200, 300 and 400MPa are selected to analyze for different plastic region behavior. Five overlap lengths of 10, 20, 30, 40 and 50mm with three adherend thicknesses of 1, 2, and 3mm are taken into account as a geometric design

parameters. One of the most critical challenge is to describe cohesive zone parameters in shear (Mode II) as a function of them in normal direction (Mode I). In the failure concept Von Mises criterion is implemented to evaluate critical traction in pure shear mode such that $\sigma_s^c = \sqrt{3} \sigma_n^c$. Likewise, initial stiffness value in shear mode can be expressed as $K_{ss}^0 = K_{nn}^0 / 2(1+\nu)$ where ν is the Poisson's ratio of the bulk adhesive. The relation between fracture energy in shear and normal mode can be derived assuming the critical separation ratio ($\lambda = \delta_c / \delta_f$) for each mode is identical. Substituting the relations amongst them for critical traction stress and initial stiffness in Eq. 4.12 gives $\Gamma_{II} = 2/3(1+\nu)\Gamma_I$ for the critical fracture energy rate in shear mode. It means that only design parameters in normal mode would be sufficient to perform parametric study. Therefore three traction stresses of 15, 25 and 40MPa were included in normal mode which represents the ultimate tensile strength of the bulk adhesive specimen considering the average strength range of the two component epoxy adhesive family. Similarly, three different specific fracture energy of 0.5, 1 and 1.5 N/mm are adopted to FE analysis, stimulating the both ductile and brittle behavior of the bulk adhesive as shown in Table 5.4. According to permutation of each variable, the total number of joint configuration is computed by multiplying parameters at each row such that ($5 \times 3^4 = 405$).

6

Numerical Results and Discussion

In this section, the FE simulation results are given to better understand the estimation of failure loads, stress singularities at the joint extremities for zero thickness joint design and definition of design parameters prior to manufacture process. For this reason, apart from the many numerous studies dealing with the single lap joint design fundamentals, the full scale nonlinear material response for both adhesive layer and the substrate material are implemented in order to figure out their effects on the joint strength. The nonlinear material models has been introduced in the previous chapters which includes accurate expression of the material behavior under tensile loading. Moreover, the stress vs strain diagrams for both material groups are constructed using the true stress strain points as an approximation of analytical equations. Therefore, this consideration provides a precise estimation of the simulation outputs such as stresses, deformations and failure loads for each joint configuration. Furthermore, in practical applications, the strength of the joint is highly dependent to geometry of the joint model. For example, implementing the zero thickness adhesive layer comes up with the some design problems. Because, as the layer gets thinner, the stiffness and some other mechanical properties such as tensile strength, fracture energy rate and toughness values are also substantially affected. To resolve this drawback, the adhesive layer is replaced by a zero thickness cohesive zone model considering the thickness effects as presented in Chapter 4.

The single lap joint design parameters can be divided into two subgroups; geometry and material parameters. In this part, overlap length “L” and adherend thickness “t” are taken as geometrical parameters whereas adherend yield point “ σ_y ” and adhesive tensile strength “ σ_a ” are the material

parameters. The evaluation of adhesive fracture energy rate and initial stiffness of the adhesive layer “ K_0 ” is also another point of interest in the stage of joint design. Consequently, the influence of each parameter group on the joint modelling and design can be categorized by the following subsections.

6.1 Interface Stress Analysis

The peeling and shear stress variations along the bondline are one of the key factor in determining progressive failure mechanism in the single lap joints. Accordingly, it is quite essential step how the stress singularities at the edges vary at zero thickness glue layer due to decreasing eccentricity. Because, at various overlap lengths and adherend thicknesses, the stress distribution is highly influenced as a result of bending moment and joint rotation. To emphasize the variation of the stresses through the bondline, normalized stress expression which is the ratio of maximum stress to average stress in the joint as a measure of stress concentration factor is introduced as the assessment tool. In the following section, the normalized peeling and shear stress distributions with respect to overlap length “ L ” and adherend thickness “ t ” are given.

6.1.1 Peeling Stress Distributions

The normalized peeling stress variation for the adherend thickness of 1mm is presented in Fig. 6.1 at each overlap length (10, 20, 30, 40 and 50mm). The point on the middle of the adhesive bondline is defined as the origin. Left and right endpoints in the figure represent the joint extremities in positive and negative direction. It is apparently observed that the maximum normalized stress becomes larger as the overlap length increases. However, it is not very critical issue at higher overlap lengths because it has only critical effect in a small distance considering the whole overlap length. Besides, the peeling stress does not exist over a large distance at higher overlap length excepting the joint extremities. One of the main reason is the bending stiffness of the joint allowing to joint rotate about the origin at relatively low adherend thickness ($t=1\text{mm}$). Actually, the peeling stress has a proportionality with the adherend bending stiffness. Furthermore, overlap length is found out to be a critical parameter in eliminating peeling stresses. For example, peeling stress exists throughout the overlap length of 10mm whereas it seems partially at higher values. It can be said that the overlap length has an optimum value between 20 and 30mm in terms

of its existence and peak value over the bondline at low thickness or bending stiffness of the substrate material.

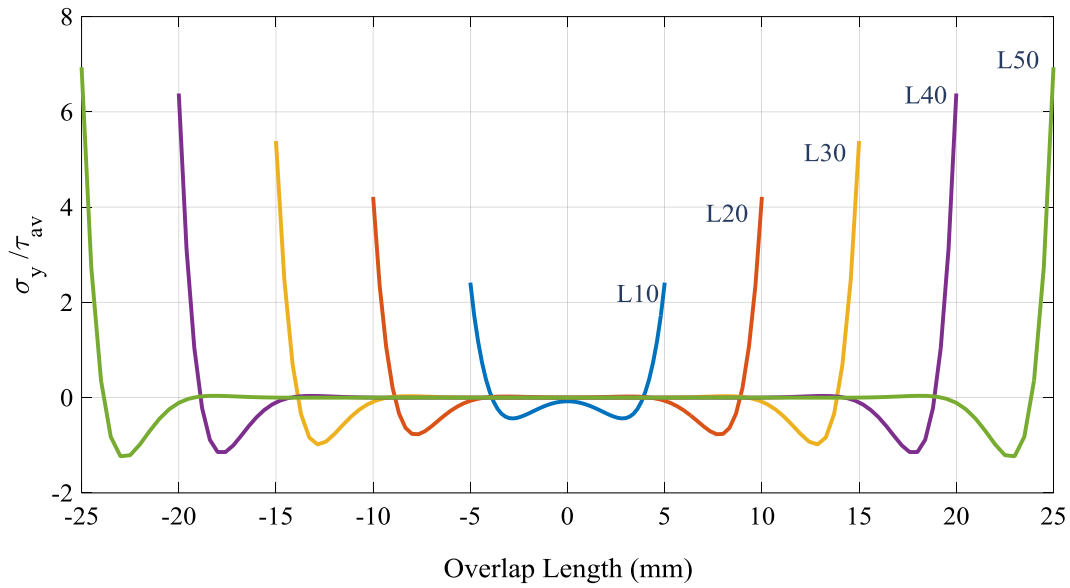


Fig. 6.1 Normalized peeling stress distribution over the bonded length at $t=1\text{mm}$.

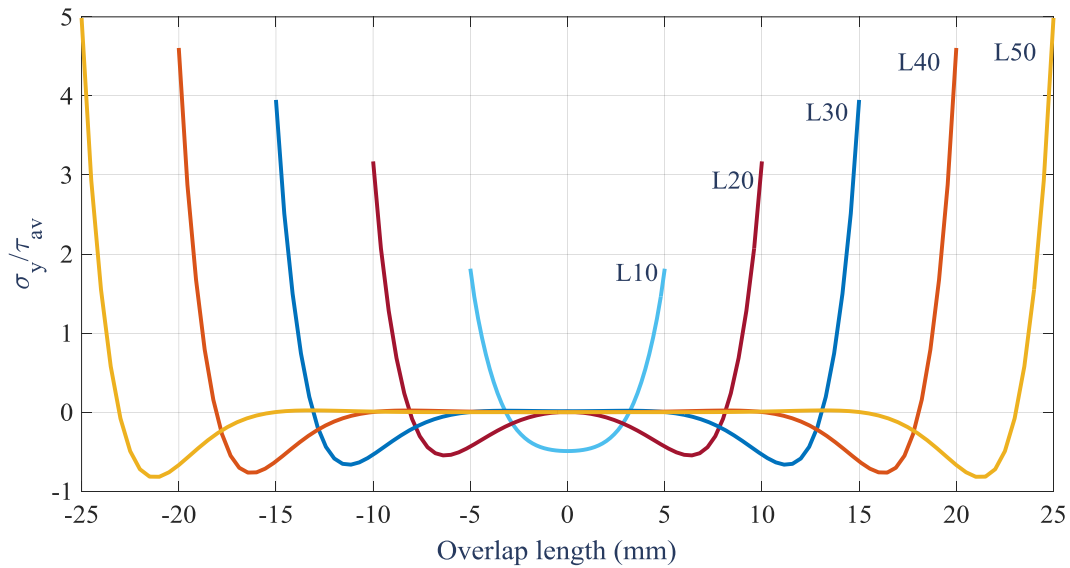


Fig. 6.2 Normalized peeling stress distribution over the bonded length at $t=2\text{mm}$.

The normalized peeling stress variation for $t=2\text{mm}$ and $t=3\text{mm}$ are illustrated in Fig. 6.2 and 6.3, respectively. The variation gets smoother in negative stress direction and the peeling stress appears

over a larger area due to increasing adherend thickness. As mentioned above, the joints having higher flexural stiffness exhibit a resistance against rotation which creates considerable peeling stresses through the overlap lengths. This situation is more visible in Fig. 6.3 for $t=3\text{mm}$. so that implementation of adherend thickness

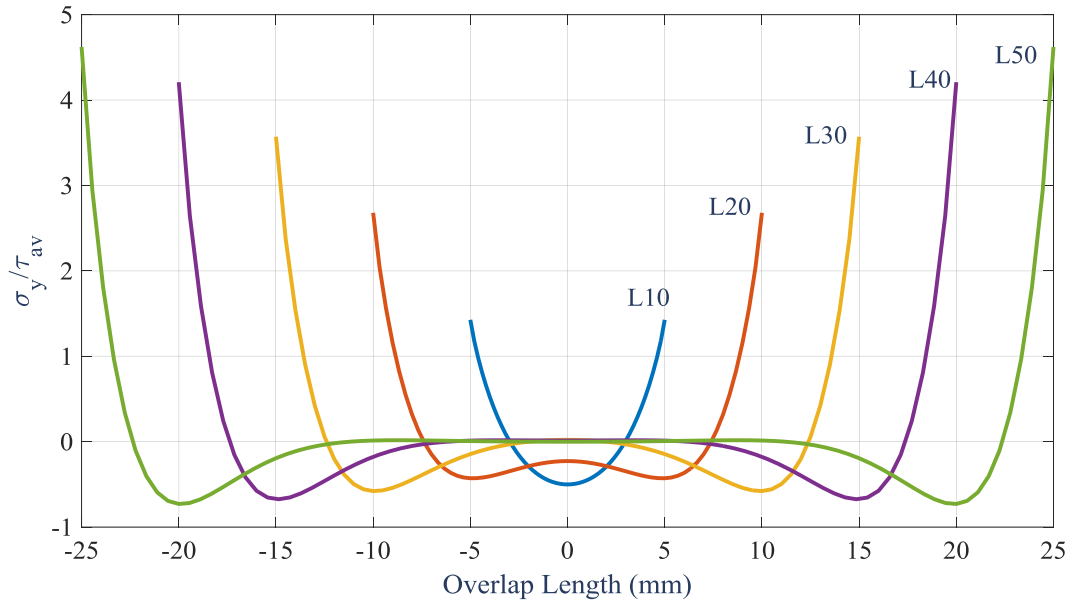


Fig. 6.3 Normalized peeling stress distribution over the bonded length at $t=3\text{mm}$.

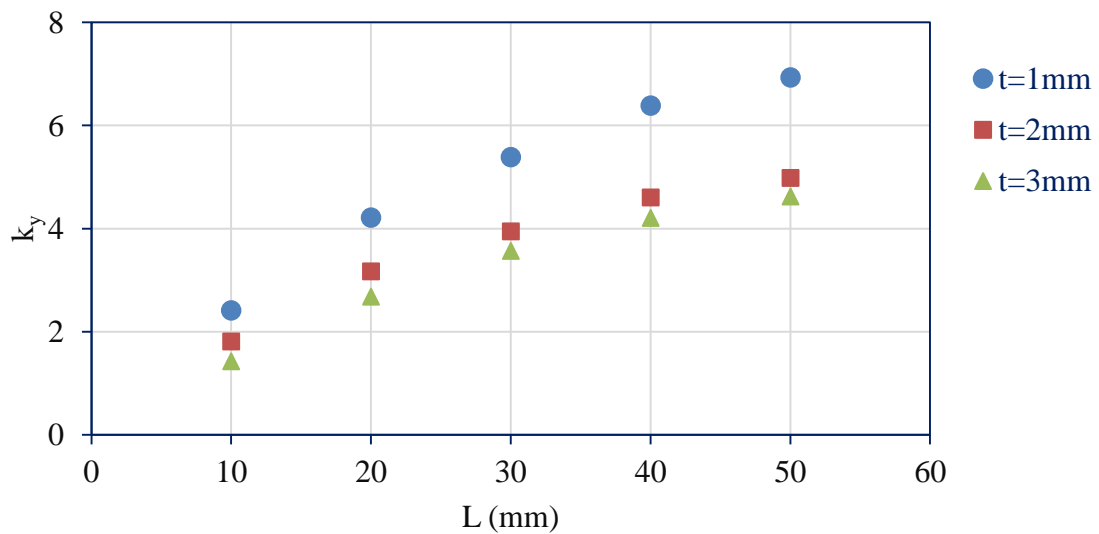


Fig. 6.4 The peak values of normalized peeling stresses (k_y) for each adherend thickness.

more than 2mm results in a peeling stress over the all bonded area. Moreover, the peak values of the normalized peeling stress is also a critical design parameter for the adhesive joints as illustrated

in Fig. 6.4. This figure expresses that the stress concentration “ k_y ” increases exponentially with the overlap length and adherend thickness but eventually it reaches a critical constant value (horizontal asymptote). In this regard, a balance between overlap length and k_y should be established for optimization purposes of the joint geometry. As an ideal moderate value, where $k_y=3-5$ and $L=20-30\text{mm}$, is observed to be quite feasible for the joint geometry in avoiding peeling stress.

6.1.2 Shear Stress Distributions

In many adhesive joint applications, the distribution of shear stresses through the bonded area is of importance since the source of failure is dominantly shear stresses particularly for thick and rigid adherends. In this section, normalized shear stress distributions for each adherend thickness and overlap length are given similar to those in the previous section. In the same way, normalization is made by dividing the local shear stress value to average stress at the bonded region. The average stress is expressed dividing the uniaxial tensile force, corresponding to 0.01mm displacement in loading direction for each case, to bonded area ($A=wxL$). The variations are constructed as a result of FE solutions for each configuration and illustrated in Fig. 6.5, 6.6 and 6.7 for the adherend thicknesses of 1, 2 and 3mm, respectively. The desired shear stress distributions are expected to be located as much as close the line where normalized shear stress value is equal to 1. This is an indication of ideal case in which all the local shear stresses are identical and equal to average stress value. It is inferred from the results that the shear stress concentration values ($k_{xy}=\tau_{xy}/\tau_{av}$) rise up with higher overlap length for each adherend thickness (see Fig. 6.5, 6.6 and 6.7).

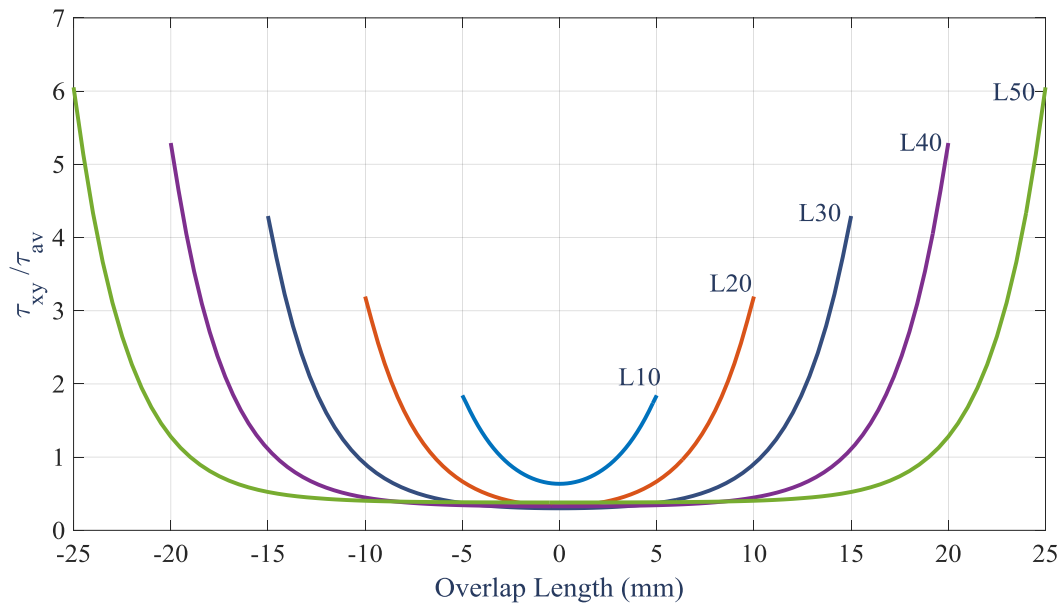


Fig. 6.5 Normalized shear stress distribution over the bonded length at $t=1\text{mm}$.

On the other hand, the uniformity of the stress distribution is remarkably distorted which yields sharp changes through the bondline. In order to determine an optimum point, these two parameters (uniformity and peak values) should be precisely controlled in the design of the joint geometry. For example, application of relatively thinner adherends in the joint model can be declared as a key factor to obtain uniform shear stress distribution.

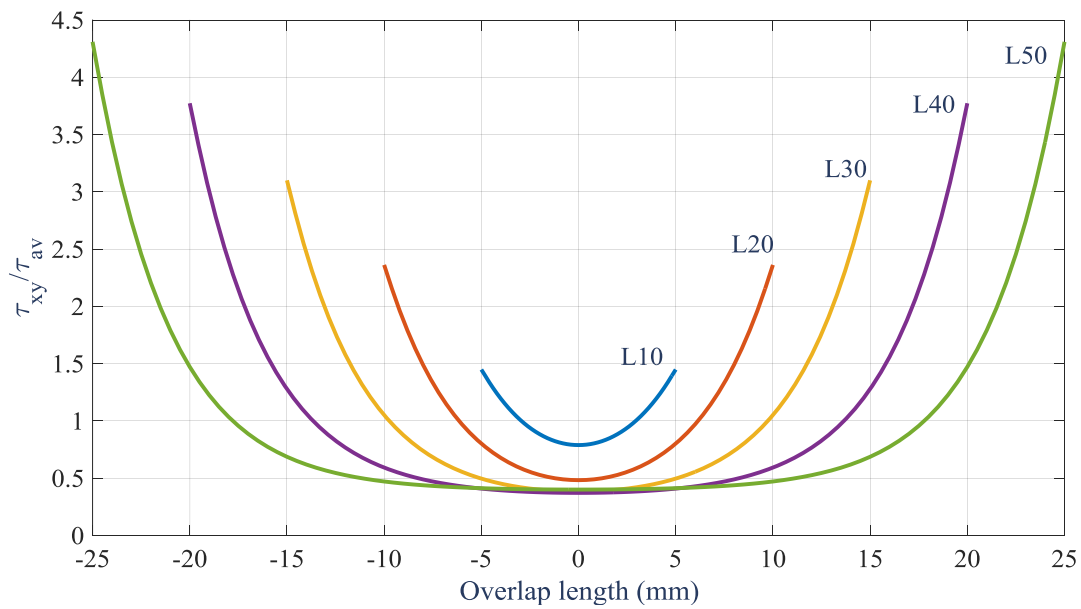


Fig. 6.6 Normalized shear stress distribution over the bonded length at $t=2\text{mm}$.

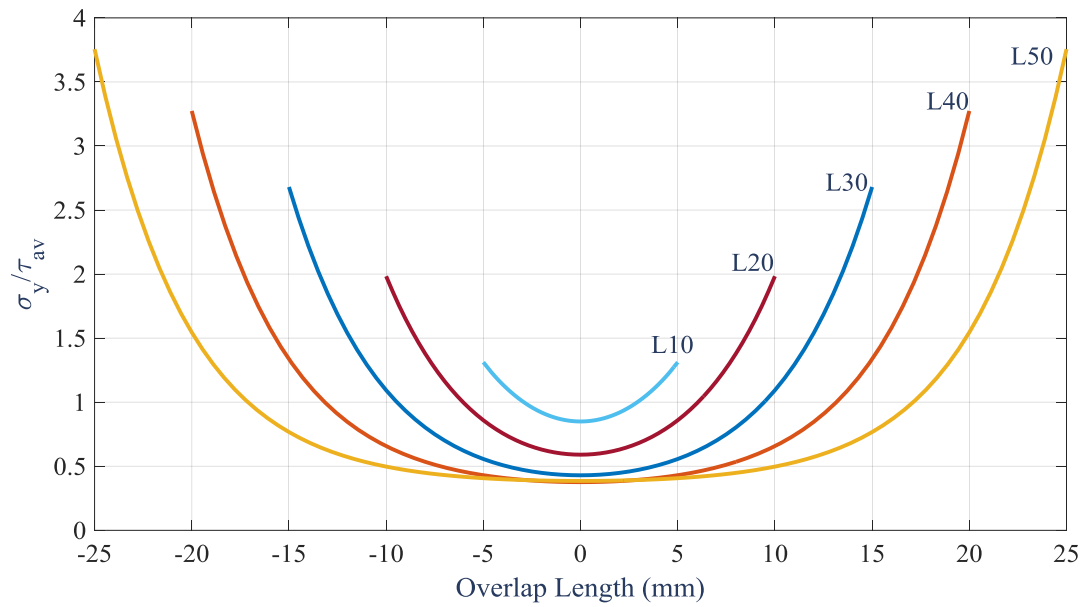


Fig. 6.7 Normalized shear stress distribution over the bonded length at $t=3\text{mm}$.

The peak normalized shear stress values at the joint extremities for each specific joint configuration are depicted in Fig. 6.8. Similar to peeling stresses, the k_{xy} values increases with increasing overlap length and decreasing adherend thickness. Therefore, k_{xy} is a quite complicated design factor since it plays a substantial role in the failure initiation, propagation and final fracture.

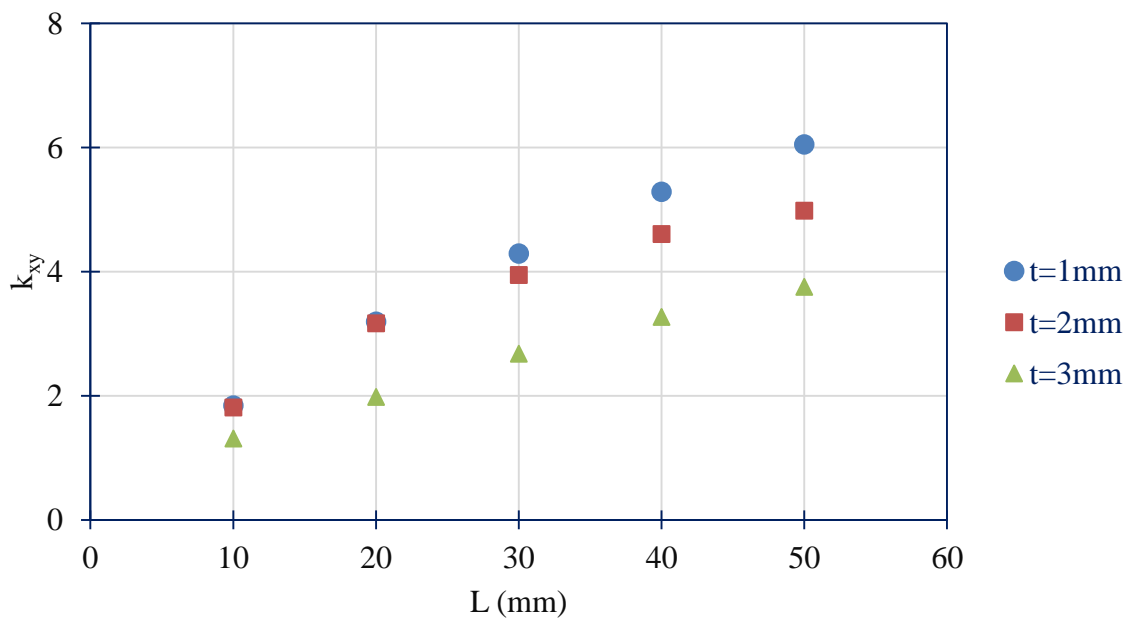


Fig. 6.8 The peak values of normalized peeling stresses (k_{xy}) for each adherend thickness.

6.2 Load Carrying Capacity of the Single Lap Joints

In this section, the load carrying capacity of the single lap joint numerical models are investigated. The adhesive joints are loaded in the uniaxial direction with a displacement control until the load starts to drop after a critical value. In this case, the maximum force sustained in the adhesive joint are assumed to be the load carrying capacity. In this present investigation, the peak load F_w (N/mm) and its influence factors are presented in the following sections. The peak load (failure load) is expressed to be the maximum value during the FE simulations and evaluated per unit width of the bonded area. In fact, the load carrying capacity of a joint may be affected by two groups of categories: the first is about the material parameters such as initial stiffness K_0 , adhesive ultimate tensile (separation) strength σ_a , adhesive specific fracture energy; the second group is related to geometry parameters such as overlap length L and adherend thickness t . To analyze performance of an adhesive joint, each group of parameter should be evaluated in detail to facilitate design procedure. In order to perform this task, various parameters belonging to each group of factor are selected considering the limit values of each of them in real and practical applications. Thus, as a geometrical parameter, five different overlap lengths of 10, 20, 30, 40 and 50mm with three different adherend thicknesses of 1, 2 and 3mm are taken into consideration. In the scope of this study, only structural mild steel are simulated as an adherend material with full scale nonlinear material model as mentioned previously. Therefore, three groups of structural steels each has a yield strength of 200, 300 and 400MPa representing the low, medium and high strength structural mild steels are selected respectively. The modulus of elasticity is taken as 200GPa for each. Accordingly, the adhesive material modelled with three different separation strengths of 15, 25 and 40MPa representing the three strength levels for epoxy adhesives.

6.2.1 Effect of Adhesive Ultimate Tensile Strength and Stiffness

One of the most dominant factors on the failure load is the tensile strength of the adhesive material. Accordingly, the initial stiffness value which is expressed as E/η ratio, has relatively ignorable since the interface between two substrates are assumed to be very thin. So that the interface stiffness becomes very high such that increasing the modulus of elasticity of the adhesive ten times results in nearly 1.5% difference of the joint failure load. Therefore, the strength of adhesive layer which connects two similar substrates together can be dictated as a source of failure in many adhesive joint applications. In this regard, the variation of failure load per unit width are

processed according to overlap length, adherend thickness and adhesive strength. The trends of the failure loads are given in Fig. 6.9, 6.10 and 6.11 corresponding to each group of parameter. It should be noted that the higher adhesive strength improves the load carrying capacity of the joint up to an overlap length of 30mm for $S_y=200\text{MPa}$ and 40mm for $S_y=300\text{MPa}$, respectively as clearly seen in Fig. 6.9a and 6.9b. This critical overlap length is the result of adherend failure at lower thickness (1mm) and yield strength (200 and 300MPa).

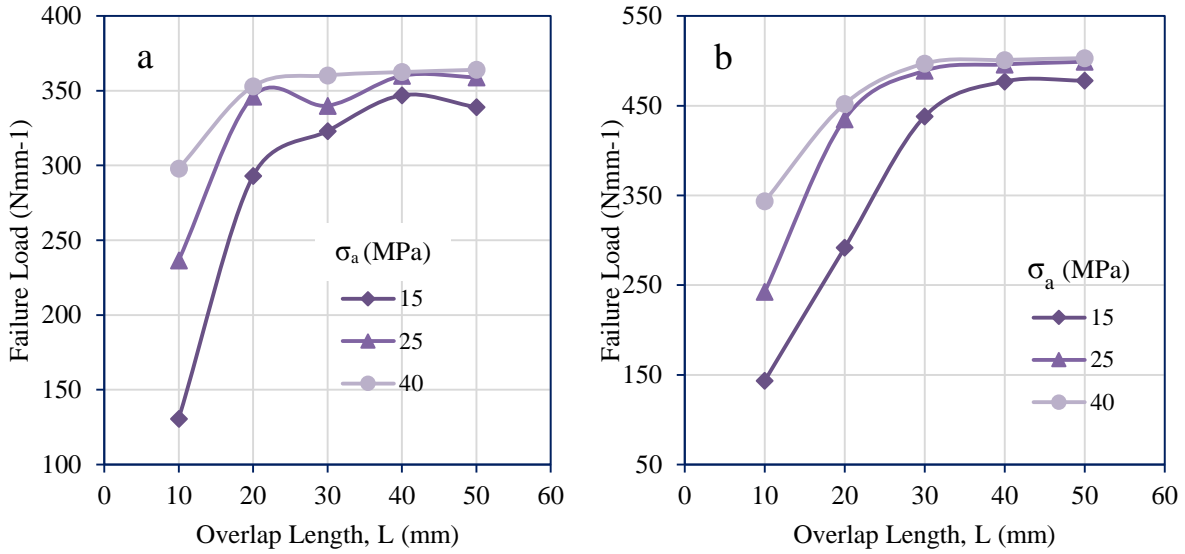


Fig. 6.9 Failure loads of the joints for the adherend yield stress of (a) $S_y=200\text{MPa}$ and (b) $S_y=300\text{MPa}$ having both identical adherend thickness of $t=1\text{mm}$.

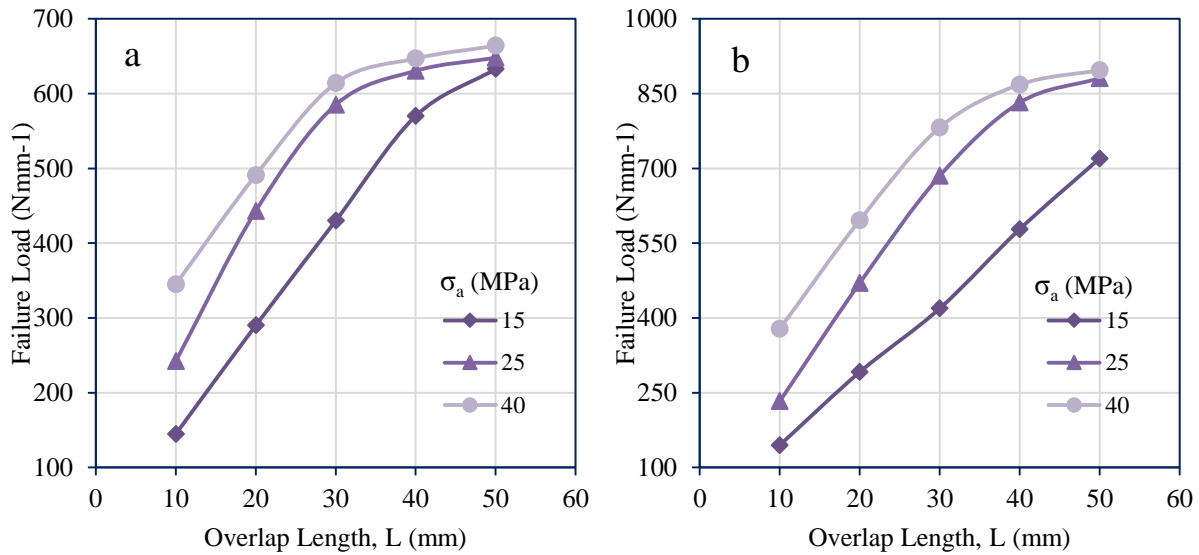


Fig. 6.10 Failure loads of the joints for the adherend yield stress of (a) $S_y=200\text{MPa}$ and (b) $S_y=300\text{MPa}$ having both identical adherend thickness of $t=2\text{mm}$.

After reaching critical adherend strength, the failure loads are almost remain constant regardless of the adhesive strength as illustrated in Fig. 6.9a and 6.9b. However, the scenario is a little bit different for the adherend thickness Of 2mm. In this case, the critical joint strength is observed to be shifted to an overlap length of 40mm at high adhesive strength values. Furthermore, the trend of failure load exhibits a linear behavior up to 600Nmm^{-1} at low adhesive strengths since the adherend strength limit value is not reached (see Figure 6.10).

When the adherend thickness becomes larger (i.e $t=3\text{mm}$), the load carrying capacities emerge nearly linear response with respect to overlap length at each adhesive strength value. But the adhesive strength has a substantial influence in this interval since the rotation of the joint is constrained as a result of adherend rigidity. Thus the critical limit value is shifted beyond the 50mm of overlap length. In this interval, it seems possible to establish a relationship in estimating failure load of the joint where failure loads change between 150 and 850Nmm^{-1} for the case in Fig. 6.11a, 150 and 1150Nmm^{-1} for the case in Fig. 11b, respectively. It means that the influence of adhesive strength is more apparent and effective at higher adherend thicknesses. It should be noted that larger overlap lengths can be implemented to obtain maximum joint performance in the case of thicker adherends. In this regard, one of the most vital challenges are how to eliminate high amount of peeling stresses as described in previous sections.

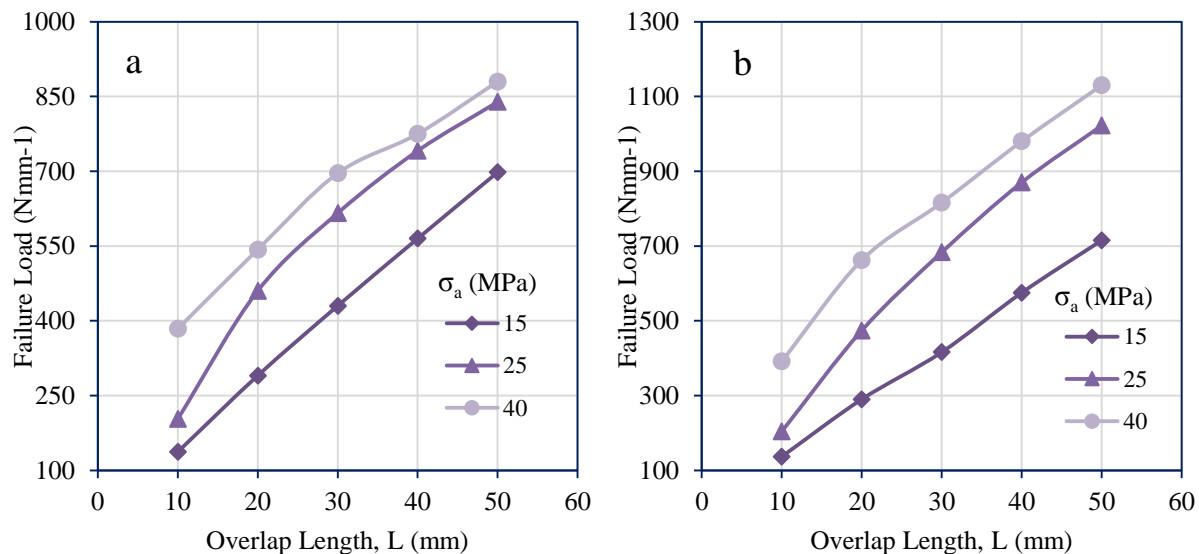


Fig. 6.11 Failure loads of the joints for the adherend yield stress of (a) $S_y=200\text{MPa}$ and (b) $S_y=300\text{MPa}$ having both identical adherend thickness of $t=3\text{mm}$.

It is reasonably observed that the application of high strength adhesives are feasible at low overlap lengths in the range of 10 and 30mm for each configuration. In addition, it is not limited to 30mm overlap length for thicker adherends ($t > 2\text{mm}$) if the high amount of peeling stresses are avoided at the joint extremities.

6.2.2 Adherend Rigidity Effect

One of the most critical factors to determine the limit of the load carrying capacity is the adherend rigidity. This section gives the main reason of how this parameters affects and confines the peak loads. Notice both adherend thickness and yield strength contribute the adherend rigidity, a simple parameter should be introduced representing both of their influence in the adherend rigidity. Since these two parameters (t and S_y) increases the rigidity, a new rigidity parameter $S_y t$ can be used to predict variation of failure load. This is actually an important design parameter that should be precisely chosen for the maximum sustainable joint load. Because increasing adhesive strength and overlap length of various joint combinations having the same rigidity is not necessary as a result of adherend failure. In order to understand this effect, the trends of failure load for each overlap length (10, 20, 30, 40 and 50mm) and rigidity parameter (between 200 and 1200 Nmm^{-1}), are depicted in Fig. 6.12, 6.13 and 6.14. Rigidity parameters are calculated as a combination of all thickness and yield stress values in the concept of this study. It can be concluded from the plots that there is generally a critical point for each joint configuration at which increasing adherend rigidity parameter does not change the failure load. Accordingly, the failure loads are not dependent

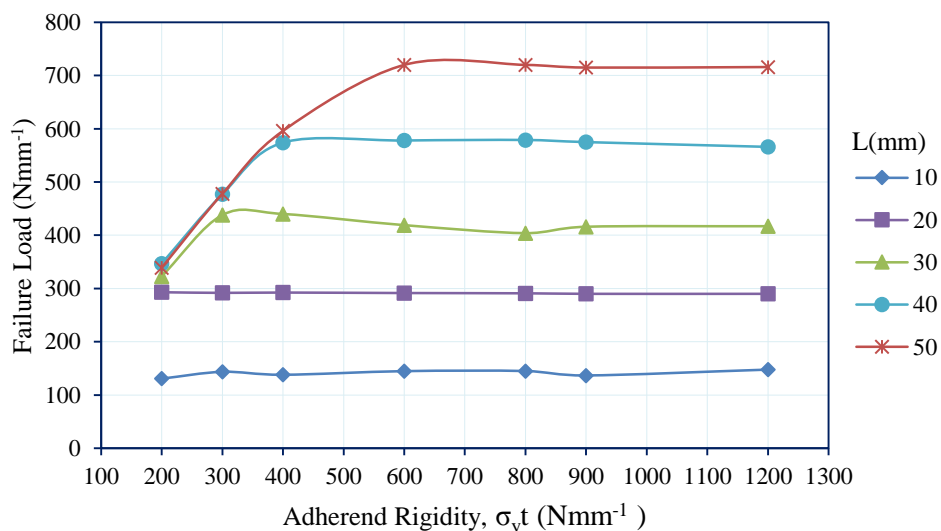


Fig. 6.12 Graphical illustration of the adherend rigidity influence on the joint strength for $\sigma_a = 15\text{MPa}$.

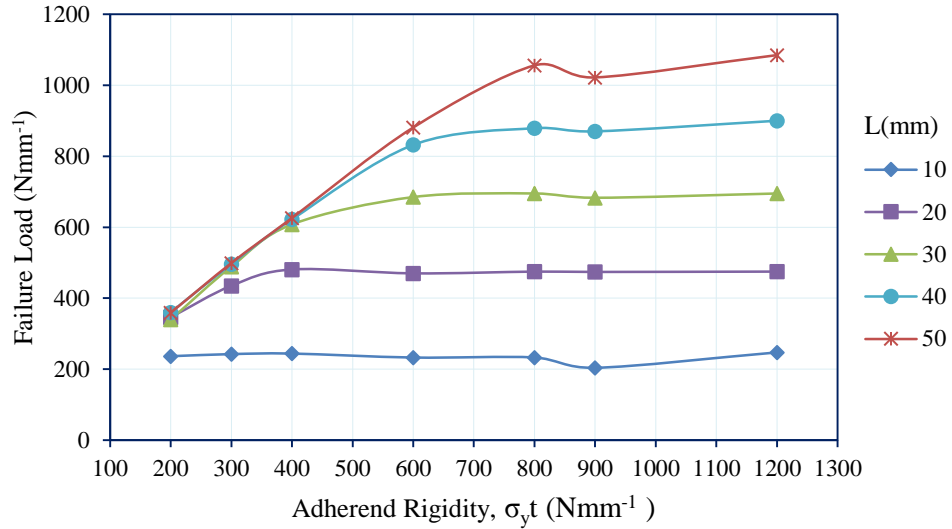


Fig. 6.13 Graphical illustration of the adherend rigidity influence on the joint strength for $\sigma_a=25\text{MPa}$.

to adherend rigidity at low overlap lengths such as 10, 20 and 30mm (see Fig. 6.12). But, it is quite dominant at higher overlap lengths and higher adhesive strengths. However, it is possible to see different circumstances for higher adhesive strengths (in Fig. 6.13 and 6.14) in which the critical point shifted through the horizontal axis. For this reason, the range of effective region is large at high overlap length and adhesive strength so that it should be taken into account prior to design stage. Fluctuations between 800 and 900Nmm⁻¹ in all graphs is detected to be a result of failure loads corresponding to different t and S_y values even though their rigidity parameters are the same.

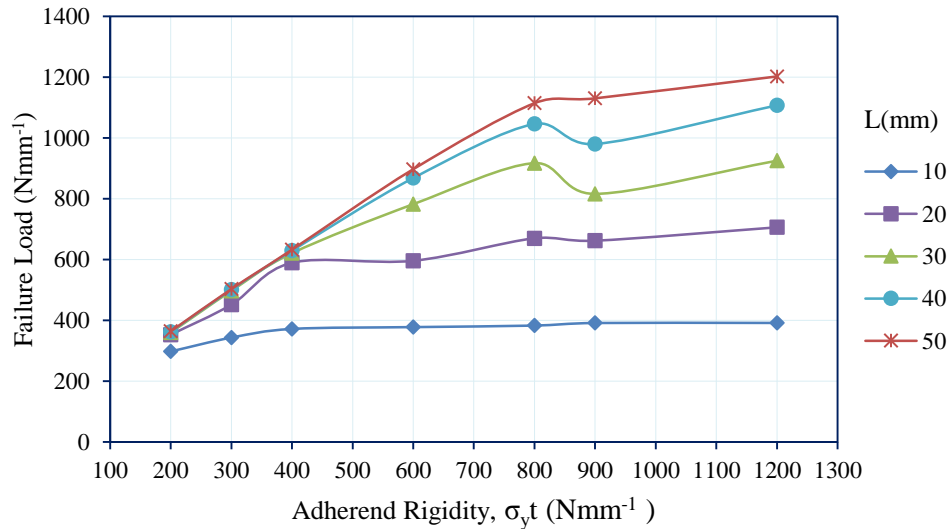


Fig. 6.14 Graphical illustration of the adherend rigidity influence on the joint strength for $\sigma_a=40\text{MPa}$.

6.2.3 Overlap Length Effect

The surface plots depicting the influence of selected overlap lengths with respect to adherend yield strength and thickness are given in Fig. 6.15, 6.16 and 6.17 each corresponds different adhesive strength. Hence it would be easier to evaluate variations based on two design variable since the overlap length analysis is a complex phenomena. The relationships for ductile and brittle adhesives are expected to be similar because the adhesive layer is modelled with a zero thickness cohesive zone model at the interface. The overlap length is observed to be a very sensitive parameter at high adherend strength and thickness. Contrary, it does not have a considerable effect at the regions where yield strength and thickness are lower (see Fig. 6.15, 6.16 and 6.17). It is also more visible at higher adhesive strengths and the joint strength fluctuates nearly between 200 and 300 Nmm^{-1} . Furthermore, the influence of L becomes less and uniform for $\sigma_a=25\text{MPa}$ and 40MPa . The influence of L exhibits a relationship having a direct proportionality with the adherend rigidity and inverse proportionality with the adhesive strength as seen in the Figures. This behaviour is actually a result of adherend flexural stiffness which induces rotation about the middle axis. The more adhesive joints are exposed to rotation, the more peeling stress singularities are induced at the joint edges regarding to adhesive properties. Therefore, applying large overlap lengths is useless in terms of separation at the edges due to the peeling process. As it is illustrated in Fig. 6.15, 6.16 and

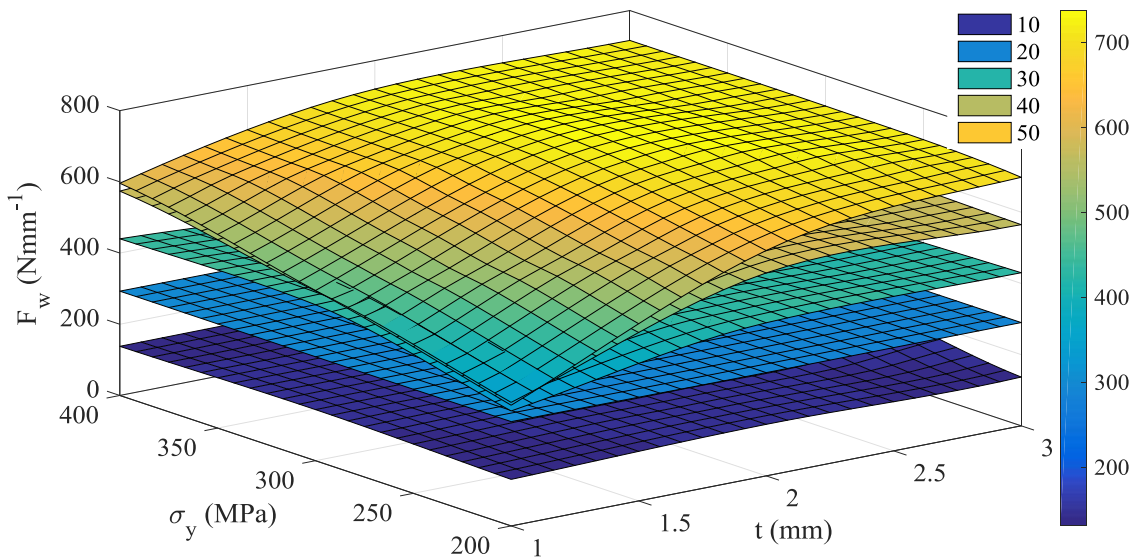


Fig. 6.15 3-D representation of overlap length influence on the joint strength as a function of adherend thickness and yield stress for the adhesive ultimate tensile stress of $\sigma_a=15\text{MPa}$.

6.17, there is generally an optimum area for deciding the overlap length. The parameter ranges that can be given for the effective overlap length are; $\sigma_y=250-400\text{MPa}$ and $t=1.5-3\text{mm}$ at $\sigma_a=15\text{MPa}$, $\sigma_y=300-400\text{MPa}$ and $t=2-3\text{mm}$ at $\sigma_a=15\text{MPa}$, $\sigma_y=350-400\text{MPa}$ and $t=2-3\text{mm}$ at $\sigma_a=15\text{MPa}$, respectively. Considering the intervals, it is suggested that the overlap length is the key factor at high stiffness adherends in order to enhance adhesive joint strength.

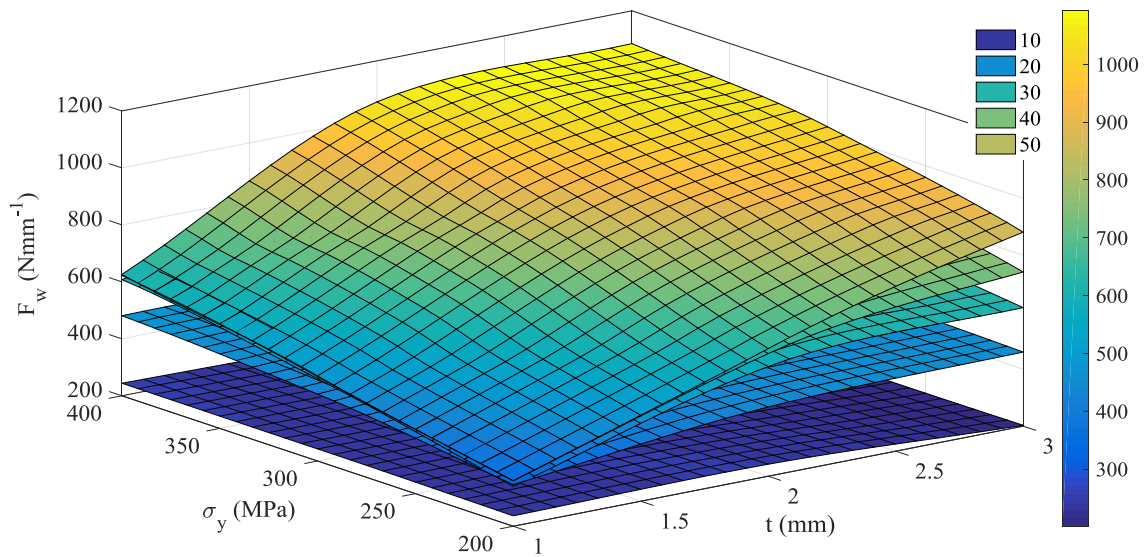


Fig. 6.16 3-D representation of overlap length influence on the joint strength as a function of adherend thickness and yield stress for the adhesive ultimate tensile stress of $\sigma_a=25\text{MPa}$.

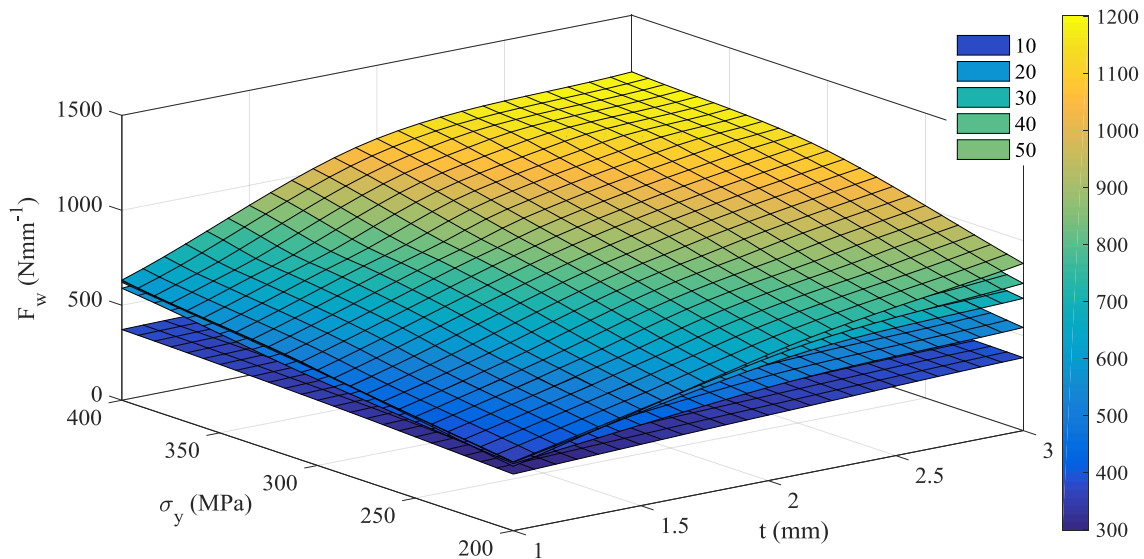


Fig. 6.17 3-D representation of overlap length influence on the joint strength as a function of adherend thickness and yield stress for the adhesive ultimate tensile stress of $\sigma_a=40\text{MPa}$

6.2.4 Adhesive Fracture Energy Rate Effect

In the case of applying cohesive zone model, specific fracture energy Γ and separation strength are two substantial parameters, which would affect the failure load of adhesive joints together. Among them, the influence of separation strength has been investigated by many authors [52-55]. Therefore, the influence of Γ is included by keeping separation strength identical. However, in many adhesive applications, increasing the fracture energy rate substantially rises the load carrying capacity of the adhesive joints. On the contrary, it is worth to analyse individual effect of fracture energy in the traction-separation curves of the cohesive zone model as seen in Fig. 6.18, 6.19 and 6.20. Five different specific fracture energy values of 0.25, 0.5, 1, 2 and 4N/mm are selected for the evaluation process. The curves are constructed using the initial stiffness value K_0 as a slope of line up to maximum traction. Then the adhesive strengths (15, 25 and 40MPa) are assumed to be critical separation stress in normal direction. The critical stress in shear direction would be calculated considering the Von-Mises approach such that τ equals to 0.577σ . It is observed that the fracture energy influence emerges ignorable response until the initiation of separation for the adhesive strength of 15MPa (see Fig. 6.18). Then it increases the toughness of the adhesive layer causing the joint to elongate more until the fracture. In this case, it leads to joint riation and fast slow crack propagation during the loading after critical stress value is reached. Although it doesn't change the separation dramatically, the fast crack growth can be prevented in case of employing low strength adhesive ($\sigma_a=15\text{-}25\text{MPa}$). In contrast, the situation differs slightly

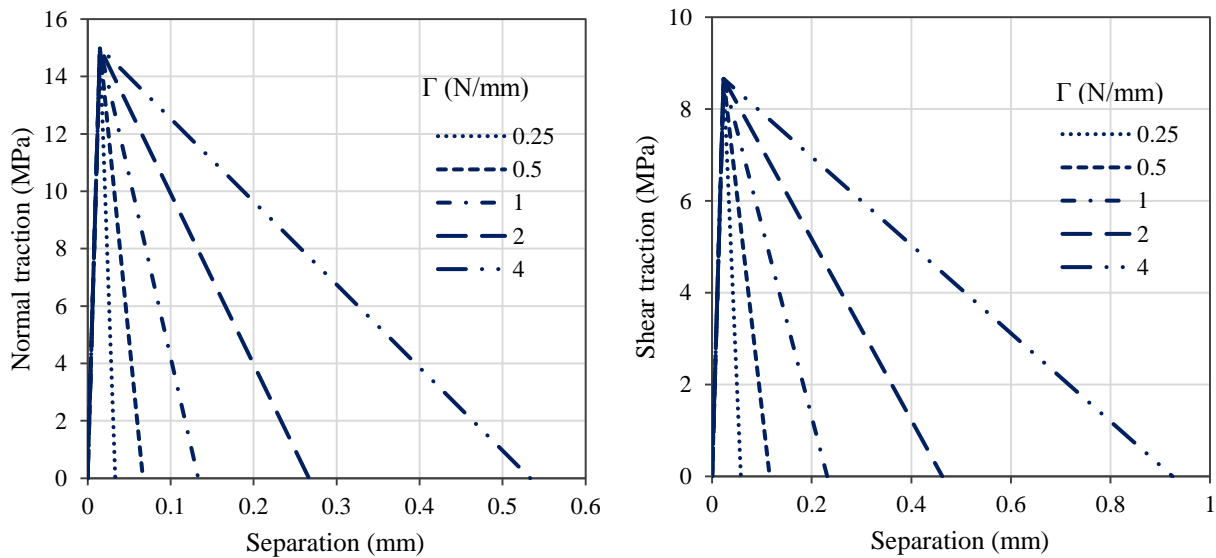


Fig. 6.18 Normal (on the left) and shear (on the right) traction-separation lines of the adhesive at various fracture energy values for critical traction $\sigma_a=15\text{MPa}$.

for the high strength adhesive (in Fig. 6.20). Because a negative slope after the critical traction stress is obtained for $\Gamma=0.25$ and 0.5N/mm . At this point, it is quite notable that the strength and stiffness of the adhesive should be higher than its nominal value in Fig. 6.20. Excepting the high strength adhesives, the influence of fracture energy for identical critical stress values is not an important issue. To ensure of the positive slope value, the fracture energy is taken as 1N/mm for failure load estimation in the present study.

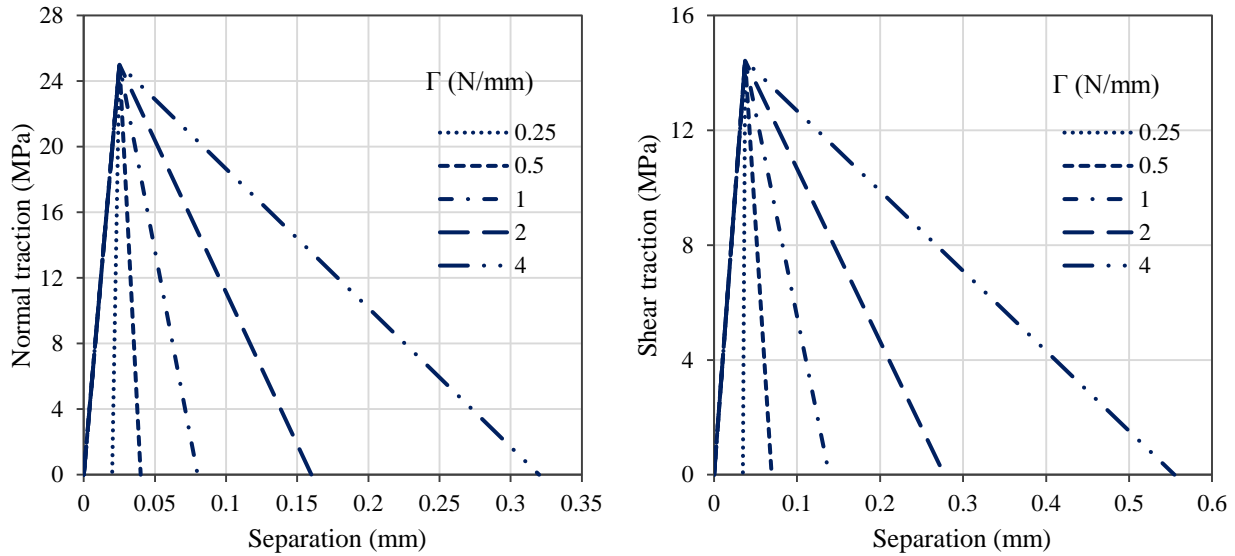


Fig. 6.19 Normal (on the left) and shear (on the right) traction-separation lines of the adhesive at various fracture energy values for critical traction $\sigma_a=25\text{MPa}$.

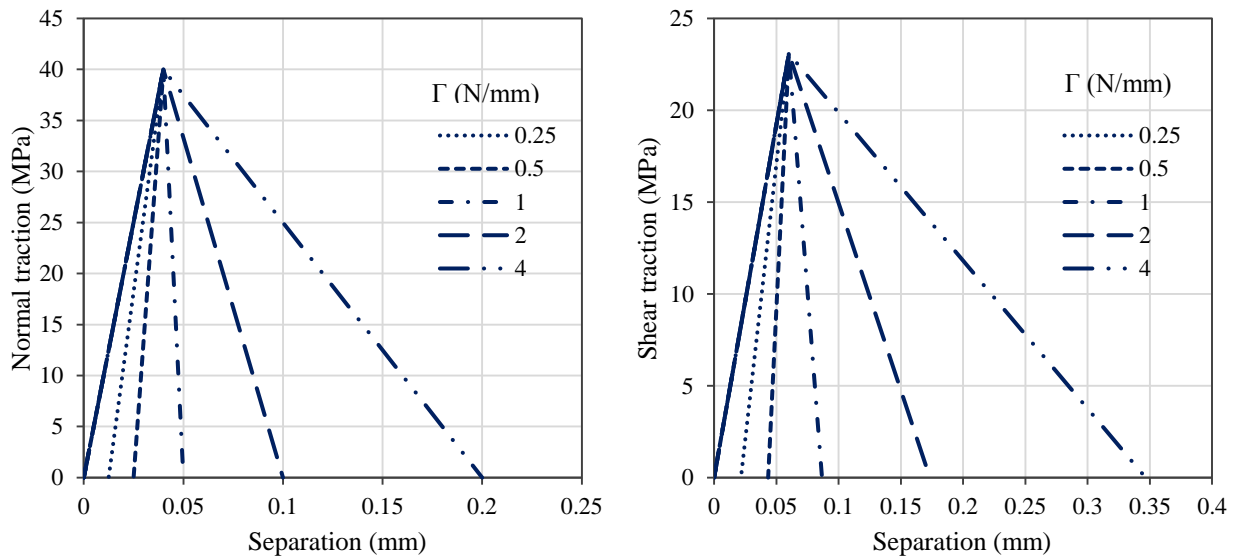


Fig. 6.20 Normal (on the left) and shear (on the right) traction-separation lines of the adhesive at various fracture energy values for critical traction $\sigma_a=40\text{MPa}$.

6.3 Adhesive Damage Model Analysis

Apart from the estimation of failure loads, the response of single lap joints under applied displacement is also a critical issue in terms of full scale damage analysis. In the adhesive joint there are mainly two types of failure; adhesive failure and cohesive failure at the interfaces. In this numerical model, cohesive failure is only covered since the bonded layer modelled with zero thickness cohesive zone. To perform this task, the displacement “ u ” is applied at one end of the joint then the reaction force per unit with (N/mm) is recorded during the FE simulation. The damage analysis is performed considering the random joint configuration for each overlap length of 10, 20, 30, 40 and 50mm. Because overlap length and adherend thickness have a dominant factor on failure occurrence. For example, the load versus displacement diagram for $L=10\text{mm}$ is given in Fig. 6.21 to evaluate failure mechanism. In this plot, the failure is examined at four different stages (see points a, b, c and d) which represent linear elastic, plastic, damage initiation and late stage damage propagation, respectively. The Von Mises stress distribution in the vicinity of bonded area corresponding to each marked point is shown in Fig. 6.22. The adhesive strength and adherend yield point is taken 25MPa and 300MPa simulating medium material parameters of the study. The joint exhibits a linear response up to point b then the adherend plasticization initiates. Then at point c, first damage initiation starts at point c, the adhesive reaches its maximum load carrying capacity

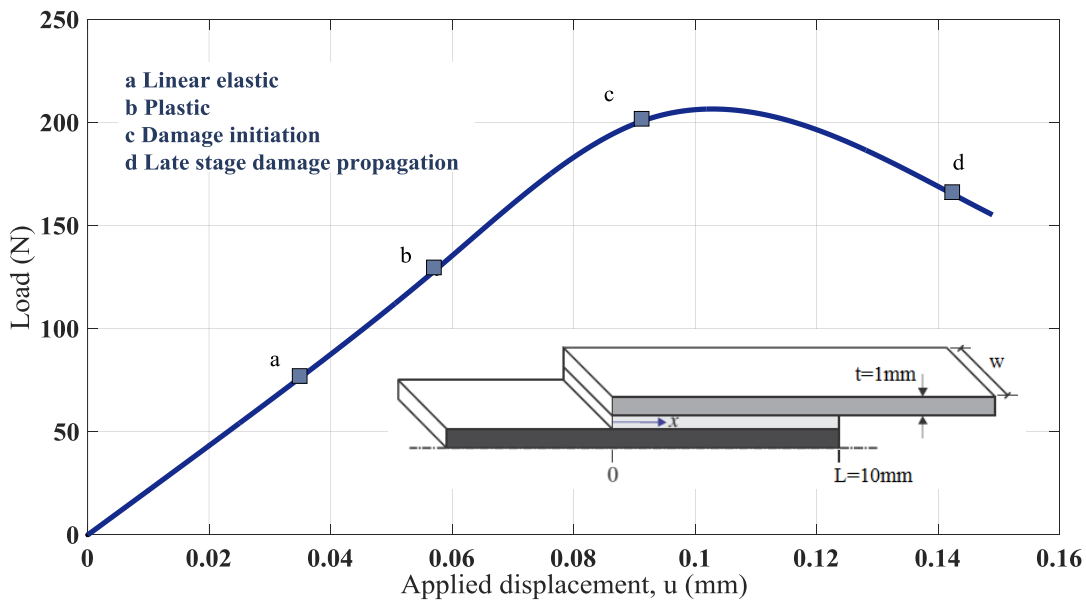


Fig. 6.21 Numerical predicted uni-axial load versus displacement response and failure steps of the L10 single lap joint configuration.

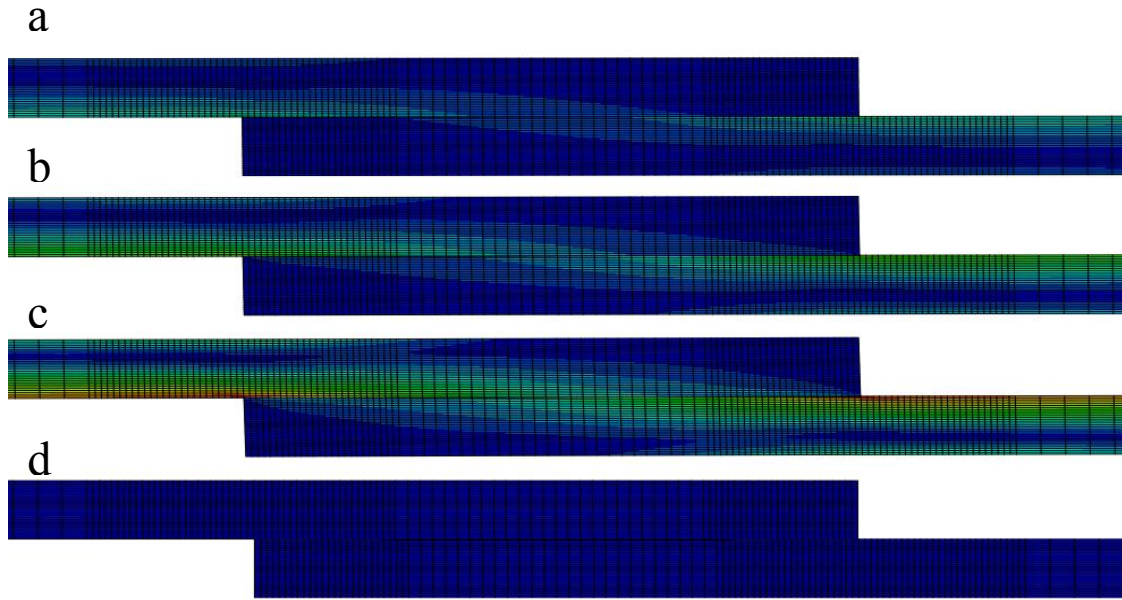


Fig. 6.22 Von-Mises stress distribution in the vicinity of the bonded area of the simulated L10 joint configuration (red is the maximum positive and blue is the minimum positive). The a-d subplots correspond to the linear elastic, plastic, damage initiation and late stage damage propagation, respectively, as described in Fig. 6.21.

and the load drops drastically (see Fig. 6.21). Finally, the crack propagation is completed at point d and full fracture occurs. Fig. 6.22 explains the progressive failure steps based on the Von Mises stress variation in the bonded area vicinity. At each consecutive instant, the magnitude of the stresses gets larger at the joint extremities and bonded length up to the last stage then the stress in the joint goes zero level (visible in full blue region in Fig. 6.22.d) since complete separation is achieved.

The progressive failure mechanism emerges the similar trends as mentioned above paragraph. But the geometrical design parameters such as overlap length and adherend rigidity can slightly change the failure behavior. For example, the trend of the load in Fig. 6.23 has a wider plastic region between the point b and d. This is result of applying low strength adherend with a yield strength of 200MPa and thickness of 1mm. Although, linear elastic region and plasticization remain similar to those in the previous figure, the joint exposes to high plastic deformation as result of reaching yield point of the adherend material (200MPa) before the failure initiation in the adhesive. For this kind of situations, a detail examination is needed to exactly understand either the adherend or adhesive fails. In order to seek a solution, progressive failure stages in the vicinity of bonded area corresponding to each point on the curve are illustrated in Fig. 6.24. Therefore, first separation of the cohesive zone is detected in Fig. 6.24d as an indication of the adhesive failure.

Accordingly, stress distribution around the overlap endpoints is generally the reason of the failure initiation due to local peak values as shown in Fig. 6.24. The regions in full red color characterize the plastic stresses which is quite apparent in Fig. 6.24d. When the first separation appeared the global joint stiffness drops dramatically then yields a sudden crack propagation up to final fracture.

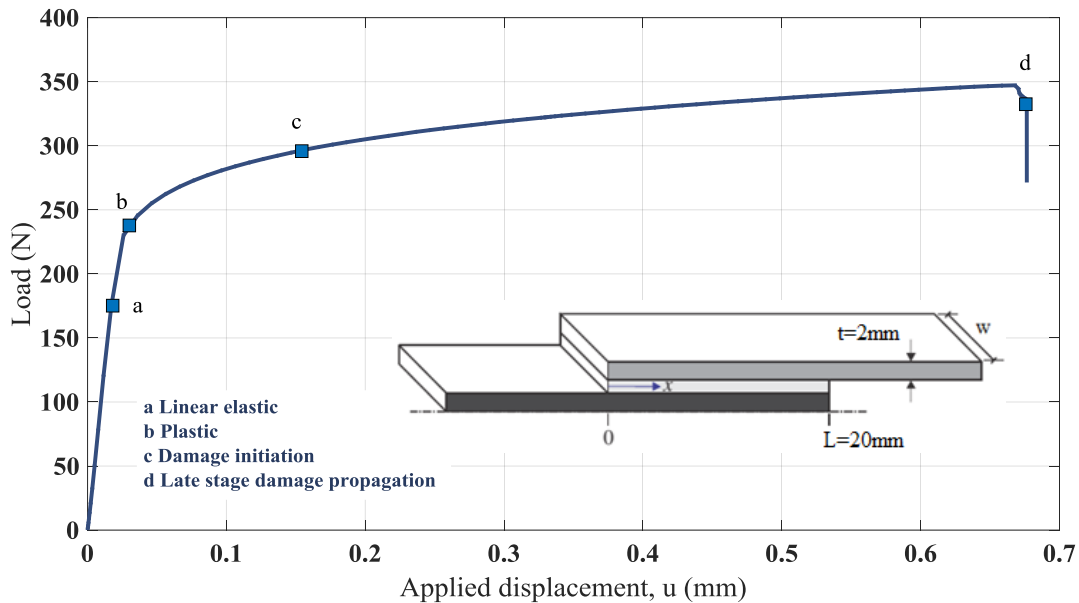


Fig. 6.23 Numerical predicted uni-axial load versus displacement response and failure steps of the L20 single lap joint configuration.

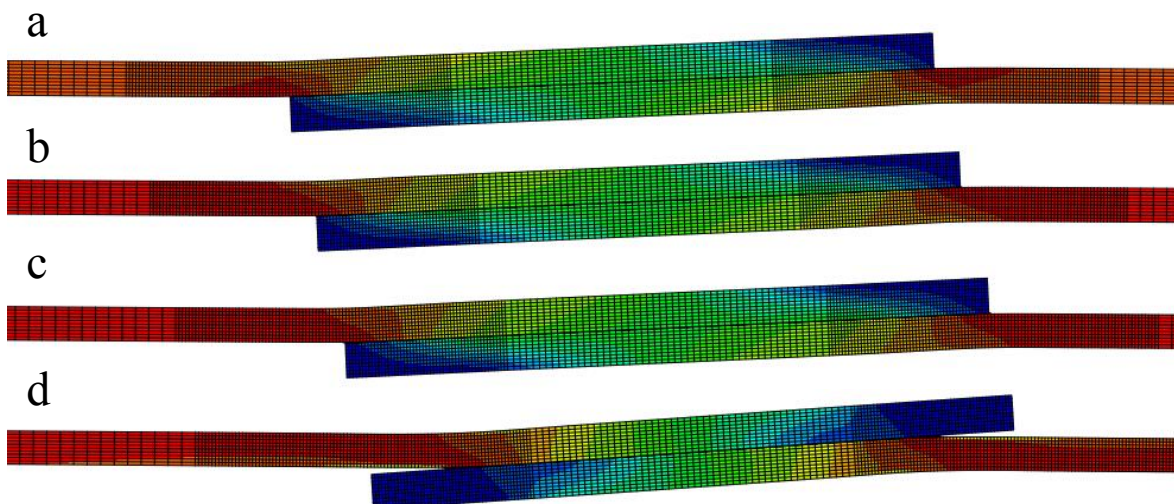


Fig. 6.24 Von-Mises stress distribution in the vicinity of the bonded area of the simulated L20 joint configuration (red is the maximum positive and blue is the minimum positive). The a-d subplots correspond to the linear elastic, plastic, damage initiation and late stage damage propagation, respectively, as described in Fig. 6.23.

The highest value of adhesive strength and adherend yield point ($\sigma_a=40\text{MPa}$ and $\sigma_y=400\text{MPa}$) are employed in Fig. 6.25 to describe damage level of cohesive elements. The figure implies that the adherend remains nearly in the elastic region until the softening process take place so that a low span of plastic deformation is observed. Furthermore, relatively low joint rotation due to high adherend rigidity ($\sigma_y=400\text{MPa}$ and $t=2\text{mm}$) and high separation strength would be pointed as a reason of attaining high failure loads up to 900N/mm (see Fig. 6.25). Based on the above results, increasing the overlap length is not only the critical parameter. Besides, adherend rigidity controls also behavior of load-displacement curve. In other words, the damage initiation occurs at nearly $u=0.056\text{mm}$ (where damage variable is $D=0$) then completed at $u=0.06\text{mm}$ (where damage variable is $D=1$). The softening process and final failure occur drastically within the displacement range of 0.004mm . This is a typical brittle failure mode under the dominant effect of peeling stresses that is highly localized at the joint extremities as seen in Fig. 6.26a, b, c and d, progressively. Note that the adherend bottom side having only the high stresses (depicted in red color) can be addressed as an evidence for the above statement. Similarly, in the middle regions of the bonded area vicinity, a small amount of stress is handled, which demonstrates the bonded area is not in full use (see Fig.6.26). It can be figured out from the FE simulations that the failure initiates at the edge of bonded length and propagates through the middle of the joint for single lap joints.

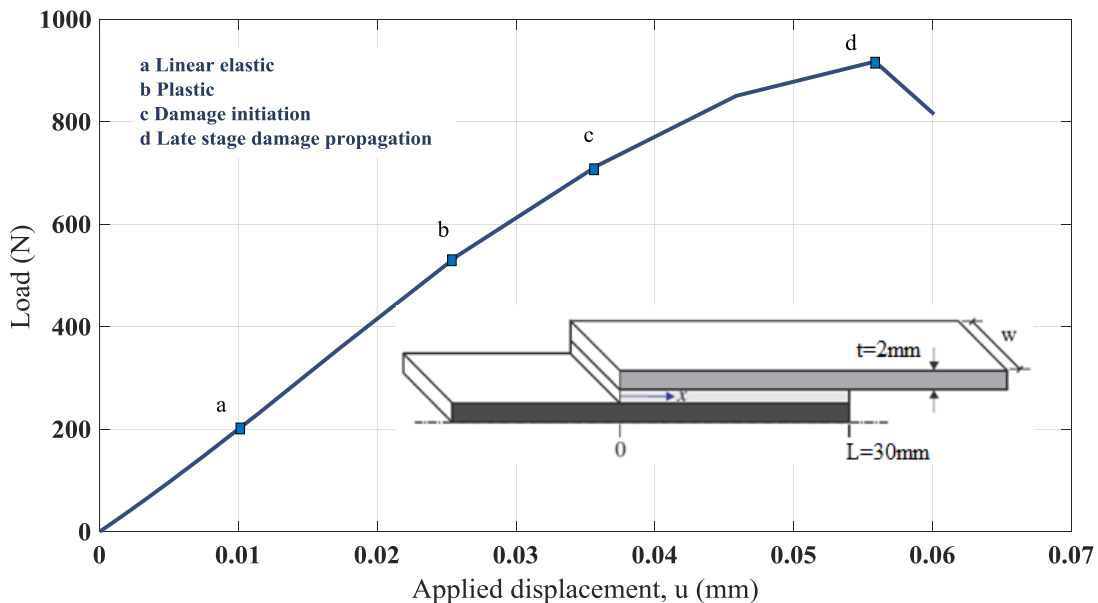


Fig. 6.25 Numerical predicted uni-axial load versus displacement response and failure steps of the L30 single lap joint configuration.

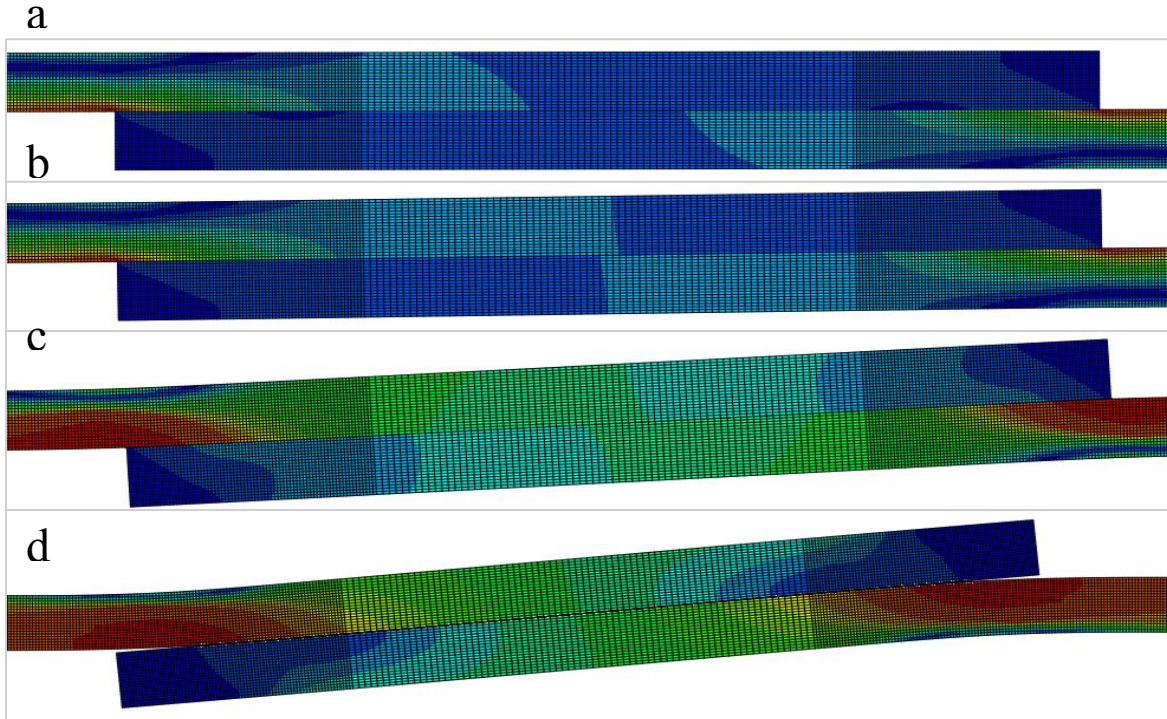


Fig. 6.26 Von-Mises stress distribution in the vicinity of the bonded area of the simulated L30 joint configuration (red is the maximum positive and blue is the minimum positive). The a-d subplots correspond to the linear elastic, plastic, damage initiation and late stage damage propagation, respectively, as described in Fig. 6.25.

The load versus applied displacement diagrams of 40 and 50mm overlap lengths are illustrated in Fig. 6.27. The plots are constructed adopting the similar material parameter ratio ($\sigma_y/\sigma_a=8$) for L40 and L50 joint configuration enabling to see effect of overlap length on the failure mechanism. For the large overlap lengths, the damage level can be assessed by the ratio between damaged and entire overlap length. It is concluded that the adherend fully reaches plastic region prior to adhesive critical stress. Apart from the small overlap lengths, no sudden drop is appeared after reaching the peak load value for both overlap length of 40 and 50mm (see Fig. 6.27). This is an indication of that the adhesive layer still carries load in the softening stage. This smooth load drop is more visible for L50, which exhibits nearly similar trend comparing to the L40 joint series. As the overlap length is increased further, the damage level of the cohesive zone attains to saturation, which means that the full adhesive layer is made full use of. After that, increasing the overlap length further with less rigid adherends would just rise up the dissipated energy during the softening process. However, it would not make a considerable change in failure load since the adherends reach their limits of saturation as mentioned at the beginning of this chapter. The normalized peeling stresses for larger

overlap lengths are described to be higher. But the rest of the bonded area are almost with zero level peeling stress. As an example, the joint continues to carry load after first damage is observed. This case is depicted in Fig 6.28c, d and e for L=50mm.

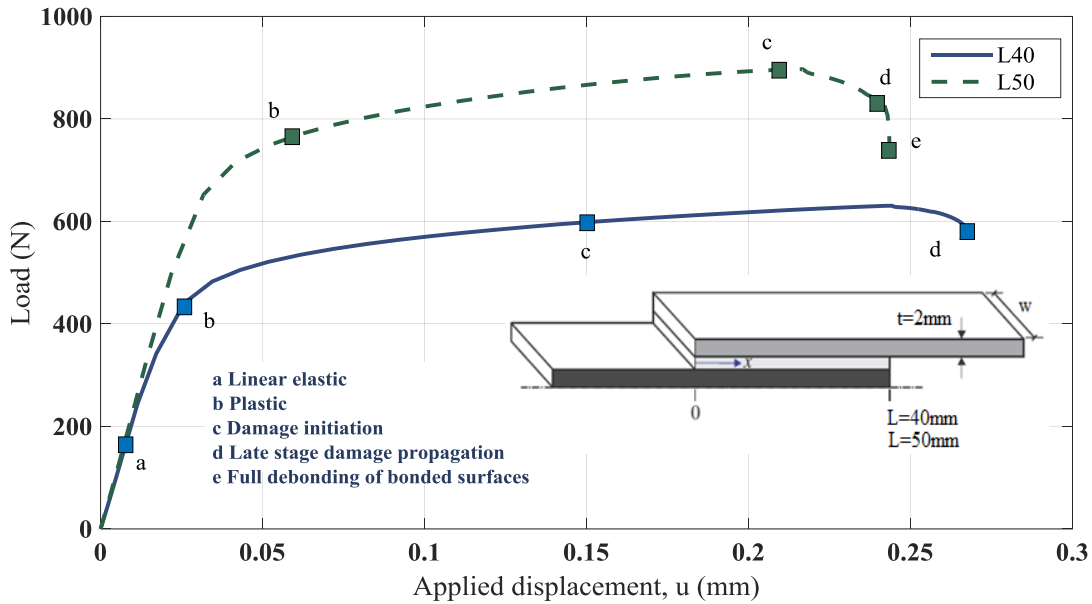


Fig. 6.27 Numerical predicted uni-axial load versus displacement response and failure steps of the L40 and L50 single lap joint configurations.

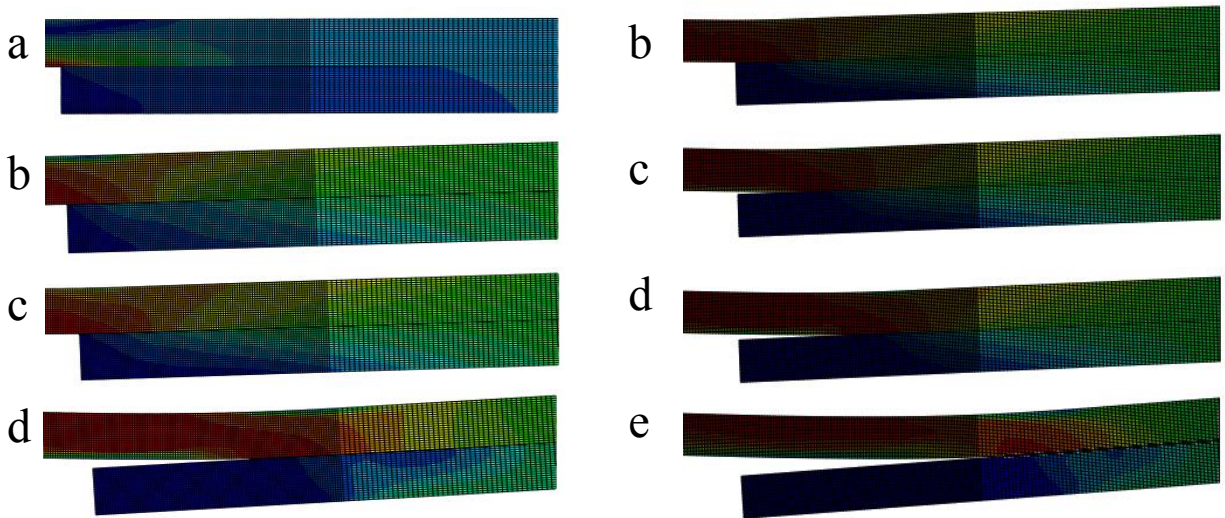


Fig. 6.28 Von-Mises stress distribution in the vicinity of the bonded area of the simulated L40 (on the left) and L50 (on the right) joint configurations (red is the maximum positive and blue is the minimum positive). The a-e subplots correspond to the linear elastic, plastic, damage initiation, late stage damage propagation and full debonding, respectively, as described in Fig. 6.27.

6.4 Parameter Normalization for Dimensional Analysis

The effect of various parameters on the performance of the single lap joints are investigated individually by means of accomplished FE simulations up to here. But it not sufficient to express how these parameters influence together the load carrying capacity of the adhesive joints. At the same time, the manufacture of the adhesive joints at different material properties and dimensions require some series of normalized (dimensionless) design parameters for the maximum joint performance. To perform this task, following normalized design parameters are considered for a general adhesive joint design methodology;

- Based on the results presented in this chapter, the geometry parameters L and t have great effect on the failure concept of bonded structures. Both of them increases the joint strength up to a certain point (saturation limit). For this reason the ratio L/t is selected to be a critical geometric parameter. The load carrying capacity of a single lap joint goes up directly with the increasing L/t ratios. It is suggested to be within range of 20 and 30 for low strength adhesive applications according to Fig. 6.29. But there is also a limitation of increasing t values regarding to the joint efficiency aspect, which is introduced in the next section.
- Secondly, the material properties of both adhesive and adherend material are the other vital factor. Because both of them have a positive impact on failure load. However, there is usually a restriction of using high strength adherend and adhesive material. They should be somehow optimized to meet required strength in the joining process. It is anticipated that only one normalized material parameter can be derived. The ratio σ_a/σ_y can be chosen as material dependent design parameter. In this way, this ratio should be chosen as higher as possible in the design stage to obtain higher failure loads. Contrary, it is not an efficient tool since the joints reach their saturation limits with thin adherends as illustrated in Fig. 6.29 where $t=1\text{mm}$.
- In order to decide how much bond strength is required to meet the adherend strength, a dimensionless parameter should be introduced. Basically, the ratio of the joint failure load in unit width and the tensile strength of the adherend material can be a comparison tool. This parameter $(F/\sigma_y t)$ exhibits the joint efficiency, approximately neglecting the rotation (bending effect).

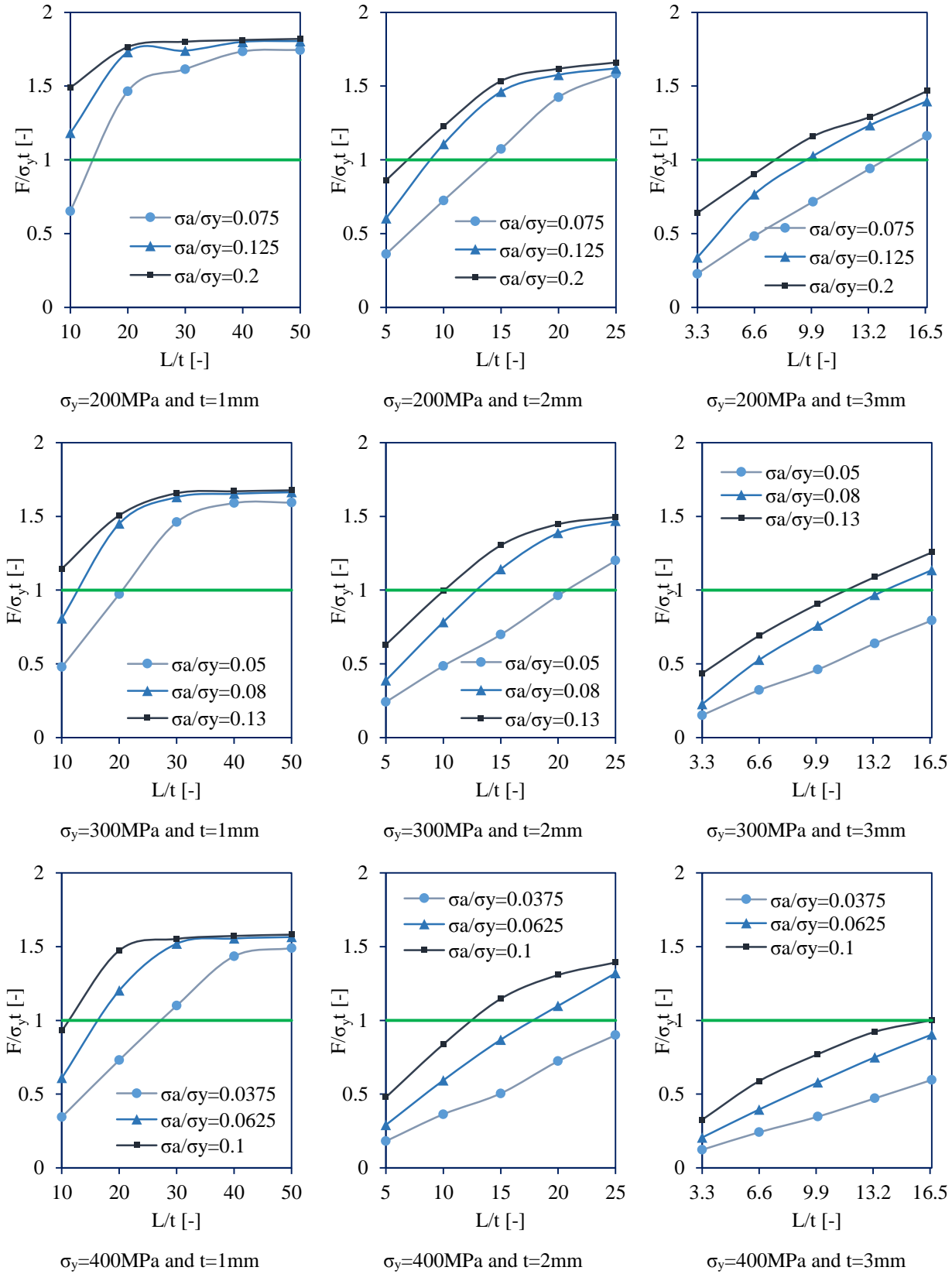


Fig. 6.29 Variation of the joint efficiency (performance) corresponding to various dimensionless design parameters.

Regarding the normalized design parameters (i.e L/t and σ_a/σ_y) the variation of the joint efficiency " $F/\sigma_y t$ " are depicted, consecutively in the subplots of Fig. 6.29. The green line over the horizontal axis represents the ideal case at which the adherend and adhesive layer strength are identical. In practical applications, the joint efficiency should not be higher than 1 so that utilizing excessive overlap length and adhesive strength are avoided. For this reason, the joint configurations above the green line (i.e where $F/\sigma_y t=1$) are not suitable for the optimum joint design. The subplots presents the variation of the joint efficiency for different L/t and σ_a/σ_y ratios (see Fig. 6.29). According to results, increasing the L/t ratio above 20 is not reasonable for thin adherends because the adherend strength is exceeded. Similarly, it is suggested to be lower than 15 for medium and high thickness adherends. However, implementing large thicknesses such that t is greater than 3mm is observed to remain under the ideal line (see Fig. 6.29 for $t=3\text{mm}$). It is emphasized that the material parameter " σ_a/σ_y " is the other critical factor particularly for more rigid adherends. It alters the joint efficiency sharply (nearly double) at moderate L/t values, which is shown in Fig. 6.29. On the other hand, the influence of these parameters eventually disappears when the joint configuration reaches critical or saturation limit. The saturation limits of the joints comprising the thin adherend ($t=1\text{mm}$) can be observed at the point where L/t ratio is about 40 (Fig. 6.29).

The design parameters (i.e $F/\sigma_y t$, σ_a/σ_y and L/t) are anticipated to be the most significant issue, which needs to be taken into consideration during the design stage. It is found out that the relationship among them can be nearly correlated by a linear function if the saturation limit determined. The feasibility of the efficiency would be given in the range 0.5 and 1 for an optimum joint design considering the efficiency scatters in the above subplots. As a result of FE simulations, the adherend thickness is found out to be more dominant than adherend yield point. Because, it controls the saturation limit of the joint, which including high nonlinearity due to inducing high amount of peeling stresses and joint eccentricity. Thus the regions below the green line can be recommended as an efficient and optimum joint design. The interval of each parameter on the curves (see Fig. 6.29) can be calculated in the case of satisfying optimum joint conditions.

7

Conclusion

In this thesis, a progressive failure model in ABAQUS® is employed to investigate load carrying capacity of the adhesive joints. An analytical expression of nonlinear material model for both adhesive and adherend material is established. FE simulations are performed considering the nonlinear geometry, elastic-plastic adhesive and adherend material in order to examine their influences on the joint strength and stress distributions. Adhesive layer is replaced by a zero thickness cohesive zone model to extensively understand the joint response as the thickness goes to zero. Besides the thickness effect on the intrinsic adhesive properties are presented as an analytical formulation. The parameters such as adhesive stiffness, tensile strength, fracture energy rate and yield stress of the adherend material are chosen to be analyzed for the joint strength evaluation. For this reason, the parameters are divided into two groups; geometry parameters (overlap length and adherend thickness), material parameters (yield stress of adherend, ultimate tensile strength of adhesive, fracture energy rate and initial stiffness). The overlap lengths of 10, 20, 30, 40 and 50mm corresponding to adherend thicknesses of 1, 2 and 3mm are selected as the geometrical parameters. The adhesive tensile strength of 15, 25 and 40MPa with the adherend yield stress of 200, 300 and 400MPa are considered. The trends of the adhesive joint strengths are given depending on the each parameter series above. Then some dimensionless design parameters are introduced with their effective ranges for an optimum joint design. An extensive experimental procedure is followed to validate FE results for various joint coupons, which includes

determination of cohesive zone parameters, experimentally. Consequently, following conclusions are drawn as a result of performed experiments and progressive FE simulations;

- The nonlinear material model for the structural steels can be approximated and implemented in the joint strength evaluation using power law as described in Eq. 4.16. Similarly, Eq. 4.17 and 4.18 are proposed to express non-linear material behavior of ductile and brittle epoxy adhesives, respectively. It is proven that the experimental tensile test results of ductile (Veropal HE-20) and brittle (Carboresin) adhesives are fitted by the proposed material models with a regression coefficient of $R^2=0.99$ and $R^2=0.976$, respectively.
- The error between experimental and FE failure load results remain below 18% for five different overlap lengths (10, 20, 30, 40 and 50mm) and two adherend thicknesses (1.5 and 2mm) for both epoxy adhesive type. It indicates that the proposed FE progressive failure model is an efficient tool in estimating strength of the adhesive joints.
- Application of zero thickness adhesive layer exhibited similar trends of stress distributions comparing to those with non-zero thicknesses. However, it reduces the joint eccentricity so that the normalized stress values at the joint extremities drop up to 1.5 for lower overlap lengths.
- The most dominant parameter are decided to the adherend thickness and overlap length, which can drastically change the joint strength up to 250% corresponding to same material configuration. Besides the influence of initial stiffness value is negligible since the adhesive layer is modelled to be infinitely thin. Although, fracture energy rate increases the joint strength, it has no considerable impact in the case of comparing the adhesives having the identical separation stress. But increasing the fracture energy rate only result in larger elongation in fracture.
- In design stage of the adhesive joints, three dimensionless parameters (L/t , σ_a/σ_y and $F/\sigma_y t$) are proposed for an optimum joint design. The range of each parameter should be controlled precisely since each joint configuration has a saturation state at which increasing one of them does not contribute the joint strength. Additionally, the strength of the joint has nearly a linear proportionality as a function of these parameters up to aforementioned critical point (saturation state).

References

- [1] Shet, C. and N. Chandra, Analysis of Energy Balance When Using Cohesive Zone Models to Simulate Fracture Processes. *Journal of Engineering Materials and Technology*, 2002. 124(4): p. 440-450.
- [2] Chandra, N., et al., Some issues in the application of cohesive zone models for metal– ceramic interfaces. *International Journal of Solids and Structures*, 2002. 39(10): p. 2827- 2855.
- [3] Needleman, A., An analysis of decohesion along an imperfect interface. *International Journal of Fracture*, 1990. 42(1): p. 21-40.
- [4] Needleman, A., A Continuum Model for Void Nucleation by Inclusion Debonding. *J. Appl. Mech.* , 1987(54): p. 525-531.
- [5] Xu, X.P. and A. Needleman, Numerical simulations of fast crack growth in brittle solids. *Journal of the Mechanics and Physics of Solids*, 1994. 42(9): p. 1397-1434.
- [6] Tvergaard, V. and J.W. Hutchinson, The relation between crack growth resistance and fracture process parameters in elastic-plastic solids. *Journal of the Mechanics and Physics of Solids*, 1992. 40(6): p. 1377-1397.
- [7] Barenblatt, G.I., The formation of equilibrium cracks during brittle fracture. General ideas and hypotheses. Axially-symmetric cracks. *Journal of Applied Mathematics and Mechanics*, 1959. 23(3): p. 622-636.
- [8] Camacho, G.T. and M. Ortiz, Computational modelling of impact damage in brittle materials. *International Journal of Solids and Structures*, 1996. 33(20–22): p. 2899-2938. 60
- [9] Geubelle, P.H. and J.S. Baylor, Impact-induced delamination of composites: a 2D simulation. *Composites Part B: Engineering*, 1998. 29(5): p. 589-602.
- [10] Chen, C.R., et al., Three-dimensional modeling of ductile crack growth: Cohesive zone parameters and crack tip triaxiality. *Engineering Fracture Mechanics*, 2005. 72(13): p. 2072-2094.
- [11] Users Guide to Adhesives, Huntsman Advanced Materials Americas Inc., 800-321-8511.
- [12] M. Goland, E. Reissner, The stresses in cemented joints, *J. Appl. Mech.* 11 (1944) 17–27.
- [13] Cornell RW. *J Appl. Mech.* 1953;20:355.
- [14] L.J. Hart-Smith, Adhesive-bonded Single-lap Joints, Technical Report, NASA CR- 112236, 1973.
- [15] Hart-Smith LJ. CR-112235, NASA Langley Research Center; 1973.

- [16] Hart-Smith LJ. In: Kinloch AJ, editor. *Developments in adhesives-2*. London: Applied Science Publishers; 1981.
- [17] Xiaocong He, A review of finite element analysis of adhesively bonded joints, *International Journal of Adhesion & Adhesives* 31 (2011) 248–264.
- [18] Kwang-Soo Kim, Yeong-Moo Yi, Gwang-Rae Cho, Chun-Gon Kim, Failure prediction and strength improvement of uni-directional composite single lap bonded joints, *Composite Structures* 82 (2008) 513–520.
- [19] Rui Zheng, Jianping Lin, Pei-Chung Wang, Chuanmin Zhu, Yongrong Wu, Effect of adhesive characteristics on static strength of adhesive-bonded aluminium alloys, *International Journal of Adhesion & Adhesives* 57 (2015) 85–94.
- [20] L. Goglio, M. Rossetto, E. Dragoni, Design of adhesive joints based on peak elastic stresses, *International Journal of Adhesion & Adhesives* 28 (2008) 427–435.
- [21] P.N.B. Reis, J.A.M. Ferreira, F. Antunes, Effect of adherend's rigidity on the shear strength of single lap adhesive joints, *International Journal of Adhesion & Adhesives* 31 (2011) 193–201.
- [22] Rene Quispe Rodríguez, William Portilho de Paiva, Paulo Sollero, Marcelo Ricardo Bertoni Rodrigues, Eder Lima de Albuquerque, Failure criteria for adhesively bonded joints, *International Journal of Adhesion & Adhesives* 37 (2012) 26–36.
- [23] J.P.M. Gonçalves, M.F.S.F. de Moura, P.M.S.T. de Castro, A three-dimensional finite element model for stress analysis of adhesive joints, *International Journal of Adhesion & Adhesives* 22 (2002) 357–365.
- [24] M.R. Ayatollahi, A. Akhavan-Safar, Failure load prediction of single lap adhesive joints based on a new linear elastic criterion, *Theoretical and Applied Fracture Mechanics* (2015) (Article in press).
- [25] Aydin, M. D., Özel, A., Temiz, Ş. The effect of adherend thickness on the failure of adhesively-bonded single-lap joints. *Journal of Adhesion Science and Technology*. 2005;19:705-18.
- [26] da Silva, L. F. M., Carbas, R. J. C., Critchlow, G. W., Figueiredo, M. A. V., Brown, K. Effect of material, geometry, surface treatment and environment on the shear strength of single lap joints. *Int J Adhes Adhes*. 2009;29:621-32.
- [27] da Silva, L. F. M., Ferreira, N. M. A. J., Richter-Trummer, V., Marques, E. A. S. Effect of grooves on the strength of adhesively bonded joints. *Int J Adhes Adhes*. 2010;30:735-43.
- [28] Taib, A. A., Boukhili, R., Achiou, S., Gordon, S., Boukehili, H. Bonded joints with composite adherends. Part I. Effect of specimen configuration, adhesive thickness, spew fillet and adherend stiffness on fracture. *International Journal of Adhesion and Adhesives*. 2006;26:226-36.

- [29] Alfano, M., Ambrogio, G., Crea, F., Filice, L., Furgiuele, F. Influence of Laser Surface Modification on Bonding Strength of Al/Mg Adhesive Joints. *Journal of Adhesion Science and Technology*. 2012;25:1261-76.
- [30] Bockenheimer, C., Valeske, B., Possar, W. Network structure in epoxy aluminium bonds after mechanical treatment. *International Journal of Adhesion & Adhesives*. 2002;22:349-56.
- [31] Prolongo, S. G., Ureña, A. Effect of surface pre-treatment on the adhesive strength of epoxy–aluminium joints. *International Journal of Adhesion and Adhesives*. 2009;29:23-31.
- [32] Rechner, R., Jansen, I., Beyer, E. Influence on the strength and aging resistance of aluminium joints by laser pre-treatment and surface modification. *International Journal of Adhesion and Adhesives*. 2010;30:595-601.
- [33] O'Mahoney, D. C., Katnam, K. B., O'Dowd, N. P., McCarthy, C. T., Young, T. M. Taguchi analysis of bonded composite single-lap joints using a combined interface–adhesive damage model. *International Journal of Adhesion and Adhesives*. 2013;40:168-78.
- [34] He, X. A review of finite element analysis of adhesively bonded joints. *International Journal of Adhesion and Adhesives*. 2011;31:248-64.
- [35] Xu, W., Wei, Y. Strength and interface failure mechanism of adhesive joints. *International Journal of Adhesion and Adhesives*. 2012;34:80-92.
- [36] Xu, W., Wei, Y. Influence of adhesive thickness on local interface fracture and overall strength of metallic adhesive bonding structures. *International Journal of Adhesion and Adhesives*. 2013;40:158-67.
- [36] Tong L. Strength of adhesively bonded single-lap and lap-shear joints. *Int J Solids Struct* 1998;35:2601–16.
- [37] Sina Ebnesajjad, *Adhesive Technology Handbook*, Norwich, NY, USA.
- [38] Xin Chen, Numerical study of stable tearing crack growth events using the cohesive zone model approach, (Ph.D thesis) Mechanical Engineering College of Engineering and Computing University of South Carolina, 2013.
- [39] ABAQUS® HTML Documentation, Dassault Systems, 2009.
- [40] Campilho RDSG, de Moura MFSF, Domingues JJMS. Using a cohesive damage model to predict the tensile behaviour of CFRP single-strap repairs. *International Journal of Solids and Structures* 2008;45:1497–512.
- [41] Pardo T, Ferracin T, Landis CM, Delannay F. Constraint effects in adhesive joint fracture. *J Mech Phys Solids* 2005;53:1951–83.
- [42] Wei Xu n, Yueguang Wei, Influence of adhesive thickness on local interface fracture and overall strength of metallic adhesive bonding structures, *International Journal of Adhesion & Adhesives*, (2013) 158–167

- [43] ASTM D1002-10. Standard test method for apparent shear strength of single-lap-joint adhesively bonded metal specimens by tension loading (metal-to-metal). West Conshohocken (PA): ASTM International; 2010.
- [44] Turon A, Da'vilab CG, Camanhoc PP, Costa J. An engineering solution for mesh size effects in the simulation of delamination using cohesive zone models. *Eng Fract Mech* 2007;74(10):1665–82.
- [45] ČSN EN 10025-94 Nelegovaná ocel obvyklých vlastností-OCEL 11 343, Praha: Český normalizační institut, 28 p; 2004. (Original in Czech Language).
- [46] Guzanová A, Brezinová J, Draganovská D, et al. A study of the effect of surface pre-treatment on the adhesion of coatings. *J. Adhes. Sci. Technol.* 2014;28:1754–1771. doi:<http://dx.doi.org/10.1080/01694243.2014.920762>
- [47] ČSN EN ISO 527-2. Plastics- determination of tensile properties -part 2: test conditions for moulding and extrusion plastics. 2012.
- [48] “Standard Test Method for Mode I Interlaminar Fracture Toughness of Unidirectional Fiber Reinforced Polymer Matrix Composites”, *Annual Book of ASTM Standards*, Vol. 15.06, 2001.
- [49] “Standard Test Method for Mode II Interlaminar Fracture Toughness of Unidirectional Fiber-Reinforced Polymer Matrix Composites”, SACMA BMS 8-276F, 2000.
- [50] Critchlow GW, Brewis DM. Review of surface pretreatments for aluminium alloys. *Int. J. Adhes. Adhes.* 1996;16:255–275. doi:[http://dx.doi.org/10.1016/S0143-7496\(96\)00014-0](http://dx.doi.org/10.1016/S0143-7496(96)00014-0)
- [51] ASTM D1002-10. Standard test method for apparent shear strength of single-lap-joint adhesively bonded metal specimens by tension loading (metal-to-metal). West Conshohocken (PA): ASTM International; 2010.
- [52] Ji GF, Ouyang ZY, Li GQ. On the interfacial constitutive laws of mixed mode fracture with various adhesive thicknesses. *Mech Mater* 2012;47:24–32.
- [53] Ji GF, Ouyang ZY, Li GQ. Effects of bondline thickness on mode-II interfacial laws of bonded laminated composite plate. *Int J Fract* 2011;168:197–207.
- [54] Ji GF, Ouyang ZY, Li GQ, Ibekwe S, Pang SS. Effects of adhesive thickness on global and local mode-I interfacial fracture of bonded joints. *Int J Solids Struct* 2010;47:2445–58.
- [55] Carlberger T, Stigh U. Influence of layer thickness on cohesive properties of an epoxy-based adhesive—an experimental study. *J Adhes* 2010;86:814–33.

Appendices

APPENDIX 1. GLOSSARY OF TERMS (BASED ON BSI AND ASTM DEFINITIONS)

Adherend: Body that is or intended to be held to another body by an adhesive.

Adherend failure: Failure of a joint in the body of the adherend.

Adhesion: State in which two surfaces are held together by interfacial bonds.

Adhesive: Non-metallic substance capable of joining materials by surface bonding (adhesion), the bonding possessing adequate internal strength (cohesion).

Adhesive failure: Failure of an adhesive bond, such that separation appears to be at the adhesive/adherend interface.

ASTM: American Society for Testing and Materials.

Bond: The union of materials by adhesives.

Bond-line: The layer of adhesive, which attaches two adherends.

Bond strength: The unit of load applied to tension, compression, flexure, peel, impact, cleavage, or shear, required to break an adhesive assembly with failure occurring in or near the plane of the bond.

BSI: British Standards Institute

Bulk adhesive: The adhesive unaltered by the adherend.

Cleavage: Mode of application of a force to a joint between rigid adherends, which is not uniform over the whole area, but results in a stress concentrated at one edge.

Cohesion: The ability of the adhesive to resist splitting or rupture.

Cohesive failure: Failure within the body of the adhesive (i.e. not at the interface).

Cure: To set or harden by means of a chemical reaction.

Cure time: Time required to affect a cure at a given temperature.

Durability: The endurance of joint strength relative to the required service conditions.

Elastomer: A rubbery material that returns to approximately its original dimensions in a short time after undergoing a large amount of deformation.

Environmental test: Test to assess the performance of an assembly under service conditions.

Glass transition: A reversible change in an amorphous polymer or in amorphous regions of a partially crystalline polymer from (or to) a viscous or rubbery condition to (or from) a hard and relatively brittle one.

ISO: International Standards Organisation.

Lap joint: Joint made by placing one adherend partly over another and bonding together the overlapped portions.

Open time: Time interval from when an adhesive is applied to when the material becomes unworkable.

Peel: Mode of application of a force to a joint in which one or both of the adherends is flexible and which the stress is concentrated at a boundary.

Plasticisation: Increase in softness, flexibility, and extensibility of an adhesive.

Post-cure: Further treatment by time and/or temperature of an adhesive to obtain the required properties by curing.

Shear: Mode of application of a force to a joint that acts in the plane of the bond.

Strain: Unit change due to force in size of body relative to its original size.

Stress: Force exerted per unit area at a point within a plane.

Stress-strain diagram (or curve): A diagram in which corresponding values of stress and strain are plotted against each other.

Structural bond: A bond, which is capable of sustaining in a structure a specified strength level under a combination of stresses for a specified time.

Substrate: An adherend, a material upon which an adhesive is applied.

Surface preparation (or treatment): Physical and/or chemical treatments applied to adherends to render them suitable or more suitable for adhesive bonding.

Tension: Mode of application of a tensile force normal to the plane of a joint between rigid adherends and uniformly distributed over the whole area of the bond-line.

Thermoset: A resin that is substantially infusible and insoluble after being cured.

Thermoplastic: A material that can be repeatedly softened by heating.

Viscosity: Resistance of a liquid material to flow.

Wet strength: Strength of an adhesive bond determined immediately after removal from a liquid in which it has immersed under specified conditions.

Wetting: A surface is considered completely wet by a liquid if the contact angle is zero, and incompletely wet if the contact angle has a finite value.

Yield stress: The stress (either normal or shear) at which a marked increase in deformation occurs without an increase in load.

Yield strain: The strain, below which a material acts in an elastic manner, and above which it begins to exhibit permanent deformation.

APPENDIX 2. LIST OF AUTHOR'S PUBLICATIONS RELATED TO THE THEME OF THE DISSERTATION

- [1] Özdemir, A., Kocabaş, I., Svanda, P. Analyzing Adhesion of Epoxy/Steel Interlayer in Scratch Test, *Int. Journal of Engineering Research and Application (IJERA)*, 2015, 5(11), pp.42-52, ISSN: 2248-9622 (Online), <http://www.ijera.com/>
- [2] Kocabaş, I., Svanda, P., Özdemir, A. Failure Load Prediction of Structural Adhesive Joints Based on Local Yielding Criterion with Non-linear Material Behaviour. *Int. Journal of Scientific and Technological Research*, 2015; 1(9): pp. 10-20, ISSN: 2422-8702 (Online), <http://www.iiste.org>
- [3] Kocabaş, I., Özdemir, A., Svanda, P. Design of Single Lap Joints with Mild Steel Adherends, 22th International Conference Engineering Mechanics 2016, Svatka – Czech Republic, May 9 - May 12, 2016, pp.289-292, ISBN:978-80-87012-59-8, ISSN:1805-8256 <http://www.engmech.cz/>
- [4] Özdemir, A., Kocabaş, I., Svanda, P. Degradation Mechanism of Adhesive Joints with Mild Steel Adherends, 33th International Colloquium-Advanced Manufacturing And Repair Technologies In Vehicle Industry, Western Tatras-Zuberec, Slovakia., May 25 - May 27, 2016, pp.81-84, ISBN:978-80-554-1214-6
- [5] Özdemir, A., Kocabaş, I., Svanda, P. Improving the Strength of Adhesively Bonded Joints through the Introduction of Various Surface Treatments, *Journal of Adhesion Science and Technology*, vol. 30, no.23, (2016) p.2573-2595., ISBN:0169-4243. DOI: 10.1080/01694243.2016.1188872